

# NAVAL POSTGRADUATE SCHOOL

## Monterey, California



### THESIS

19990805 032

**MODELED DETECTION AND RECOGNITION RANGE  
FOR A POLARIZATION FILTERED FLIR SENSOR**

by

Spyridon E. Lagaras

June 1999

Thesis Advisor:

Co-Advisor:

Alfred W. Cooper

Ron J. Pieper

Approved for public release; distribution is unlimited.

REPORT DOCUMENTATION PAGE			Form Approved OMB No. 0704-0188	
Public reporting burden for this collection of information is estimated to average 1 hour per response, including the time for reviewing instruction, searching existing data sources, gathering and maintaining the data needed, and completing and reviewing the collection of information. Send comments regarding this burden estimate or any other aspect of this collection of information, including suggestions for reducing this burden, to Washington headquarters Services, Directorate for Information Operations and Reports, 1215 Jefferson Davis Highway, Suite 1204, Arlington, VA 22202-4302, and to the Office of Management and Budget, Paperwork Reduction Project (0704-0188) Washington DC 20503.				
1. AGENCY USE ONLY (Leave blank)		2. REPORT DATE June 1999		3. REPORT TYPE AND DATES COVERED Master's Thesis
4. TITLE AND SUBTITLE MODELED DETECTION AND RECOGNITION RANGE FOR A POLARIZATION FILTERED FLIR SENSOR			5. FUNDING NUMBERS	
6. AUTHOR(S) Lagaras, Spyridon E.				
7. PERFORMING ORGANIZATION NAME(S) AND ADDRESS(ES) Naval Postgraduate School Monterey, CA 93943-5000			8. PERFORMING ORGANIZATION REPORT NUMBER	
9. SPONSORING / MONITORING AGENCY NAME(S) AND ADDRESS(ES)			10. SPONSORING / MONITORING AGENCY REPORT NUMBER	
11. SUPPLEMENTARY NOTES The views expressed in this thesis are those of the author and do not reflect the official policy or position of the Department of Defense or the U.S. Government.				
12a. DISTRIBUTION / AVAILABILITY STATEMENT Approved for public release; distribution unlimited.			12b. DISTRIBUTION CODE	
13. ABSTRACT (maximum 200 words) A model has been developed to evaluate the influence of polarization filtering on the detection and identification range of a thermal sensor. The scenarios evaluated were based on environmental parameters and ship temperatures recorded during the EOPACE measurement series in San Diego bay in 1996. These scenarios represent a FLIR sensor on a platform in level flight at 100 m or 1000 m approaching a ship target, represented as a gray body at the recorded ship hot-spot temperature. The polarized version of the SEARAD sea radiance code was used to provide sea background radiance and propagation characteristics for both ship target and background. Apparent Temperature Difference was calculated versus range for horizontally polarized and unpolarized imaging. Maximum range was determined for both cases by comparison to a generic Minimum Resolvable Temperature function representing a typical LWIR Common Module FLIR. Preliminary results for the polarized case predict greater apparent temperature difference at ranges to around 10 kilometers. Unresolved apparent anomalies in the computed results suggest that target temperatures are under-estimated. Empirical correction of the zero range temperature difference suggests polarized identification ranges of the order of 25 to 30 km. Improvements to the modeling are proposed.				
14. SUBJECT TERMS Forward Looking Infrared (FLIR), Apparent Temperature Difference, Common Module FLIR, Minimum Resolvable Temperature Difference (MRTD), SEARAD			15. NUMBER OF PAGES 157	
			16. PRICE CODE	
17. SECURITY CLASSIFICATION OF REPORT Unclassified		18. SECURITY CLASSIFICATION OF THIS PAGE Unclassified		19. SECURITY CLASSIFICATION OF ABSTRACT Unclassified
				20. LIMITATION OF ABSTRACT UL

NSN 7540-01-280-5500

Standard Form 298 (Rev.2-89)  
Prescribed by ANSI Std. Z39-18



Approved for public release; distribution is unlimited

**MODELED DETECTION AND RECOGNITION RANGE FOR A  
POLARIZATION FILTERED FLIR SENSOR**

Spyridon E. Lagaras  
Lieutenant, Hellenic Navy  
B.S., Hellenic Naval Academy, 1989

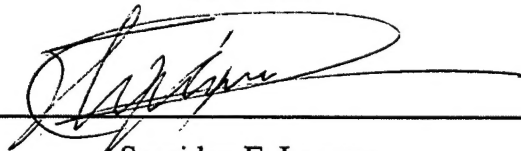
Submitted in partial fulfillment of the  
requirements for the degrees of

**MASTER OF SCIENCE IN APPLIED PHYSICS  
AND  
MASTER OF SCIENCE IN ELECTRICAL ENGINEERING**

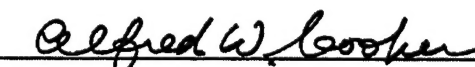
from the

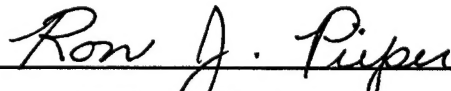
**NAVAL POSTGRADUATE SCHOOL  
June 1999**

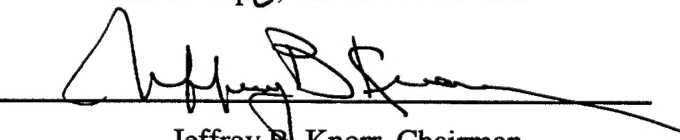
Author: \_\_\_\_\_


  
Spyridon E. Lagaras

Approved by: \_\_\_\_\_

  
Alfred W. Cooper, Thesis Advisor

  
Ron J. Pieper, Thesis Co-Advisor

  
Jeffrey B. Knorr, Chairman  
Department of Electrical and Computer Engineering

  
William B. Maier II, Chairman  
Department of Physics





## ABSTRACT

A model has been developed to evaluate the influence of polarization filtering on the detection and identification range of a thermal sensor. The scenarios evaluated were based on environmental parameters and ship temperatures recorded during the EOPACE measurement series in San Diego bay in 1996. These scenarios represent a FLIR sensor on a platform in level flight at 100 m or 1000 m approaching a ship target represented as a gray body at the recorded ship hot-spot temperature. The polarized version of the SEARAD sea radiance code was used to provide sea background radiance and propagation characteristics for both ship target and background. Apparent Temperature Difference was calculated versus range for horizontally polarized and unpolarized imaging. Maximum range was determined for both cases by comparison to a generic Minimum Resolvable Temperature function representing a typical LWIR Common Module FLIR. Preliminary results for the polarized case predict greater apparent temperature difference at ranges to around 10 kilometers. Unresolved apparent anomalies in the computed results suggest that target temperatures are under-estimated. Empirical correction of the zero range temperature difference suggests polarized identification ranges of the order of 25 to 30 km. Improvements to the modeling are proposed.



## TABLE OF CONTENTS

I. INTRODUCTION.....	1
II. INFRARED TECHNOLOGY FUNDAMENTALS .....	5
A. THE ELECTROMAGNETIC SPECTRUM .....	5
B. RADIANT ENERGY TRANSFER UNITS .....	8
C. BASIC LAWS OF THERMAL RADIATION.....	9
1. Black Body Radiation.....	9
2. Total Power Law.....	11
3. Kirchoff's Law .....	11
4. Planck's Radiation Law.....	12
5. Wien's Displacement and Stefan-Boltzmann Laws .....	13
D. ATMOSPHERIC PROPAGATION.....	15
1. Absorption .....	16
2. Scattering .....	18
a) Rayleigh Scattering.....	20
b) Mie Scattering .....	21
E. POLARIZATION.....	22
1. Polarization Physics.....	22
a) Stokes Parameters.....	22
b) Emission Polarization .....	24
c) Reflection Polarization .....	27
2. Polarization Filtering Techniques.....	29
F. TARGET TO BACKGROUND CONTRAST .....	30
G. FORWARD LOOKING INFRARED SYSTEMS .....	32
1. Infrared Detection.....	34
2. Image Formation.....	35
3. Image Processing.....	36
4. Display.....	37
III. EXPERIMENT DESCRIPTION AND SCENARIOS.....	39
A. EXPERIMENT EQUIPMENT.....	39
1. Internal Polarizing Filtering with the AGA-780.....	39
2. Research Vessel POINT SUR.....	42
3. Software.....	42
a) CEDIP PTRWIN .....	42
b) Interactive Data Language .....	43
c) SeaRad.....	43
B. THE EXPERIMENT .....	44
C. DATA.....	45
1. Images.....	45
2. Meteorological Data .....	47
3. Ship Skin Temperature Data.....	48
D. SCENARIOS.....	48
IV. SYSTEM PERFORMANCE FIGURES OF MERIT AND DETECTION CRITERIA.....	51
A. FLIR PERFORMANCE MEASURES.....	51
1. Noise Equivalent Temperature Difference .....	51
a) Minimum Detectable Temperature Difference .....	53
b) Minimum Resolvable Temperature Difference.....	55
B. APPARENT TEMPERATURE DIFFERENCE COMPUTATION .....	58
C. DETECTION CRITERIA AND PROJECTED AREA OF THE SHIP .....	61
1. Visual Discrimination Criteria.....	64
2. Critical Dimension and Target Aspect.....	65
D. MRT COMPUTATION AND CALCULATION VS RANGE WITH VARIOUS CRITERIA.....	69

V. RESULTS .....	83
VI. CONCLUSIONS AND DISCUSSION .....	91
VII. RECOMMENDATIONS FOR FUTURE WORK .....	95
APPENDIX A. EXPERIMENT LOCATION .....	97
APPENDIX B. POLARIZER FILTERS .....	103
APPENDIX C. R/V POINT SUR.....	109
APPENDIX D. SEARAD.....	113
APPENDIX E. METEOROLOGICAL DATA .....	117
APPENDIX F. CONVERSION OF TEMPERATURE TO IN BAND RADIANCE.....	127
APPENDIX G. CALCULATION OF APPARENT TEMPERATURE DIFFERENCE.....	129
APPENDIX H. CALCULATION OF MRT AND MTF .....	131
APPENDIX I. IDL OUTPUTS.....	135
APPENDIX J. EXCEL SPREADSHEET OUTPUTS.....	137
APPENDIX K. SPECTRAL RADIANCE OF A BLACK BODY AT DIFFERENT TEMPERATURES.....	139
LIST OF REFERENCES .....	141
INITIAL DISTRIBUTION LIST .....	145

## ACKNOWLEDGEMENTS

This research has been supported in part by Naval Command Control and Ocean Surveillance Center, Propagation Division, Code 88 and by the Naval Postgraduate School Institute for Joint Warfare Analysis.

I would also like to express my appreciation to the participants of the EOPACE measurement series, the crew of R/V POINT SUR, the Naval Postgraduate School Boundary Layer Meteorology Group and the NPS NACIT (Infrared Technology Group).

Most of all I would like to thank Professor Alfred W. Cooper for his guidance, patience, support and friendship. I consider working with him a great experience that I will cherish for the rest of my career.

My special thanks to Professor Ron J. Pieper for his outstanding patience and being a great support to my work.

Finally, I would like to thank my wife Elena for her support and understanding during my work on this thesis.



## I. INTRODUCTION

Infrared systems have numerous applications in today's military environment. Their primary use is for target detection, recognition and identification by discriminating between target and background temperature. There is an intensive scientific and technological effort to improve the performance of such systems due to the high potential of the military applications using this technology.

The operating environment of the infrared devices is a noisy one and strongly influenced by the weather conditions. In order to improve the target-to-background contrast, which eventually will improve the detection capabilities of a system, various techniques have been tried. One such promising technique is the use of polarization filters in the sensor. The application of this method requires an environment in which the electromagnetic energy coming from the source or background is polarized. The sea background comprises such an environment.

It has been found that the infrared electric vector of sea radiance is preferentially horizontally polarized in the sun glint corridor within a few degrees of the horizon and vertically polarized from the adjacent sea background at similar grazing angles. Previous experiments and analysis done at the Naval Postgraduate School [Ref.6,13,16,22] have shown that there is a significant contrast improvement between a man-made target, such as a ship which gives no apparent polarized feature properties to the reflected or emitted energy, and the sea. Therefore horizontally polarized filters can improve the target-to-background contrast while viewing target scenes outside the sun glint. It must be taken into consideration though, that the magnitude of degree of polarization was found to be



much greater in the 3 to 5  $\mu m$  band in the Sun glint regions than the 8 to 12  $\mu m$  band which dominates emission and is the band that will be used for this work.

In this thesis data from an experimental data set that was obtained in the Electro-Optic Propagation Assessment in the Coastal Environment (EOPACE) multinational measurements series in San Diego Bay in 1996, is used to retrieve some data for the construction of the scenarios that were used for the analysis. EOPACE is a program sponsored by ONR and organized by SPAWAR SYSTEMS CENTER, San Diego, Ocean and Atmospheric Sciences Division, Code 543. The purpose of the EOPACE measurements is to quantify infrared propagation characteristics for near ocean surface transmission and analyze Electro-Optic systems performance in the coastal environment conditions. The data that were used in this thesis were obtained by the NPS Boundary Layer Meteorology Group on the Research Vessel (R/V) POINT SUR and NPS NACIT (Infrared Technology Group) at Building 15 of the Naval Command Control and Ocean Surveillance Center (NRAD) on Point Loma, California, on 9 April 1996. The collected data comprise 5,508 images of the R/V POINT SUR in sets of various ranges, aspect angles, meteorological conditions and ship skin temperatures. The data that were collected in the experiment are image sets of horizontally polarized, vertically polarized and unpolarized images of the R/V POINT SUR taken with an AGA 780 camera using internal polarizers (Aluminum grid on a KRS-5 substrate).

This thesis addresses the prediction of detection, recognition and identification ranges with and without polarization for a target with the characteristics of R/V POINT SUR by taking under consideration the specific environmental conditions when the

measurements were conducted. The project addresses two different scenarios in which a generic Forward Looking Infrared (FLIR) platform sensor approaches the target (R/V POINT SUR) at different heights. For the calculation of the apparent target to background temperature difference ( $\Delta T_{app}$ ) at given range the SEARAD atmospheric propagation code is used, which is a modified form of the standard MODTRAN code taking into consideration the effects of polarization. SEARAD is a DOS compatible program developed by C.R. Zeisse at NCCOSC-NRaD (Naval Command, Control and OCEAN Surveillance Center-Naval Research and Development), for application to naval problems [Ref.28]. The sensor performance is described by the parameter Minimum Detectable Temperature Difference (MDTD) or Minimum Resolvable Temperature Difference (MRTD) as appropriate. By comparing the MRTD with  $\Delta T_{app}$  the maximum ranges for detection, recognition and identification will be estimated by using specific (standard) criteria to describe the actual target.



## II. INFRARED TECHNOLOGY FUNDAMENTALS

In order to follow a progressive approach to the objectives of this thesis a brief presentation of the basic laws and theories of Infrared technology is necessary. Only the most important points necessary to comprehend the basic physical phenomena associated with this work will be addressed.

### A. THE ELECTROMAGNETIC SPECTRUM

In general, waves are means of transporting energy or information. Typical examples of Electromagnetic Waves are light rays, radio waves and radar beams. Their common characteristic is the spatial and temporal variations of the electric and the magnetic fields. They relate with each other and their relationship is presented by Maxwell's equations:

$$\text{Faraday's Law: } \nabla \times \mathbf{E} = -\frac{\partial \mathbf{B}}{\partial t} \quad (2.1)$$

$$\text{Ampere's Law: } \nabla \times \mathbf{H} = \mathbf{J} + \frac{\partial \mathbf{D}}{\partial t} \quad (2.2)$$

$$\text{Gauss's Law: } \nabla \cdot \mathbf{D} = \rho_v \quad (2.3)$$

$$\text{Nonexistence of isolated magnetic charge: } \nabla \cdot \mathbf{B} = 0 \quad (2.4)$$

where:

$\mathbf{E}$ = Electric field intensity vector (Volts/meter)

**B**= Magnetic flux density (Tesla)

**T**= Time (seconds)

**H**= Magnetic field intensity vector (Amperes/meter)

**J**= Current density (Amperes/meter<sup>2</sup>)

**D**= Electric field density vector (Coulomb/ meter<sup>2</sup>)

$\rho_v$  = Volume charge density (Coulomb/ meter<sup>3</sup>)

Since all of the above mentioned waves as well as infrared waves comply with the same laws, they are of the same nature. However quantization effects which may be ignored at long wavelengths are of major significance in the visible and infrared.

What is known as optical radiation covers the electromagnetic spectrum from the Ultraviolet (UV) range throughout the visible and up to the infrared (IR) portion of the spectrum, as shown in Figure 1 [Ref.1].

The ultraviolet portion ranges from about 0.1 up to 0.40  $\mu m$  . The visible range of the electromagnetic spectrum to the human eye, commonly known as visible light, is from 0.40  $\mu m$  up to 0.77  $\mu m$  . The infrared portion is divided into three operational regions; the near infrared or short wavelength infrared (SWIR) region ranging from 0.77  $\mu m$  up to 3  $\mu m$  ; the middle wavelength infrared (MWIR) ranging from 3  $\mu m$  up to 8  $\mu m$  ; the long wavelength infrared (LWIR) from 8  $\mu m$  up to 14  $\mu m$  ; and finally the far and extreme infrared region ranging 14  $\mu m$  up to 1000  $\mu m$  . The region from 5  $\mu m$  to 8  $\mu m$  is also a part of the infrared spectrum, but is not used due to the high absorption of the atmosphere in this area.

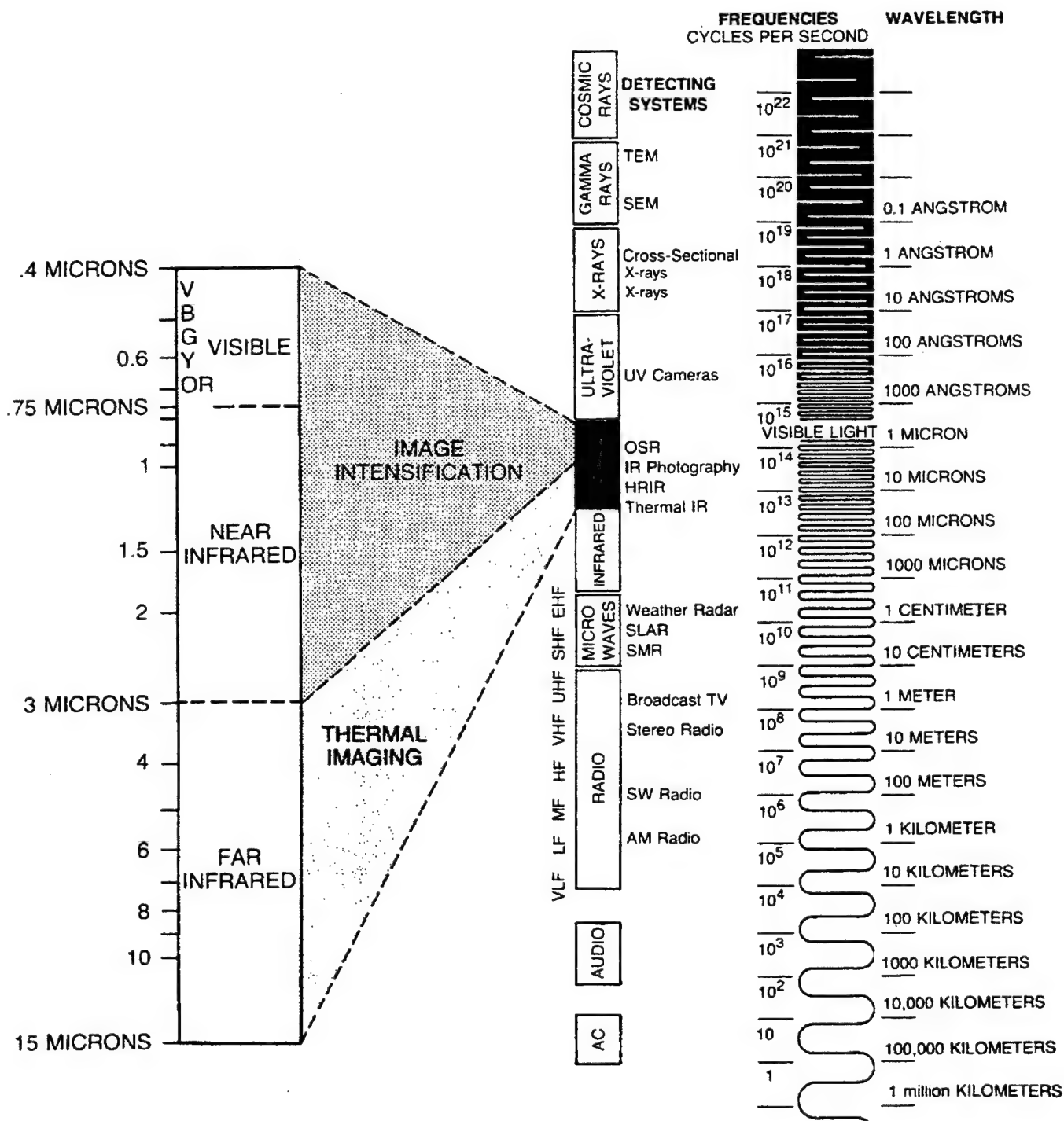


Figure 1 - The Electromagnetic Spectrum [Ref.1].

Imaging devices working in the near infrared region sense ambient radiation that is reflected from the targets and the background scene. These devices are known as night vision devices and can detect infrared with wavelength up to about  $1.5\ \mu\text{m}$ . Infrared radiation with wavelengths greater than  $3\ \mu\text{m}$  is known as thermal radiation, because the energy emitted by the target due to its temperature provides the largest part of the detectable signature. Thermal imaging systems basically take advantage of this thermal energy that every object emits, and work in the regions of MWIR and LWIR. Such devices are the Forward Looking Infrared (FLIR) and the Infrared Search and Track (IRST).

## **B. RADIANT ENERGY TRANSFER UNITS**

The basic radiometric quantities and units of the infrared radiation are presented in Table 1 [Ref. 2:p.14] in both their energy and photon forms. To distinguish between the two a different subscript is used (e for energy and q for quanta). The most common detector type that is used is the quantum detector, whose output signal is directly proportional to the integral of the incident photon flux over a specific time period. This is the main factor that makes desirable the use of the photon forms. Historically the energy forms were and still are being used for detector performance measurements. Therefore both approaches are still useful.

Table 1 - Definition of Radiometric Quantities and units.

Quantity	Definition	Energy Symbol	Photon Symbol
Radiant Energy Q	Total Radiated Energy	$Q_e$ (J)	$Q_q$ (Photons)
Radiant Flux $\Phi$	$\frac{\partial Q}{\partial t}$	$\Phi_e$ (W)	$\Phi_q$ (Photons sec <sup>-1</sup> )
Radiant Flux or Exitance M	$\frac{\partial \Phi}{\partial A}$	$M_e$ (W m <sup>-2</sup> )	$M_q$ (Photons sec <sup>-1</sup> m <sup>-2</sup> )
Irradiance I	$\frac{\partial \Phi}{\partial A}$	$E_e$ (W m <sup>-2</sup> )	$E_q$ (Photons sec <sup>-1</sup> m <sup>-2</sup> )
Radiance L	$\frac{\partial^2 \Phi}{(\partial A * \cos \vartheta) \partial \Omega}$	$L_e$ (W m <sup>-2</sup> sr <sup>-1</sup> )	$L_q$ (Photons sec <sup>-1</sup> m <sup>-2</sup> sr <sup>-1</sup> )
Radiant Intensity I	$\frac{\partial \Phi}{\partial \Omega}$	$I_e$ (W sr <sup>-1</sup> )	$I_q$ (Photons sec <sup>-1</sup> sr <sup>-1</sup> )

## C. BASIC LAWS OF THERMAL RADIATION

### 1. Black Body Radiation

The definition of some important parameters is necessary before addressing the basic laws of thermal radiation. Emissivity of a surface is defined as the "ratio of emitted radiant power from a surface to that emitted from a black body (perfect emitter) at the same temperature" [Ref.3]. Absorptance is defined "as the fraction of incident power absorbed" [Ref.3]. The spectral radiant emittance is the radiant flux leaving an infinitesimal area of surface divided by that area per unit wavelength [Ref.3].

A black body can be defined as a perfect absorber (absorptivity  $\alpha=1$ ). Being a perfect absorber, it must also be a perfect emitter (emissivity  $\varepsilon = 1$ ). According to those



two properties and Kirchoff's Law the Black Body has a reflectance ( $\rho$ ) and transmissivity ( $\tau$ ) of zero. A black body is totally diffuse, radiates at all wavelengths, and at any temperature its spectral radiant emittance is the maximum possible for any real thermal source with the same temperature. In Figure 2 the spectral radiant emittance of a blackbody at various temperatures is presented.

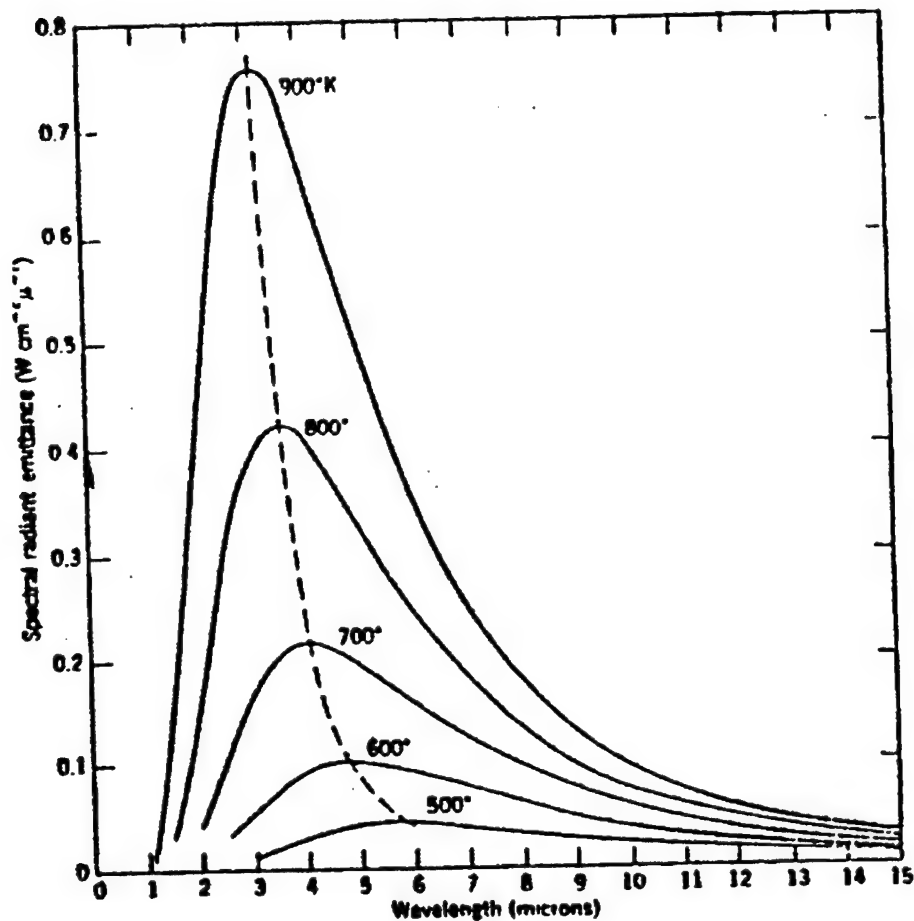


Figure 2 - Spectral Radiant Emittance of a Blackbody at various Temperatures [Ref.3:p.3-3].

## 2. Total Power Law

When there is incident radiation on a body, some of it is absorbed, some of it reflected and some of it transmitted. Thus the ratios of each of those three to the incident power must add to be equal to one:

$$\alpha + \rho + \tau = 1 \quad (2.5)$$

where:

$\alpha$  = Absorptivity (the fraction of incident power absorbed)

$\rho$  = Reflectivity (the fraction of incident power reflected)

$\tau$  = Transmissivity (the fraction of incident power transmitted)

## 3. Kirchoff's Law

A non-Black body in a thermal equilibrium receives but also emits power. Since the system is in thermal equilibrium, the absorbed and emitted powers must be equal. It follows by extension that at any wavelength the emissivity, the fractional efficiency of radiation relative to a black body, must equal the absorptivity.

$$\varepsilon(\lambda) = \alpha(\lambda) \quad (2.6)$$

This expression is a statement of Kirchoff's Law together with the principle of "detailed balance".

#### 4. Planck's Radiation Law

In the late 1890's the German theoretical physicist Max Planck found a single formula that could fit the measurements of  $M_\lambda(T)$ , known as the spectral exitance, over the entire wavelength range. This formula became known as Planck's Radiation Law:

$$M_\lambda(T) = \frac{2\pi c^2 h / \lambda^5}{(e^{\frac{hc}{\lambda kT}} - 1)} \quad (2.7)$$

where:

$M_\lambda(T)$  = Spectral Exitance (Watts/cm<sup>2</sup>/μm)

$\lambda$  = Wavelength (μm)

$k$  = Boltzmann's Constant ( $k=1.38 \times 10^{-23}$  J/K)

$c$  = Light velocity in Vacuum ( $c=2.998 \times 10^8$  m/sec)

$h$  = Planck's Constant ( $h=6.625 \times 10^{-34}$  Js)

$T$  = Source Temperature (K)

Planck came to this result by making two important modifications to the classical theory:

1. The emission of absorption of energy out of a surface is by oscillators (of electromagnetic origin) which can only have certain discrete energies determined by  $E_n = nhf$ , where  $n$  is an integer,  $f$  is the frequency in Hertz and  $h$  is called Planck's constant equal to  $h=6.625 \times 10^{-34}$  Js.

2. The oscillators can absorb or emit energy in discrete multiples of the fundamental quantum of energy given by  $\Delta E = hf$ .

Planck's Law represents with great accuracy the radiation from a surface, and with a table of emissivities allows the calculation of the emittance from a real surface.

Emissivity is defined as the ratio of the radiant exitance or radiance of a given body to that of a black body. The basic definition is in terms of a narrow spectral interval.

Thus the spectral emissivity of a body is defined as:

$$\epsilon_{\lambda} = \frac{M_{\lambda}}{M_{\lambda}^{BB}} \quad (2.8)$$

A material which has an emissivity that is independent of wavelength is often called a gray body. Bodies which have an emissivity which varies with wavelength are often called spectral or colored bodies, or selective emitters.

## 5. Wien's Displacement and Stefan-Boltzmann Laws

Blackbody radiation is theoretically interesting because of its universal character. The radiation properties of the blackbody are independent of the particular material of which the container is made.

The spectral exitance  $M_\lambda(\lambda, T)$  is the total power radiated per unit area per unit wavelength at a specific temperature. From the curves in Figure 3 two important observations should be noted:

1. There is a shift in the maximum towards the shorter wavelengths as the temperature is increased.
2. The total radiated power increases as the temperature increases.

The first of the above mentioned observations is commonly referred to as Wien's Displacement law and is expressed by the formula:

$$\lambda_{\max} T = 2.898 \times 10^{-3} \text{ (m K)} \quad (2.9)$$

Where  $\lambda_{\max}$  is the wavelength of the peak of the spectral distribution at a given temperature.

For the second observation if we integrate the quantity  $M_\lambda(\lambda, T)$  over all wavelengths, the power per unit area at  $T$  is obtained. Josef Stefan found empirically in 1879 and Boltzmann demonstrated theoretically several years later, that  $M(T)$  is related to temperature by:

$$M(T) = \epsilon \sigma T^4 \quad (2.10)$$

This is known as the Stefan-Boltzmann law, with the constant  $\sigma$  experimentally measured to be  $5.6705 \times 10^{-8} \text{ (W/m}^2\text{K}^4\text{)}$ .

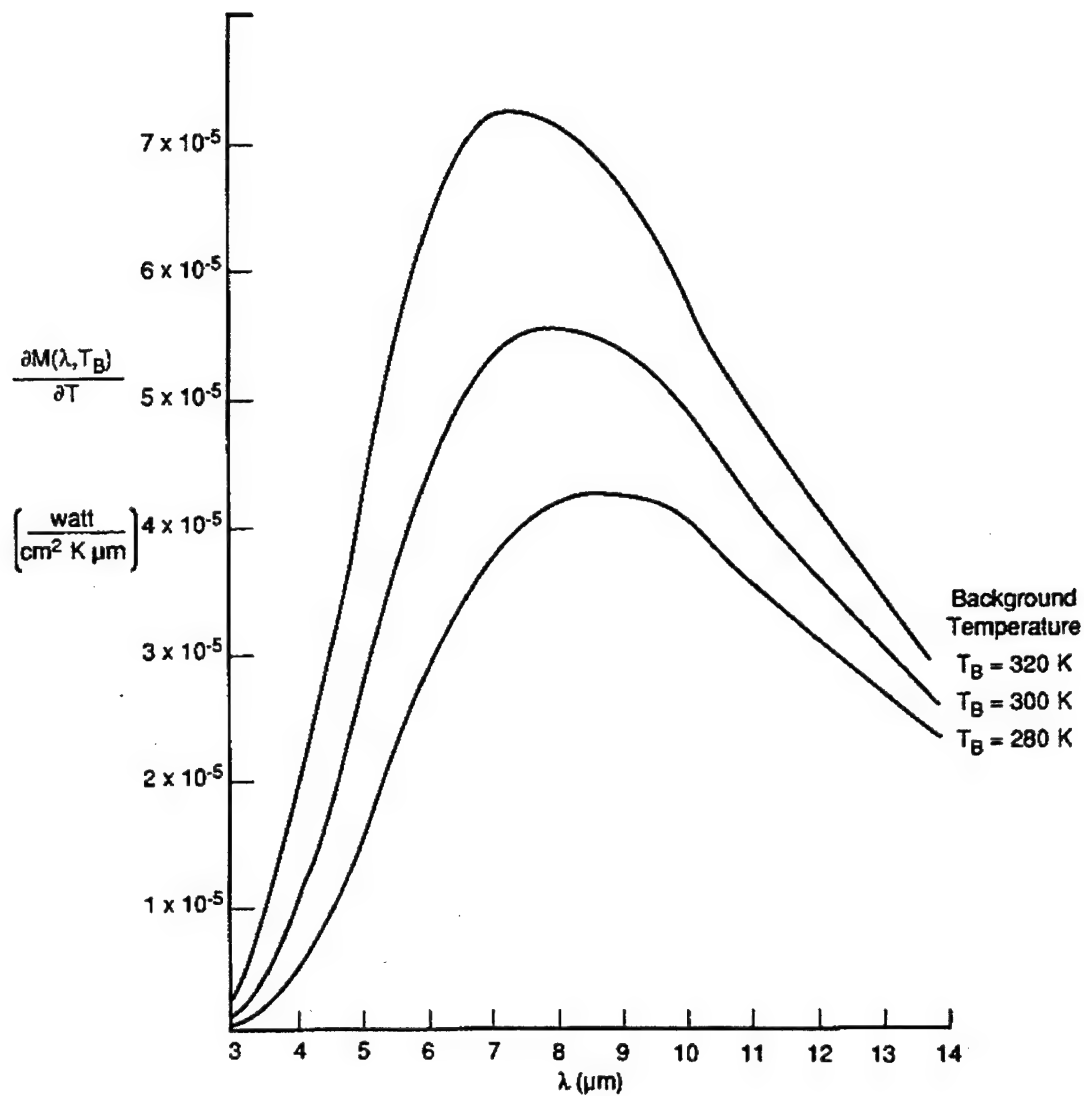


Figure 3 - Spectral distribution of the radiation emitted from a blackbody for different blackbody temperatures [Ref.2].

#### D. ATMOSPHERIC PROPAGATION

The atmosphere is an important consideration regarding the performance of all infrared systems. An infrared system can be described as having three basic components:

the source of the radiation, the propagation medium and finally the detector. Due to the dramatic improvement in the performance of detection systems today, the limiting factor of the overall system performance is often the propagation medium.

Absorption, scattering and turbulence are the dominant mechanisms of loss.

### 1. Absorption

The atmospheric window regions are defined by molecular absorption (primarily water vapor and carbon dioxide). The energy structure of a molecule is composed of discrete energy levels. At optical frequencies, the quantum nature of molecules is very important. Figure 4 illustrates the concept for a two level system. A photon with a frequency  $f_0$ , such that  $E_1 - E_2 = hf_0$  ( $h$  is Planck's constant) is absorbed by the system. Other frequencies do not interact. Energy in this case is absorbed by the molecule (from the photon field) at the frequency  $f_0$ . Thus an absorption spectral line is observed in a very narrow linewidth around  $f_0$  because of the absence of energy relative to the incident photon field.

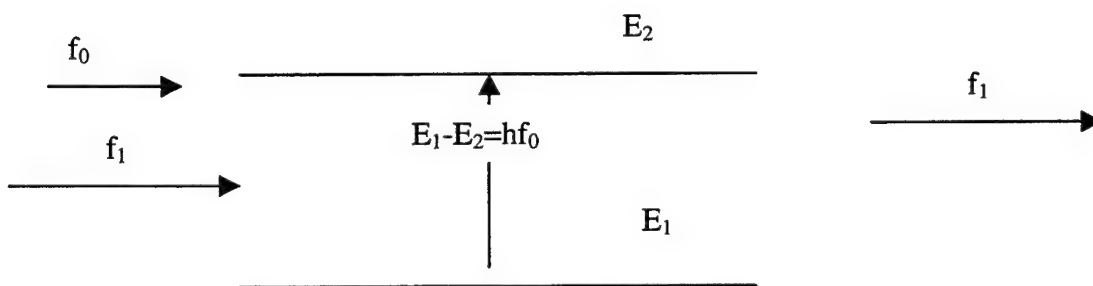


Figure 4 - Photon absorption in a two level system.

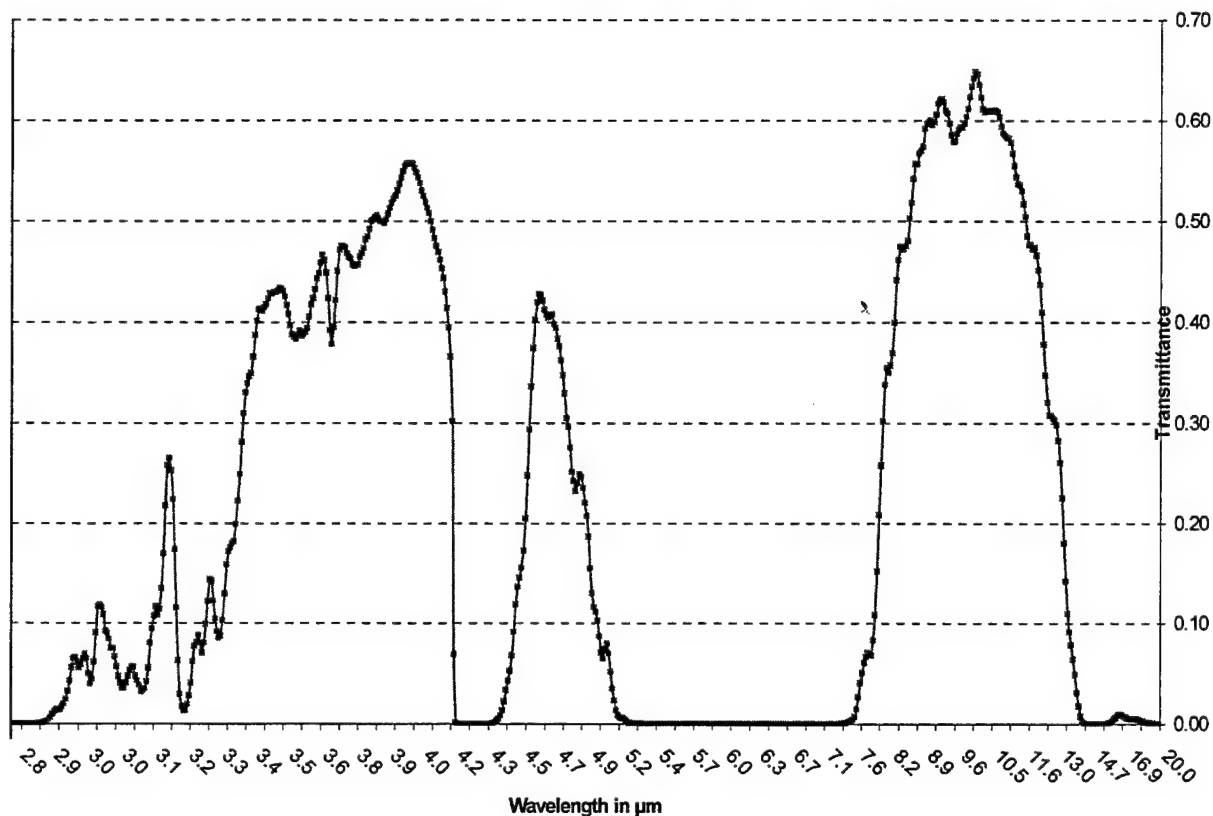


Figure 5 - Atmospheric transmittance for marine aerosol model using the 1976 US Standard atmospheric model for a slant range of 2 km from sea level to 100m height calculated with the SEARAD code.

The plot in Figure 5 shows the infrared "windows" in which systems have to operate. The extinction that is shown is caused by four separate mechanisms that must be considered separately. The total extinction coefficient is the sum of the coefficients for total absorption and total non-forward scattering:

$$\mu = \mu_a + \mu_s \quad (2.11)$$



where:

$\mu_a$  = total absorption coefficient

$\mu_s$  = total non-forward scattering coefficient.

The total absorption coefficient is:

$$\mu_a = k_m + k_a \quad (2.12)$$

where:

$k_m$  = molecular absorption coefficient

$k_a$  = aerosol absorption coefficient.

As for the molecular extinction, the relative values of these coefficients depend strongly on the density and molecular composition of the atmosphere and the composition, number density and size distribution of the aerosols.

## 2. Scattering

Scattering is the process by which the energy in an electromagnetic wave is intercepted and reradiated into  $4\pi$  steradian solid angle. It results from the interaction of the wave field with the electron oscillators in the scattering medium [Ref. 3:p.12-22]. If the energy of an electromagnetic wave does not match the energy of one of the atom's energy state transitions, the atom will scatter the light. So in contrast to the excitation process (absorption) non-resonant scattering occurs with incoming radiant energy of

other frequencies (other than resonant frequencies). So the atoms (or the molecules) of the scattering medium are excited by the incoming wave field, behaving as forced harmonic oscillators which reradiate at the frequency of the incident wave. There is a phase difference in the secondary wave from the primary, however (phase lag), dependent on the difference between the wave frequency and the oscillator resonance frequency. Any inhomogeneity in refractive index can cause scattering (in the atmosphere the component gas molecules, aerosol particles of various sizes, fog, rain and hail drops are all effective scatterers). The spatial distribution of the scattered radiation is strongly dependent on the relative magnitudes of the particle size and wavelength. For particles very small compared to wavelength, the scattering is approximately isotropic. As the ratio of size to wavelength increases, the scattering is basically concentrated into the forward hemisphere. For very large scattering objects forward scattering dominates and secondary lobes develop at other angles in the radiation pattern.

The scattering coefficient that is part of the total extinction coefficient  $\mu = \mu_a + \mu_s$ , can be divided into components due to the molecules of the air and the aerosol particles suspended in it:

$$\mu_s = \sigma_m + \sigma_a \quad (2.13)$$

where:

$\sigma_m$  = molecular scattering coefficient

$\sigma_a$  = aerosol scattering coefficient.

The approximate order of importance in each of the important atmospheric transmission windows is shown in Table 2 [Ref. 3:p.12-9].

Table 2 - Order of Significance of Attenuation Coefficients [Ref. 3:p.12-9].

Atmospheric Window	Wavelength	Attenuation Coefficients in order of importance
Visible	0.39 $\mu m$ to 0.77 $\mu m$	$\sigma_a, \sigma_m, k_a$
Near Infrared (SWIR)	0.77 $\mu m$ to 1.2 $\mu m$	$\sigma_a, k_a, \sigma_m, k_m$
Mid Infrared (MWIR)	3 $\mu m$ to 5 $\mu m$	$k_m, \sigma_a, k_a, \sigma_m$
Far Infrared (LWIR)	8 $\mu m$ to 12 $\mu m$	$k_m, k_a, \sigma_a$

**a) Rayleigh Scattering**

In the small particle region the scattering can be described accurately by the relatively simple theory developed by Rayleigh for small particles. His theory predicts that in this case scattering is proportional to the second power of the volume of the particle and inversely proportional to the fourth power of the wavelength. This describes the scattering by atmospheric molecules.

The attenuation of a light beam due to Rayleigh scattering is expressed by:

$$I = I_0 \exp(-\sigma_m R) \quad (2.14)$$

where:

$I_0$ = irradiance of the original radiation

$I$ = irradiance of the remaining radiation

$\sigma_m$  = Rayleigh scattering coefficient

R= path length.

**b) Mie Scattering**

In 1908 Gustav Mie published a rigorous solution of the scattering problem for homogeneous spherical particles of any size. Although complicated, his solution has great practical value, particularly when applied to colloidal and metallic suspensions, fog and clouds to mention only a few applications[Ref.4:p.294]. Mie scattering includes Rayleigh scattering in the limit of small drop size and non-selective scattering in the large particle limit, where the efficiency factor tends to a constant value close to two.

The transmitted beam irradiance here is similar to Rayleigh scattering and is given by:

$$I = I_0 \exp(-\sigma_a R) \quad (2.15)$$

where:

$I_0$ = irradiance of the original radiation

I= irradiance of the remaining radiation

$\sigma_a$  = aerosol attenuation coefficient (function of aerosol density)

R= path length

## E. POLARIZATION

### 1. Polarization Physics

The polarization of light is one of its fundamental properties, the others being its intensity, wavelength and coherence. Christian Huygens was the first to suggest that light was not a scalar quantity. This vectorial nature of light is called polarization. Light propagating in air or space is a transverse electromagnetic wave. Its electric field is perpendicular to the magnetic field and they both are mutually orthogonal to the propagation direction. In the case that the plane of vibration of the electric vector is spatially fixed, the wave is said to be linearly polarized. Under the conditions where the electrical vector rotates in such a way that an ellipse is created when viewed from the direction of propagation, then it is said to be elliptically polarized (with the special case of circular polarization being included in this general category). The fundamental laws and polarization equations describe the basic parameters of polarization of the sea and sky background as well as the target.

#### *a) Stokes Parameters.*

Sir G. Stokes found that the polarization behavior could be completely represented in the terms of four measurable quantities known as the Stokes polarization parameters. The Stokes polarization parameters for a plane wave are [Ref.5]:

$$I = E_s^2 + E_p^2 \quad (2.16)$$

$$M = E_s^2 - E_p^2 \quad (2.17)$$

$$C = 2E_s E_p \cos \delta \quad (2.18)$$

$$S = 2E_s E_p \sin \delta \quad (2.19)$$

where:

$I$  = the total intensity of the light

$M$  = the intensity of linear s or p polarized light

$E_s$  = the normal to the plane of propagation components of the wave  
electric field

$E_p$  = the parallel to the plane of propagation components of the wave  
electric field

$C$  = the intensity of linear  $\pm 45^\circ$  polarized light

$S$  = the intensity of right or left circular polarization contained within the  
beam

$\delta$  = the phase difference between the s and p components of the E field.

The first parameter ( $I$ ) expresses the total intensity of the optical field and the other three ( $M, C, S$ ) describe the polarization state. Stokes' parameters can be applied not only to completely polarized light but also to partially polarized light and unpolarized light. The degree of polarization is the ratio of the intensities of the polarized to the total intensity:

$$P = \frac{I_{pol}}{I_{tot}} = \frac{(M^2 + C^2 + S^2)^{1/2}}{I}, \quad 0 \leq P \leq 1 \quad (2.20)$$

where:

$I_{pol}$  = the intensity of the sum of the polarization components

$I_{tot}$  = the total intensity of the beam

The effects that result from polarization depend on the emission as well as the reflection properties of the various materials.

#### ***b) Emission Polarization***

The thermal energy emitted by various targets and their background is inherently polarized. For sea targets the emission characteristics of the sea and the sky background is of great importance since a significant contrast improvement can be obtained by filtering off the background.

##### **(1) Sea Emission Polarization.**

The mathematical models describing sea surface polarization are complex and are analyzed in great detail in Reference 6 and 10. What is important for this work is the fact that both emitted and reflected components of the sea surface radiance will show polarization, predominantly in orthogonal directions. For most materials there is only a small range of angles at which elliptical polarization occurs. Even in those cases the phase difference between orthogonal components is small enough (due to small dielectric constants) that an approximation of linearly polarized light at all angles is valid [Ref.7].

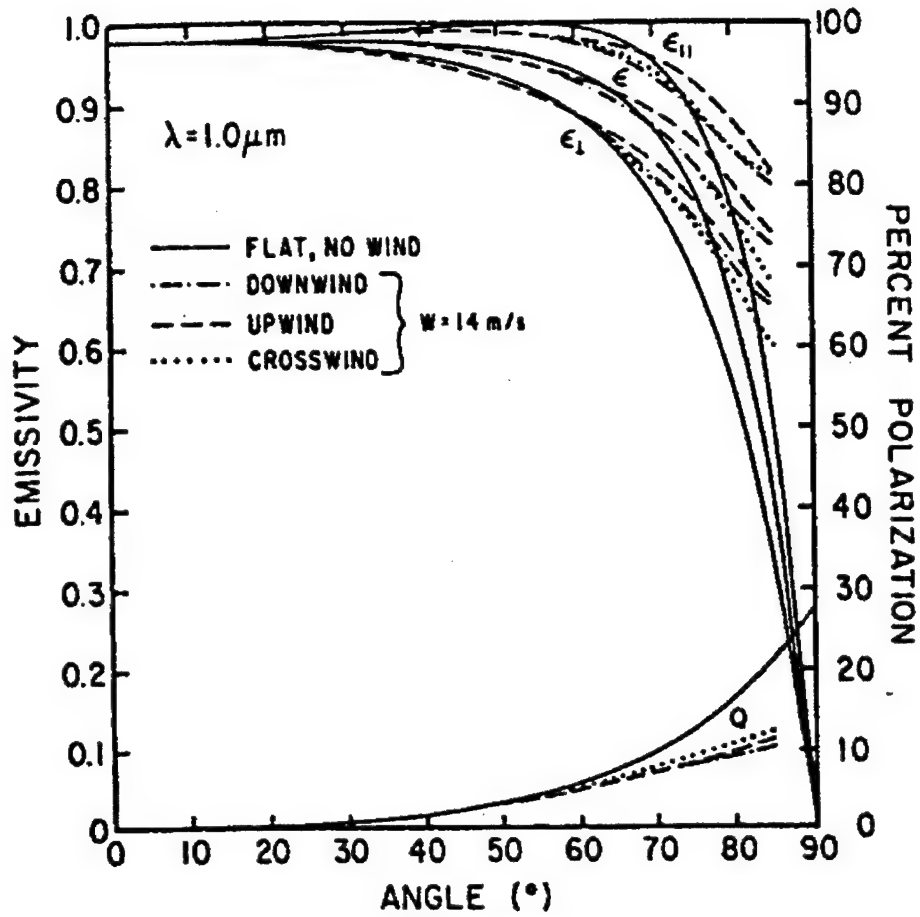


Figure 6 - Sea emissivity and percent polarization for  $\lambda = 1 \mu m$  [Ref.8].

In Figure 6 the polarization of emission for  $1 \mu m$  wavelength and 14 m/sec wind speed is presented [Ref.8]. The percentage of polarization  $Q$  is defined by:

$$Q = 100 \times \frac{\epsilon_{||} - \epsilon_{\perp}}{\epsilon_{||} + \epsilon_{\perp}} \quad (2.21)$$



where:

$\epsilon_{\parallel}$  = emissivity of each facet referred to the horizontal direction

$\epsilon_{\perp}$  = emissivity of each facet referred to the vertical direction.

The results from Figure 6 hold true for all wavelengths less than or equal to  $10\ \mu m$ , excluding the absorption bands [Ref.7]. It should be noted that the maximum values for polarization are observed at angles near the grazing angle.

## (2) Sky Emission Polarization

Infrared radiation emitted from the sky is unpolarized [Ref.9]. As a result there will be no improvement in the contrast measurements when the sky is viewed directly. What should be mentioned though is that when the sky is viewed towards the zenith its emission is less, due to the fact that the atmosphere contains of water vapor and aerosols (absorbers) that do act as good emitters but have smaller numbers densities. So the sky radiance increases along with the zenith angle toward the horizon to that of a blackbody with atmospheric temperature. This is due to the maximum thickness of the atmosphere encountered at these angles [Ref.10].

## (3) Target Emission Polarization

It has been demonstrated that painted surfaces such as those found on ships and other vehicles display emission polarization. In Figure 7 [Ref.11] a series of various paint measurements is presented ranging from very smooth to sand paint mixtures.

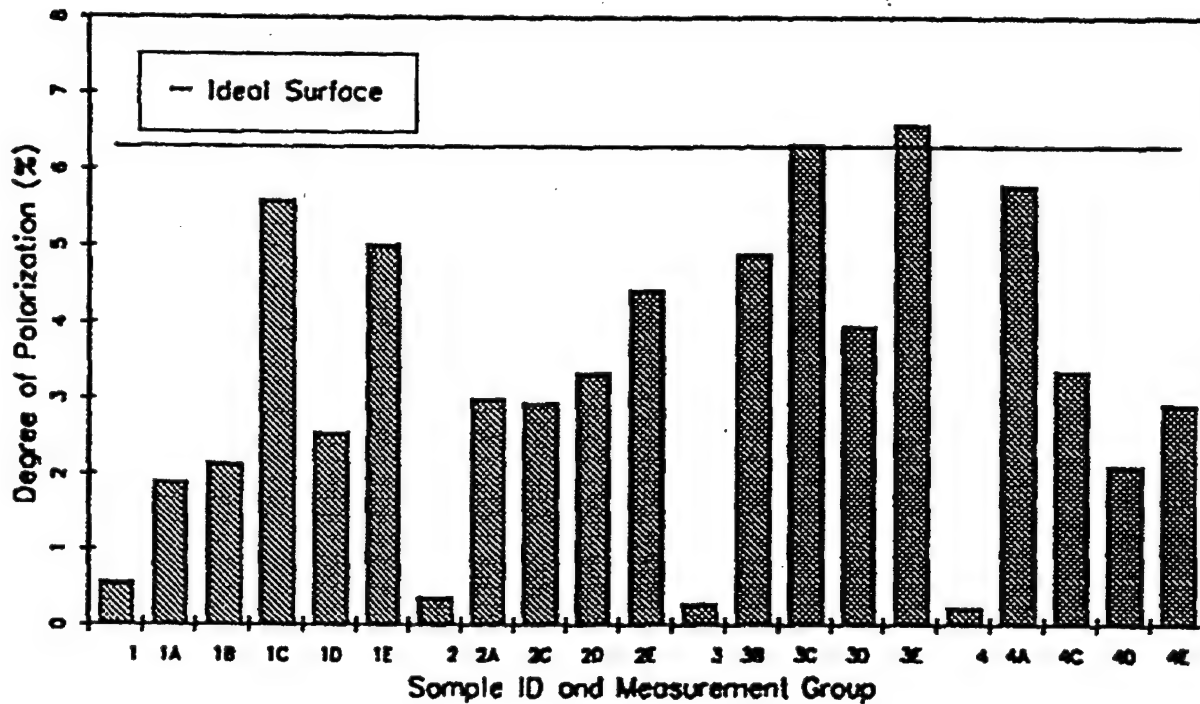


Figure 7 - Measured polarized signature components in the 7.5-12  $\mu m$  band for selected paint samples viewed at 45° from normal [Ref.11].

The line for an ideal surface denotes the degree of polarization that would be seen from a perfectly specular reflector. The rougher the sample the less is the degree of polarization. The degree of polarization depends as well on the index of refraction of the paint and any possible degradation due to the roughness of the surface.

c) *Reflection Polarization*

From the total power law it follows that:

$$\alpha + \rho + \tau = 1 \quad (2.22)$$

where:

$\alpha$  = Absorptivity

$\rho$  = Reflectivity

$\tau$  = Transmissivity

For a perfectly opaque body,  $\tau=0$  so:

$$\varepsilon + \rho = 1 \quad (2.23)$$

The emissivity was treated in Section 2.b.3. The reflectance  $\rho$  will be degraded by the absorption properties of the specific body.

(1) Sea Reflection Polarization

By applying the Fresnel equations to a Cox-Munk sea surface slope distribution the following equations are derived [Ref.8]:

$$\varepsilon_{\perp} = 1 - \rho_{\perp} \quad (2.24)$$

$$\varepsilon_{\parallel} = 1 - \rho_{\parallel} \quad (2.25)$$

$$\varepsilon = \frac{\varepsilon_{\perp} + \varepsilon_{\parallel}}{2} \quad (2.26)$$

$$\rho = \frac{\rho_{\perp} + \rho_{\parallel}}{2} \quad (2.27)$$

$$\varepsilon = 1 - \rho \quad (2.28)$$

The sea surface acts as an opaque body. The percentage polarization due to reflection is given by:

$$\rho = 100 \times \frac{\rho_{\perp} - \rho_{\parallel}}{\rho_{\perp} + \rho_{\parallel}} \quad (2.29)$$

## (2) Sky Reflectance

The sky appears to be a poor reflector due to its very good absorptance (because of the atmospheric water and aerosols).

## (3) Target Reflectance

The total polarization coming from a thermal target will depend on the balance between thermal emission and reflection of incident radiance. The maximum results due to reflection polarization will occur nearer to grazing incident angles.

## 2. Polarization Filtering Techniques

The method of polarizing filter construction has in the past been mainly by using anisotropic crystals or wire grids. The wire grid technique has been applied in recent years by using lithographic techniques. That is, a conducting grid is deposited on a transparent substrate.

In this way the filter will block the incoming radiation with the electric field parallel to the orientation of the grid. That is because the wire grid induces currents that

reflect the part of the incoming wave with an electric field parallel to the wire grid. In order for this process to take place the spacing of the wires in the wire grid must be of the order of the wavelength of the incident radiation.

For the infrared region typical transparent substrates are materials such as Silicon, Germanium and KRS-5 (the substrate for the filters actually used in the experiment) [Ref.26].

## **F. TARGET TO BACKGROUND CONTRAST**

The basic parameter that is used by a system or an operator in order to distinguish between a target and its surroundings is the contrast. The contrast is the difference between the irradiance received from a target pixel and the irradiance received coming from the neighboring background.

There are several definitions and types of contrast used. What is known as inherent contrast [Ref.12], or contrast relative to the background is defined by:

$$C_o = \frac{N_{tgt} - N_{background}}{N_{background}} \quad (2.30)$$

where:

$N_{tgt}$  = irradiance coming from the target

$N_{background}$  = irradiance coming from the background.

An alternative definition of contrast is presented by the following formula:

$$C_o = \frac{N_{igt} - N_{background}}{N_{igt} + N_{background}} \quad (2.31)$$

The absolute contrast is given by:

$$\Delta N = N_{igt} - N_{background} \quad (2.32)$$

When comparing two images, it is useful to quantify the increase or decrease in image contrast improvement. So the improvement factor is defined as:

$$F = \frac{\Delta N_1}{\Delta N_2} \quad (2.33)$$

The contrast improvement factor for polarization over the unpolarized case is given by:

$$F_{pol} = \frac{C_{pol}}{C_{unpol}} \quad (2.34)$$

where:

$C_{pol}$  = contrast of the image scene with polarizer

$C_{unpol}$  = contrast of the image scene without polarizer.

It has been shown that the target to background contrast outside the sun glint corridor can be improved with the use of horizontal polarization filters [Ref.13]. Although there is a reduction of the incoming radiation due to the polarizing filters there was an improvement in the contrast. With the use of a vertically polarized filter much of the predominantly vertical polarized energy coming from the background was rejected.

## **G. FORWARD LOOKING INFRARED SYSTEMS**

A Forward Looking Infrared System (FLIR) is the infrared analog of a visible TV camera [Ref.14]. Its purpose is to detect and process the natural radiation that every material body emits. Planck's laws describe this kind of radiation known as "thermal radiation". The atmospheric transmission windows that allow the transmission of thermal radiation are from  $3\ \mu m$  up to  $5\ \mu m$  (known also as medium wavelength infrared or MWIR) and from  $8\ \mu m$  to  $12\ \mu m$  (known also as long wavelength infrared or LWIR).

It should be made clear that the FLIR uses different principles of operation from systems that operate in near darkness by amplifying the existing visible (or near visible) external radiation due to moonlight, starlight or any other such sources. These systems are known as "night vision devices". Night vision devices are smaller and simpler than the various FLIR devices but they do have certain restrictions such as the fact that they do not work satisfactorily when there is not sufficient light or in the presence of deep shadows. Also their performance is inferior to that of a FLIR in conditions of smoke, haze and dust. The connotation of a FLIR is a system that provides a visible rendition of

the invisible infrared radiation scene [Ref.14:p.105]. This technology has various applications such as missile guidance, threat warning, search and track and others.

The purpose of a FLIR system is to form a real image of the infrared scene, identify the differences in the imaged radiation, and after some signal processing procedure, to create a visible representation of this variation (for the man in the loop systems).

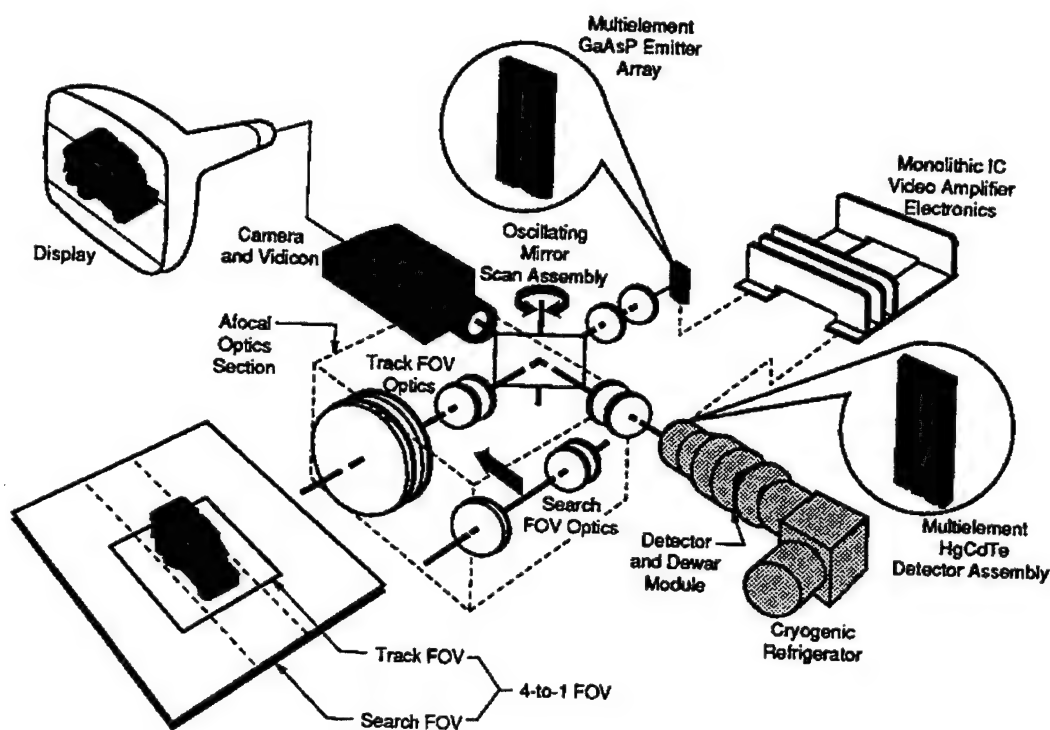


Figure 8 - Modular FLIR concept. Common module systems scan an array of IR sensitive detectors across the target scene. The detector outputs are used to drive a geometrically equivalent array of light-emitting diodes to present a visible representation to a television camera [Ref.14].



In early 1970's the US Department of defense suggested a modular approach to thermal imaging system design. This had as a result the creation of the "common module" components that have influenced military design ever since. The basic philosophy of the common module system was to standardize the basic building blocks of the infrared imaging systems. A first generation common module system is schematically represented in Figure 8 [Ref.14].

These "first generation" common module FLIRS are now being replaced by systems using scanning integrated Focal Plane Arrays. The procedures taking place in an infrared imaging system can be grouped into four basic categories: detection, image formation, signal processing and display.

## **1. Infrared Detection**

There are two ways by which infrared radiation can be detected by its interaction with matter. First through the process of photon exchange, which can produce heating and second by direct electron emission by photon absorption (internal photoelectric effect).

In the photon to phonon exchange process, the radiation is absorbed as heat, resulting in a rise in temperature. This increase in temperature has as a result an effect on some temperature dependent parameter of the detector. This change to a measurable physical parameter is then taken as a reference to indicate the resultant temperature change. These devices are known as square law detectors.

In the process of direct photon absorption, electrons from the valence band of a band gap semiconductor are elevated to the conduction band by direct photon absorption.

This increase in the number of electrons in the conduction band is measurable. These devices are known as quantum detectors.

The most impressive difference between quantum and square law detectors is that the first must be cooled to cryogenic temperatures [Ref.14], because the very small gaps required for infrared photon energies result in very high (to unacceptable) numbers of conduction band electrons at temperatures close to ambient and necessitate operation at 80K or lower. Quantum detectors are therefore mounted to the cold surface of a cooler inside a vacuum enclosure called a dewar. However the sensitivity is greater by more than a factor of 10 than thermal detectors.

## **2. Image Formation**

The electromagnetic radiation laws of reflection, refraction and diffraction for the infrared are the same as for visible light. The concepts and analytical techniques are directly applicable and most visible components have an infrared counterpart [Ref.14:p.112]. While reflective materials for the infrared and visible light are almost the same, refractive elements (such as visible glasses) are not. FLIR optical systems also tend to be bigger than visible systems with the same field of view because of diffraction and sensitivity differences (depending on the ratio  $\lambda / D$ ).

The system used commonly requires an optical scanning subsystem to provide full focal plane coverage with limited number of detector elements [Ref.14]. This is done with the use of a mechanical scanning system, which scans the image across the detector in a prescribed manner. Usually a mirror intersects the optical beam and rotates or rocks

to provide the required scan. Almost all scanning systems use quantum detectors. Thus there are performance considerations that require reducing the background radiation to the minimum possible level. The minimum is the radiation coming from the image background. In order to achieve this the field of view of the detector array must be limited by a cryogenic enclosure. This limiting cryogenic enclosure is called cold shielding. The cold shield must be at low temperature, or else it will add some part of the thermal energy coming from places other than the image scene.

### **3. Image Processing**

"The function of the signal processing of the signal is basically to condition the detector outputs into a form suitable for interface to the display" [Ref.14]. On the other hand the information processing subsystems function is to extract information from the signal processing output. Such functions include preamplification of the detector signal in order to increase the level of the signal and dc level subtraction to eliminate unwanted constant outputs associated with the background radiation.

In the common module systems, each detector output is brought out of the dewar as a separate output. Analog signal processing is used throughout, one channel per detector. Multiplexing and reformatting are done in the subsystem called the electro-optical multiplexer. Then the output of each channel is used to drive a visible Light Emitting Diode (LED) in an array geometrically equivalent to the detector array. Then the diode array is scanned (a task performed by the backside of the infrared scan mirror as is shown in Figure 8) and is focused by a lens (operating in the visible part of the spectrum) to a TV camera.

#### **4. Display**

The display is used as a converter of the signal processing output into a two dimensional visible light presentation of the selected part of the infrared scene. The display could be a standard TV in the form of a cathode-ray tube. Care must be taken in this part as well as the previous mentioned components of the FLIR system, so that there is no degradation in the performance of the system. It must be also mentioned that the display is not a necessary component of all systems since there are applications with no man in the loop. In those systems information does not have to be presented in a form that the human brain is able to understand (i.e. TV image) as it is the case of automated (Automatic Target Recognition) systems.



### **III. EXPERIMENT DESCRIPTION AND SCENARIOS**

In this chapter the experiment and the equipment that was used will be described. The scenarios, including data from the actual experiment that in turn are used for the thesis work, will be also described. The EOPACE data were acquired in April 1996 in San Diego Bay. A total of 5,508 infrared images were taken of the R/V POINT SUR in April 9 and April 10, using an AGA-780 Thermovision camera that was positioned at a building at Point Loma. Internal polarizer filters were used to get sets of images for three different polarization cases (horizontal, vertical and unpolarized). All measurements were taken in the Long Wavelength Infrared band ( $8-12\ \mu m$ ). Meteorological data, Global Positioning System (GPS) data and ship skin temperature data were recorded by instruments installed onboard the ship. In Appendix A a map of the data acquisition area (San Diego Bay) is presented as well as the GPS ship movement during the experiment.

#### **A. EXPERIMENT EQUIPMENT**

##### **1. Internal Polarizing Filtering with the AGA-780**

The camera that was used for the experiment was the AGA-780 Thermovision. It is a two-channel infrared scanning single detector system. It can operate in both the MWIR ( $3-8\ \mu m$ ) and LWIR ( $8-14\ \mu m$ ) bands using liquid nitrogen cooled InSb and HgCdTe detectors, respectively [Ref.15]. The nominal working temperature is 77 K. Scanning is accomplished by two rotating prisms (vertical and horizontal scanning prisms in Figure 9) in each channel which scan the image across the detector yielding 1.1 mrad

geometric resolution. The input lenses for the long wave infrared (LWIR) unit used for the experiments consist of anti-reflection coated germanium. Its optical system is  $f/1.87$ , with a  $7 \times 7$ -degree field of view [Ref.15]. Interchangeable lenses with a  $3.5^\circ \times 3.5^\circ$  FOV are also available.

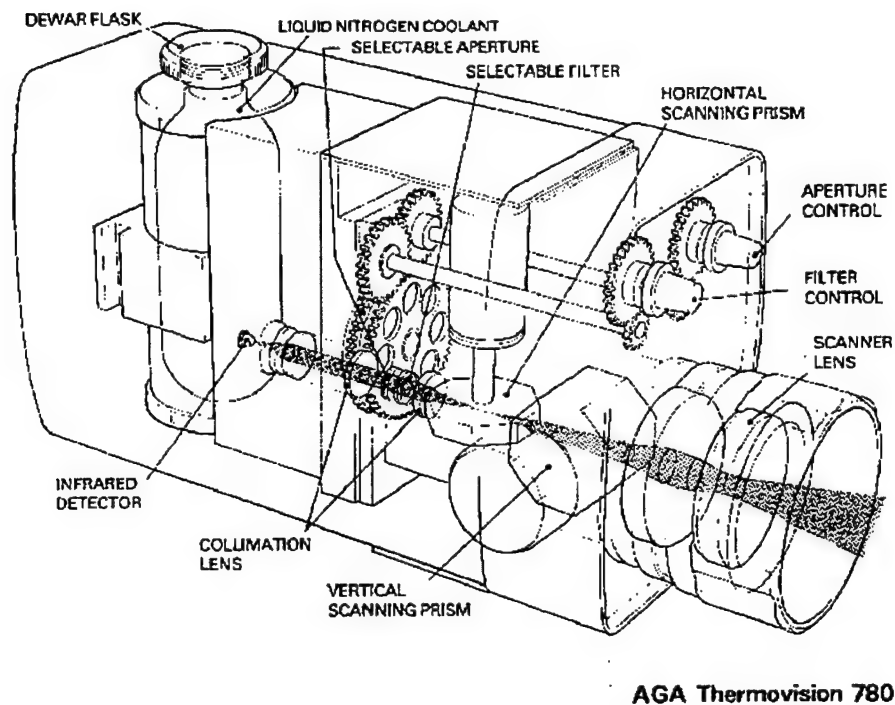


Figure 9 - Internal layout of the AGA-780 Thermovision [Ref.15].

The internal filtering is accomplished after the radiation has passed through the lenses. The polarizing filters (KRS-5) are placed on the selectable filter wheel, between the two components of the collimation lens, inside the camera. The original purpose of the filter wheel was to hold various accessory spectral filters in the optical path, before the radiation reached the detector [Ref.15]. Polarization measurements with the AGA-780

require sequential images with adjacent filter wheel positions inserting vertically and horizontally polarized filters. The requirement of turning the filter wheel in order to use the different polarizer filters is the reason for the sequential nature of the imaging procedure during the experiment.

The two polarizing filters that were used each consisted of an aluminum grid superimposed on a 9.5mm diameter x 3mm thick round KRS-5 substrate manufactured by Graseby-Specac (Suffolk, England). The performance specifications provided with the filters are shown in Appendix B. The different traces numbered there as 1, 2 and 3 represent power transmitted with the grid vertical, horizontal and with the two grids from the two filters crossed, relative to the electronic vector of the incoming radiation. The determination of the parallel and perpendicular transmittances for the filter requires the use of a spectrometer which itself includes internal polarizing reflections. So it must be done by measuring the transmittance two times, with the grid in two orthogonal orientations. These two measured transmittances are designated  $E_v$  and  $E_h$ . The corresponding transmittance of the camera is measured without the grid in place as  $E_0$  and the transmittance for two crossed grids as  $E_1$ . From these quantities the grid transmittances are given by:

$$K_1 = \frac{E_h + E_v}{E_0} \quad (3.1)$$

$$K_2 = \frac{E_1}{E_h + E_v} \quad (3.2)$$



The manufacturer provided those quantities for each filter. It must be also mentioned that according to the manufacturer, for the traces in Appendix B the spectrometer output was normalized such that  $E_0=1.00$  (100%) for all wavelengths.

## **2. Research Vessel POINT SUR**

Research Vessel (R/V) POINT SUR is owned by the National Science Foundation (NSF). It is operated for the Central California Oceanographic Cooperative (CENCAL) by Moss Landing Marine Laboratories, which is on Monterey Bay. Its equipment consists of the necessary navigational, laboratory and mechanical facilities that support biological, geological, chemical and physical oceanographic research. For the purposes of this project it was used as a target for infrared imaging as well as for atmospheric sampling functions. In the Appendix C are presented the ship's general characteristics and dimensions (R/V POINT SUR Cruise Planning Manual).

## **3. Software**

### ***a) CEDIP PTRWIN***

The analog data provided by the scanning detector were digitized for display, recording and measurement by PTRWIN version 3.16 from CEDIP. This data acquisition and analysis software uses a 12-bit A/D converter for converting the detector signal intensity into a real-time image on a computer screen and for digital image recording. In addition, the PTRWIN software was used as a visualization tool to select images to be analyzed. Although PTRWIN also offers good analysis tools, it works

interactively analyzing only one image a time [Ref.16]. Following the process developed for a previous thesis [Ref.16], other software will be used for the analysis and data retrieved from the collected images.

***b) Interactive Data Language***

IDL (Interactive Data Language) is a complete computing environment for the interactive analysis and visualization of data. IDL integrates an array-oriented language with numerous mathematical analysis and graphical display techniques [Ref.17]. The image analyses in this project were performed using programs written in IDL 5.0.3 from Research Systems Inc., Boulder, CO. The programs used were originally written or adapted for the purpose of another thesis [Ref.16] and then modified to suit the needs of this work.

***c) SeaRad***

SeaRad is a modified version of the U.S. Air Force program MODTRAN2, which predicts the sea radiance (brightness) for any viewing geometry in the spectral range from  $52.63 \text{ cm}^{-1}$  to  $25000 \text{ cm}^{-1}$  in addition to transmittance and path radiance. The particular SeaRad code used for this thesis can also be used to predict the polarization of sea radiance [Ref.28].

Sea radiance is modeled by combining the methods of geometrical optics with the Cox-Munk statistical description for wind driven ocean capillary waves. The model is incorporated into the atmospheric transmittance/radiance code MODTRAN2 to provide numerical sea radiance predictions. In the model each individual capillary wave

facet is allowed to reflect the sky or sun and emit thermal radiation. The total radiance from the sea is obtained by applying the proper statistical weight to each facet and integrating it over all facets within the observer's field of view [Ref.18]. SeaRad operates exactly like the original MODTRAN2 code except that a new logical parameter (Sea Switch) is required in the input file (tape). Sun glint is included in the sea radiance prediction provided that the user has chosen to execute SeaRad in radiance mode with solar scattered radiance included (IEMSCT=2).

It should be mentioned that preliminary comparisons show that SeaRad agrees to within a few degrees Celsius with the actual sea radiance measurements in the mid and long-wave infrared bands. Appendix D provides an example of how SeaRad is used to predict ocean radiance.

## **B. THE EXPERIMENT**

The experiment was conducted in San Diego Bay at Point Loma. The basic instruments in the experiment setup were the sensor (camera AGA-780 Thermovision) and the target (R/V POINT SUR). The camera was located at building 15 in NRaD, Point Loma with coordinates N 32° 39' 36", W 117° 14' 22". The ship positioning was planned to correspond to a pattern of radial bearings with stationary points spaced at 0.5 nmi intervals. At each stationary point, the ship should maneuver to be at different heading for each image sequence (3 polarization cases) taken. Both ship GPS location and sensor position are known, so the bearing is computed. From ship heading and bearing

information, the target aspect angle can be calculated. In Appendix A the area of the experiment is presented.

## **C. DATA**

### **1. Images**

The images were recorded sequentially for the three polarization cases: horizontal, vertical and unpolarized. An average of 26 images (frames) was taken for each polarization case. Horizontal and vertical cases were recorded in the same file and each unpolarized case was recorded in a different file. The frames are composed of 4 interlaced fields with dimensions 125x64 pixels each. Therefore, each frame is an array of 125x256 pixels. Image data taking was implemented with the AGA-780 mounted on a remotely controlled pan-tilt head outside the south looking window of Building 15 on Point Loma. The data were digitized and recorded with the PTRWIN acquisition boards installed in the docking station of an NEC laptop computer. For storage, the files were transferred to a second portable computer and stored on optical disk. The original image files from PTRWIN are identified by the extension \*.PTW [Ref.16].

With the use of the modified program BASEGEN.PRO (written in IDL) from Ref.16, 140 original image files were converted into basic image files (\*.PTE). The basic files were named sequentially using the name BASE followed by a number. For this thesis data for the scenarios were taken from file BASE33.PTE due to the time proximity with radiosonde data, that in turn were used for the construction of the atmospheric

model in SeaRad. The structure of the basic files for the three polarization cases is presented in Table 4.

Table 3 - Original Image Files (\*.PTW) Structure [Ref.16].

<b>DATA</b>		<b>OFFSET (bytes)</b>
<b>Main Header (65,536 bytes)</b>	General Parameters	0
	Scanner Parameters	44
	Display Parameters	245
	Digitalization Parameters	375
	Comments	563
	Setup File Name	1563
<b>1st Frame Header (1,536 bytes)</b>	Level	0
	Time	80
	Comments	180
<b>1st Frame (64,000 bytes)</b>	1st Field	0
	2nd Field	16,000
	3rd Field	32,000
	4th Field	48,000
<b>2nd Frame Header (1,536 bytes)</b>	Level	0
	Time	80
	Comments	180
<b>2nd Frame (64,000 bytes)</b>	1st Field	0
	2nd Field	16,000
	3rd Field	32,000
	4th Field	48,000
The Frame Structure above is repeated until the last frame in the image sequence.		

Table 4 - Basic Files (\*.PTE) structure. [Ref.16].

Variable	Type
Name of original (*.PTW) file	string (20)
Information vector	integer (1,13) <sup>1</sup>
Frame time : horizontal polarization	integer (4, # frames hor. case)
Frame time : vertical polarization	integer (4, # frames ver. case)
Frame time : unpolarized	integer (4, # frames unp. case)
Image set (frames) : horizontal polarization	integer (125, 256, # frames hor. case)
Image set (frames) : vertical polarization	integer (125, 256, # frames ver. case)
Image set (frames) : unpolarized	integer (125, 256, # frames unp. case)
Results : horizontal polarization	float (100, # frames hor. case)
Results : vertical polarization	float (100, # frames ver. case)
Results : unpolarized	float (100, # frames unp. case)

## 2. Meteorological Data

The NPS Boundary Layer Meteorology Group collected meteorological data on two meteorological towers (METOC 1 and METOC 2) installed onboard the ship. The data were recorded every 30-seconds. Ship GPS data are included in the METOC files. Also radiosonde data were collected every four to five hours. Appendix E describes and presents the format used to record the data collected on the ship as well as the radiosonde data. The two meteorological towers were located onboard the ship in the following configuration: METOC 1 tower was above the ship bridge (approximately 38 ft above sea

---

<sup>1</sup> In IDL, the first matrix index is column number and the second is line number.

surface) and METOC 2 tower was at the ship bow (approximately 24 ft above sea surface).

### **3. Ship Skin Temperature Data**

The skin temperature of the ship was measured with 16 thermistors installed by NPS-NACIT at different points on the ship. Measurements were taken and recorded every 20 seconds. In Appendix C is presented the position for each thermistor onboard the ship and the format used to record the data.

## **D. SCENARIOS**

For the simulation two scenarios were designed. The target used was an equivalent parallelepiped with the dimensions (length, width and height) of R/V POINT SUR. The sensor simulated has the generic characteristics of a Common Module Forward Looking Infrared sensor (FLIR). The characteristics are given in chapter IV.

For the scenarios it was assumed that the FLIR was mounted on an aircraft. The aircraft approached the target in level flight at two different heights: 100m and 1000m. A schematic representation of the scenarios is presented in Figure 10. For the input characteristics to the atmospheric model used in SeaRad the data from the meteorological measurements (basically the radiosonde) were used. The temperature of the hot spot of target (R/V POINT SUR) was obtained from image file BASE33.PTE with the assistance of some programs in IDL. Those programs were initially written for the purposes of Ref.16 and then modified to suit the needs of this thesis.

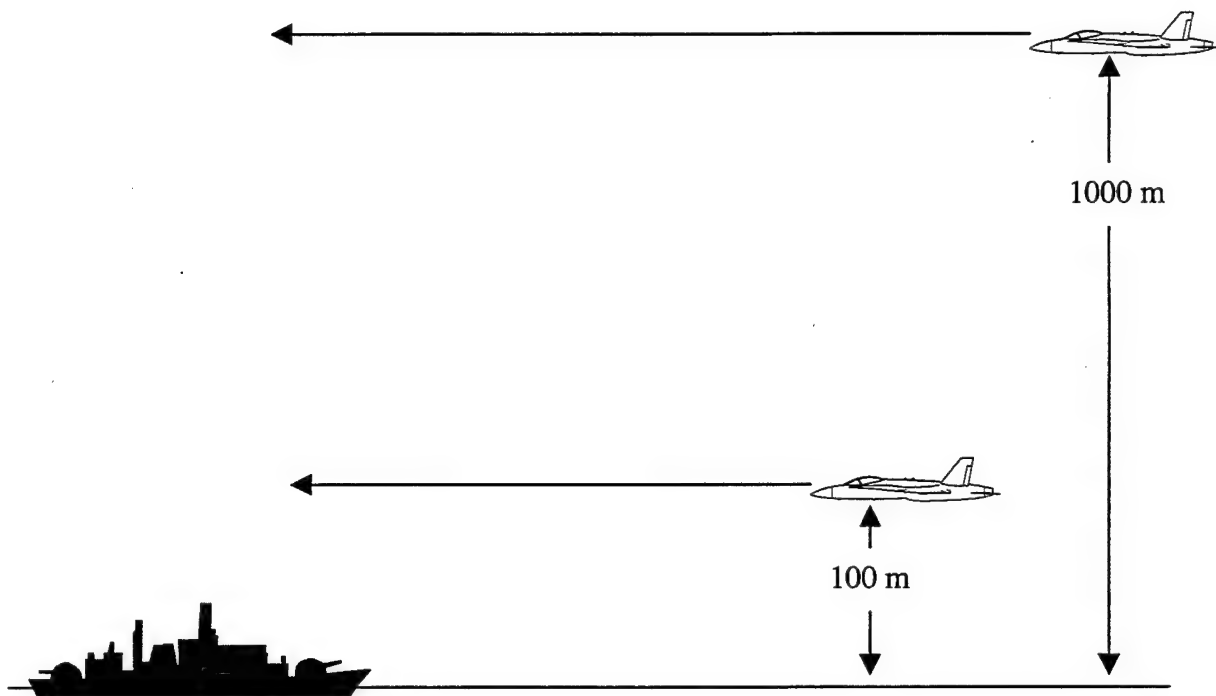


Figure 10 - Schematic representation of the scenarios.





#### IV. SYSTEM PERFORMANCE FIGURES OF MERIT AND DETECTION CRITERIA

In this chapter the FLIR system performance figures of merit, the apparent temperature difference and the various detection criteria will be presented.

##### A. FLIR PERFORMANCE MEASURES.

###### 1. Noise Equivalent Temperature Difference

Noise Equivalent Temperature Difference (NET or NETD) is a useful expression for the sensitivity of a thermal system. It is the temperature difference, referenced to 300 K, between a large target (a square that is at least ten times the detector angular subtense) and the background, which is required to produce a peak signal-to-rms- noise of one at a particular point in the signal processing chain [Ref.2].

The NET is an excellent diagnostic tool for production testing to verify sensitivity. It is, none the less, a poor system to system comparison parameter and should be used cautiously when comparing systems built to different designs. That is because NET is a function of spectral responsivity and the noise equivalent bandwidth [Ref.12].

The form of NET is given in Ref.19 as:

$$NET = \frac{(\Delta f_n)^{1/2} 4(f/\#)^2}{\pi \tau_o \tau_A A_d^{1/2} N_s^{1/2} \int_{\Delta \lambda} \frac{\partial L_\lambda}{\partial T} D_\lambda^* d\lambda} \quad (4.1)$$

where:

$L_\lambda$  = spectral radiance ( $\text{W cm}^{-2} \text{sr}^{-1} \mu\text{m}^{-1}$ )

$f/\#$  = system effective  $f/\#$

$\tau_o$  = optics transmission

$\tau_A$  = atmospheric transmission over the laboratory path

used to make measurement

$A_d$  = detector area ( $\text{cm}^2$ )

$N_s$  = number of detectors in series

$\Delta\lambda$  = spectral band ( $\mu\text{m}$ )

$\frac{\partial L_\lambda}{\partial T}$  = derivative with respect to temperature of the

spectral radiance

$D_\lambda^*$  = spectral detectivity ( $\text{cm Hz}^{1/2} \text{W}^{-1}$ )

$\Delta f_n$  = electronic noise bandpass

A drawback in the use of NET as a figure of merit is the fact that it does not include display or observer response characteristics. So NET does not relate directly to human performance.

*a) Minimum Detectable Temperature Difference*

Minimum Detectable Temperature Difference (MDT or MDTD) is a laboratory measurement of a thermal system's sensitivity, which includes a human operator (unlike NET).

MDT is the apparent temperature difference between a square (or circular) target and a uniform background, required for the detection of the square (or circular) target by a trained observer viewing through a FLIR. There are no time constraints in the observation process and the location of the target is approximately known to the observer [Ref.2]. MDT is measured for a set of targets of increasing area and is usually plotted as  $\Delta T$  versus  $1/(\text{target area})^{1/2}$  as in Figure 11. It can be observed from Figure 11 that the curve is not asymptotic for small targets since an increase in temperature can make even a very small target detectable, even when the angular subtense is smaller than the instantaneous field of view (IFOV) of the detector.

Shumaker, Wood and Thacker give a formula for MDT as [Ref.21]:

$$MDT(v) = \frac{(SNRT)(NET)(\Omega_T + r_s^2)(\Delta x \Delta y)^{1/2}}{\Omega_T \left[ \frac{\pi}{4} (r_s^2 + r_B^2 + \Omega_T) t_e F_r N_{os} N_{ss} \right]^{1/2}} \quad (4.2)$$

where:

$SNRT$  = signal to noise threshold

$NET$  = noise equivalent temperature difference

$\Omega_T$  = target angular subtense ( $\text{mrad}^2$ )

$r_s$  = system resolution (mrad)

$\Delta x$  = in scan detector subtense (mrad)

$\Delta y$  = cross scan detector subtense (mrad)

$r_B$  = back end resolution (mrad)

$t_e$  = eye integration time in seconds

$F_r$  = frame rate in Hz

$N_{os}$  = overscan ratio

$N_{ss}$  = serial scan ratio

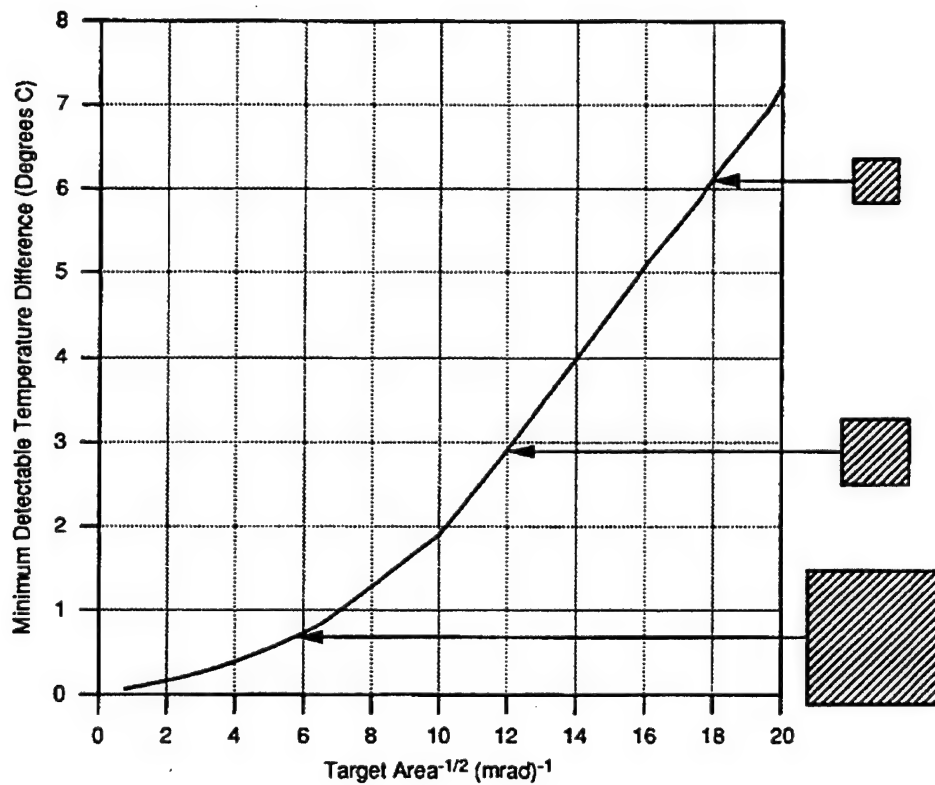


Figure 11 - Typical plot of MDT showing relative sizes of the MDT pattern [Ref.2:p.81].

***b) Minimum Resolvable Temperature Difference***

Following previous work on television systems Lloyd and Sendall [Ref.20] developed the thermal imaging system performance measure, Minimum Resolvable Temperature Difference (MRT or MRTD).

MRT is a noise limited threshold measure of system spatial resolution and thermal sensitivity, in which the characteristics of the human observer are included (thus making it a subjective measurement). It is defined as the temperature difference between a uniform background and the bars of a four bar pattern, each bar having a 7:1 aspect ratio (so the overall pattern will be a square), which is required by a trained observer to just resolve all four bars when viewing the pattern through the imager [Ref.2]. An example of an MRT plot is displayed in Figure 12.

As can be seen from Figure 12, the temperature difference that is needed to resolve the four bars increases as the bars get smaller. The MRT curve is finally asymptotic at a spatial frequency near  $\Delta x^{-1}$  (unlike MDT), since even very large temperature differences will not allow resolution of the four bar patterns where one cycle of the bar pattern is smaller than a detector angular subtense.

Shumaker provides a formula for the MRT [Ref.21:p.8-52]:

$$MRT(\nu) = \frac{2 \times SNRT \times NET \times \rho_x^{1/2}}{MTF_s(\nu)} \left[ \frac{\nu^2 \Delta x \Delta y}{L} \right]^{1/2} [t_e F_r N_{os} N_{ss}]^{-1/2} \quad (4.3)$$

where:

$SNRT$  = signal to noise threshold

$NET$  = noise equivalent temperature difference

$\rho_x$  = noise filter factor

$\nu$  = spatial frequency for which MRT is desired

$\Delta x$  = in scan detector subtense (mrad)

$\Delta y$  = cross scan detector subtense (mrad)

$MTF$  = modulation transfer function

$L$  = length to width ratio of the bar (7)

$t_e$  = eye integration time in seconds

$F_r$  = frame rate in Hz

$N_{os}$  = overscan ratio

$N_{ss}$  = serial scan ratio

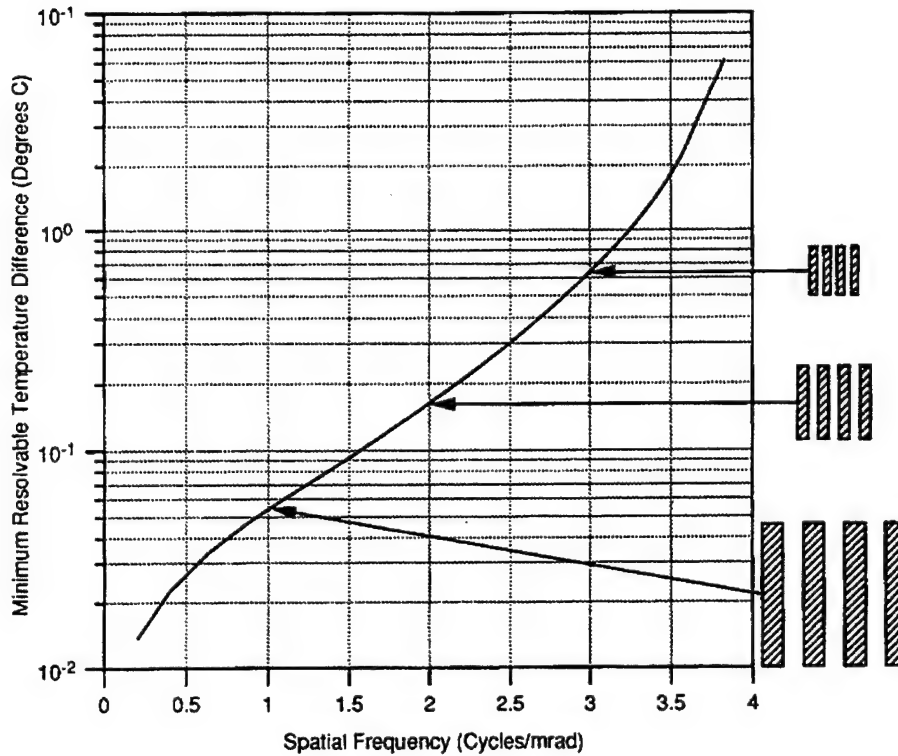


Figure 12 - A typical MRT plot indicating the sizes of the MRT four bar pattern at various spatial frequencies [Ref.2:p.82].

In Ref.21 is also provided another formula for the Noise Equivalent Temperature Difference, which can be derived from the formula that was presented earlier:

$$NET = \frac{10(FOV_x FOV_y F_r N_{os} N_{ss})}{(\pi N_D n_{sc})^{1/2} D \Delta x \Delta y D^{**} n_{sc} \frac{\partial N}{\partial T} \tau_o} \quad (4.4)$$

where:

$FOV_x$  = in scan field of view in mrad



$FOV_y$  = cross scan field of view in mrad

$F_r$  = frame rate in Hz

$N_{os}$  = overscan ratio

$N_{ss}$  = serial scan ratio

$N_D$  = number of detectors

$n_{sc}$  = scan efficiency

$\Delta x$  = in scan detector subtense (mrad)

$\Delta y$  = cross scan detector subtense (mrad)

$D$  = aperture diameter in meters

$D^{**}$  = band average detectivity in  $\text{cm Hz}^{1/2}/\text{W}$

$\frac{\partial N}{\partial T}$  = derivative of Planck's equation in  $\text{W/cm}^2 \text{ K Sr}$

$\tau_o$  = transmission of the optics

## B. APPARENT TEMPERATURE DIFFERENCE COMPUTATION

The temperature difference  $\Delta T$  between a target and its background is defined for zero range  $\Delta T_o$  (no attenuation). When the energy from the target and its background is modified by the atmosphere in the path between the target and the sensor, then it is known as the apparent temperature difference ( $\Delta T_{app}$ ).

There are two basic ways to compute the apparent temperature difference. One is to assume that the contrast temperature difference is attenuated in the same fashion as the radiance:

$$\Delta T_{app} = \Delta T_o e^{-\mu R} \quad (4.5)$$

where:

$\Delta T_{app}$  = apparent temperature difference at range R

$\Delta T_o$  = zero range temperature difference

$\mu$  = extinction coefficient

R = range

The use of equation 4.5 for the computation of the apparent temperature difference is a very simple method, frequently used, and its results are not very accurate.

Another method is to convert the temperature difference into in-band background radiance and target radiance, compute the corrections for attenuation and path radiance by using a specific code (i.e. LOWTRAN, MODTRAN, SEARAD) and reconvert to an apparent  $\Delta T_{app}$  as a function of range. This method is much more accurate than the previous one and will be used for this thesis along with the results from the SEARAD propagation code.

For the conversion of the temperature difference into in-band background radiance and target radiance a program written in MATLAB was used (rad.m). The code is provided in Appendix F. This program performs a numerical integration of Planck's

law over the bandwidth and provides lookup tables that associate temperature with radiance.

The target's temperature was obtained from the file BASE33.PTE with the assistance of the modified program Hotspot.pro (written in IDL). The modified Hotspot.pro located the hot spot of the target and provided the temperature in degrees Kelvin. Then this temperature was converted to radiance with the program rad.m.

A model of the specific atmospheric conditions from the radiosonde data from the experiment (Appendix E) was inserted in SEARAD (Appendix D) as well as the geometry for the two scenarios. The above data provided a set of polarized and unpolarized values for the transmittance, path radiance and background radiance. The transmittance multiplied by the ship radiance and with the addition of the path radiance provided the total ship and path radiance at the sensor. This radiance was then converted to temperature with the use of the Planck formula for the in-band radiance. The calculation was performed by the rad.m program (Appendix F).

The full range background radiance for the specific geometry (thus a specific range) was also converted to temperature. This temperature was then subtracted from the total ship and path radiance, providing the apparent temperature difference  $\Delta T_{app}$  for the specific range.

For the same calculations with polarization the values of the full range background radiance and the ship and path radiance were multiplied by a factor of 0.7 and 0.5 respectively to compensate for the attenuation of the energy passing through the polarizing filter. The analytical calculations of the above factors of 0.7 and 0.5 are

presented in Appendix B. These numbers represent the amount of in-band energy that passes through the polarizer filters for the cases of horizontally polarized and unpolarized waves.

### **C. DETECTION CRITERIA AND PROJECTED AREA OF THE SHIP**

The initial task in every system is to search the field of view to locate the target. The search pattern varies from system to system and also with the observer training and background. The following step is finding the target. D'Agostino and Moulton introduced the "minimum findable temperature difference" (MFTD) [Ref.23]. "In this process the target might be anywhere in the field of view. When the target is located, then attention is focused on a particular area of the scene. This process is more complex than the minimum detectable temperature (MDT). The MDT is the ability to detect a blob in noise with the target in the center of the field of view. Both the MDT and MFTD are functions of the target angular subtense" [Ref.12].

After finding the target a specific set of criteria have to be applied to provide the required amount of detail for detection, recognition and identification (detection, recognition and identification are just three discrimination levels in a continuum). The definition of each level depends on the author (since each author has tried to describe his impression of discrimination ) [Ref.12]. Typically used levels of target discrimination are listed in Figure 13.

Because of the difficulty of the description of a target mathematically, for measurement of the capability of the FLIR aided eye to detect (in a broad sense) a target,

two types of simple targets are used: isolated rectangles and periodic bar patterns. The first step is the detection of isolated rectangles and the second is the resolution of bars in a bar pattern.

<b>TASK</b>	<b>DESCRIPTION</b>	<b>EXAMPLES</b>
Pure Detection	Something-Nothing Decision	Object vs. Noise
Discrimination Detection	Potential Target vs. Background Decision	Target vs. Background
Orientation	Determining the Direction of the Long Axis of the Target	Side View vs. Front View
Classification	Distinguishing Potential Targets from Similarly Sized Non-Targets	Warship vs. Merchant Ship Tracked vs. Wheeled Vehicle
Recognition	Distinguishing the Target from Similarly Classed Military Objects	Destroyer vs. Cruiser Tank vs. APC
Identification	Determining the Specific Military Designation	Kashin vs. DD963 Destroyer
Unit Identification	Determining the Identity of the Specific Object	USS Kennedy vs. USS Forrestal

Figure 13 - Discrimination levels [Ref.21:p.2-3].

The first task is described as "aperiodic detection" and is characterized by the FLIR parameter Minimum Detectable Temperature (MDT). The second task is described as periodic detection and is characterized by the FLIR parameter Minimum Resolvable Temperature (MRT).

This simplified analysis has proven widely usable as an analytical approach and it is customary to describe all visual tasks by equating them to one of the two problems above for which mathematical solutions have been developed. Generally pure detection is equated to detection of an isolated rectangle, with area equal to the target area, and whose

temperature difference with the background is set equal to the average temperature difference of the real target and its background.

For the other discrimination tasks, the targets are related with bar chart patterns whose temperature difference between the hot and cold bars is equal to the average temperature difference of the real target and its background and whose spatial frequency is determined by the target's critical dimension and the difficulty of the visual task attempted [Ref.21]. This procedure is illustrated in Figure 14. In the case where a specific feature must be detected for the discrimination task, then its area alone may be equated to an idealized target.

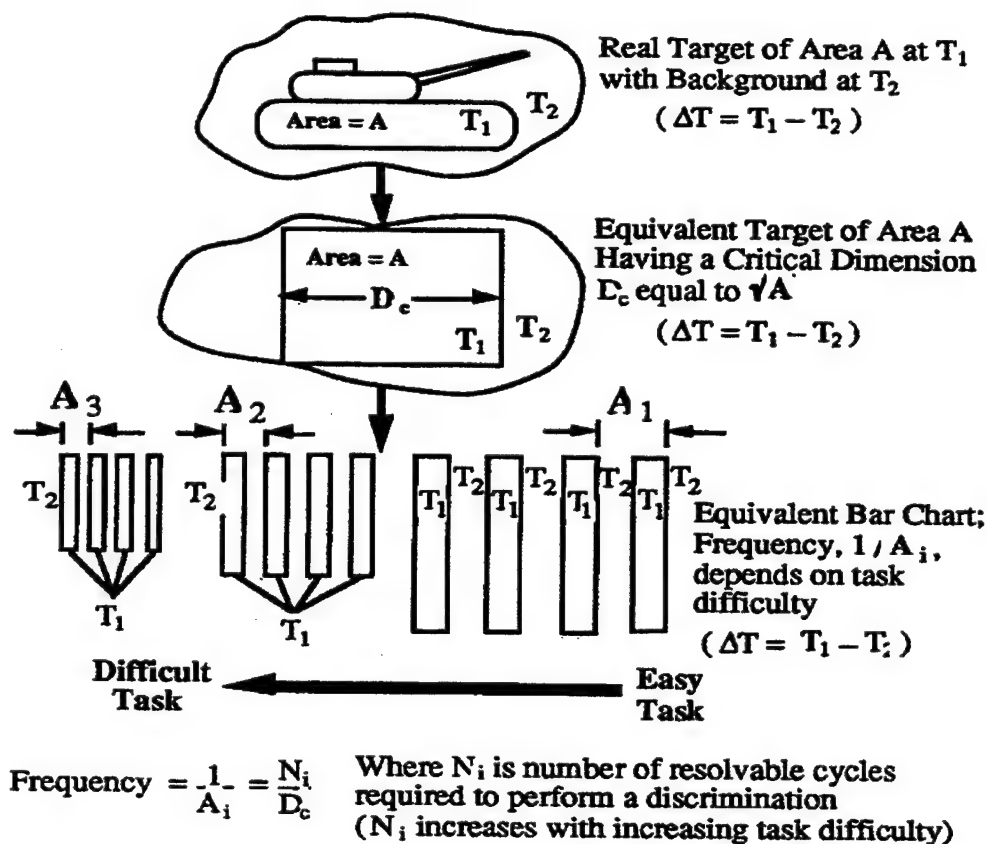


Figure 14 - Target task transform [Ref.21:p.2-5].

## 1. Visual Discrimination Criteria

There have been only a few experiments designed to relate the resolution of bar charts to levels of visual discrimination. The classic experiment was conducted in 1957 by Johnson [Ref.24] for application to image intensifier systems. The results from that experiment are presented in Table 5 and are known as the "Johnson Criteria" [Ref.21].

Table 5 - Johnson criteria

TARGET (BROADSIDE)	RESOLUTION PER MIN. DIMENSION (LINE PAIRS)			
	DET.	ORIENT.	RECOG.	IDENT.
Truck	0.90	1.25	4.5	8.0
M-48 Tank	0.7	1.2	3.5	7.0
Stalin Tank	0.75	1.2	3.3	6.0
Centurion Tank	0.75	1.2	3.5	6.0
Half-Track	1.0	1.50	4.0	5.0
Jeep	1.2	1.50	4.5	5.5
Command Car	1.2	1.5	4.3	5.5
Soldier (Standing)	1.5	1.8	3.8	8.0
105 Howitzer	1.0	1.5	4.8	6.0
AVERAGE	1.0 ± 0.25	1.4 ± 0.35	4.0 ± 0.8	6.4 ± 1.5

Later Moser concluded that the Johnson Criteria could not be simply extrapolated to ship targets [Ref.25]. Following a study with ship silhouettes he concluded that the minimum ship dimension was of little importance, but the classification and identification of ships could be related to the number of pixels within the area of the ship image and determined the required numbers as 1, 66 and 400 pixels at the image. These criteria correspond to the number of resels (resolution elements) per average ship dimension as a measure of visual discrimination.

O'Neill used a television system and experimented using a ship target 158 meters long and 14 meters high with an experienced observer. Subsequent research at the Naval Air Development Center showed that the number of resolvable elements characterizing a task is dependent upon the signal to noise ratio in the imagery. The less the noise the fewer the resolvable elements required.

There do not exist any criteria for visual discrimination that hold true for a wide spectrum of targets or conditions. So the best way for the determination of the appropriate criteria for a specific target, is to perform a simple psychophysical experiment. When no other information is available on which to establish a bar chart equivalent the data in Table 6 can be used as a first approach to determining the resolution criterion for the desired task

## **2. Critical Dimension and Target Aspect**

For the establishment of the bar chart equivalent of a specific task, the target critical dimension must be established. For this work the Moser "average target dimension", which is the square root of the target-projected area, will be used as the target critical dimension. This way of calculating the critical dimension was found by Moser to lead to consistent predictions even for very elongated targets.



Table 6 - Summary of target transform data [Ref.21].

<u>LAND TARGETS</u>				
RESOLVED LINE PAIRS (CYCLES) PER CRITICAL DIMENSION				
	<u>DET.</u>	<u>ORIENT.</u>	<u>RECOG.</u>	<u>IDENT.</u>
Truck	0.90	1.25	4.5	8.0
M-48 Tank	0.75	1.2	3.5	7.0
Stalin Tank	0.75	1.2	3.3	6.0
Centurion Tank	0.75	1.2	3.5	6.0
Half-Track	1.0	1.50	4.0	5.0
Jeep	1.2	1.50	4.5	5.5
Command Car	1.2	1.5	4.3	5.5
Soldier (Standing)	1.5	1.8	3.8	8.0
105 Howitzer	1.0	1.5	4.8	6.0
AVERAGE	$1.0 \pm 0.25$	$1.4 \pm 0.35$	$4.0 \pm 0.8$	$6.4 \pm 1.5$

<u>SHIP TARGETS</u>	
<u>O'NEILL DATA</u>	
<u>DISCRIMINATION TASK</u>	<u>RESOLVED LINE PAIRS (CYCLES) PER CRITICAL DIMENSION</u>
Detect Object on Horizon Sky	3
Recognize a Vessel	5
Recognize Ship Structure	11
Recognize Ship Type	16
Classify King Posts	16
Discern Radar Detail	33
Detect 40mm Gun Barrel	55

<u>MOSER DATA</u>	
<u>DISCRIMINATION TASK</u>	<u>RESOLVED LINE PAIRS (CYCLES) PER CRITICAL DIMENSION</u>
Detect a Ship	(Aperiodic treatment)
Classify Ship as Combatant	4
Recognize Ship Type	10

Since the critical dimension will be calculated as the square root of the exposed target area, the aspect of the target will play a major role. The target aspect affects the

apparent size and shape of the target. The area of the target image as a function of its dimensions and the azimuth and elevation aspect angles is given by:

$$A_T = l \times h \times \cos \theta \times \cos \varphi + w \times h \times \cos \theta \times \sin \varphi + l \times w \times \sin \theta \quad (4.6)$$

where:

$A_T$  = projected target area

$l$  = actual target length in meters

$w$  = actual target width in meters

$h$  = actual unobstructed target height in meters

$\theta$  = elevation angle

$\varphi$  = azimuth angle

The critical dimension of the target then will be:

$$D_c = \sqrt{A_T} \quad (4.7)$$

The orientation of the target for the calculation of the projected target area (with the dimensions of R/V POINT SUR) due to the viewing angle is displayed in Figure 15 along the lines of Shumaker [Ref. 21].

This approach was followed for the calculation of the projected area of R/V POINT SUR for this work. The calculation written in MATLAB is included in the program `mrt.m`, listed in Appendix H, to compute the MRT for the two scenarios.

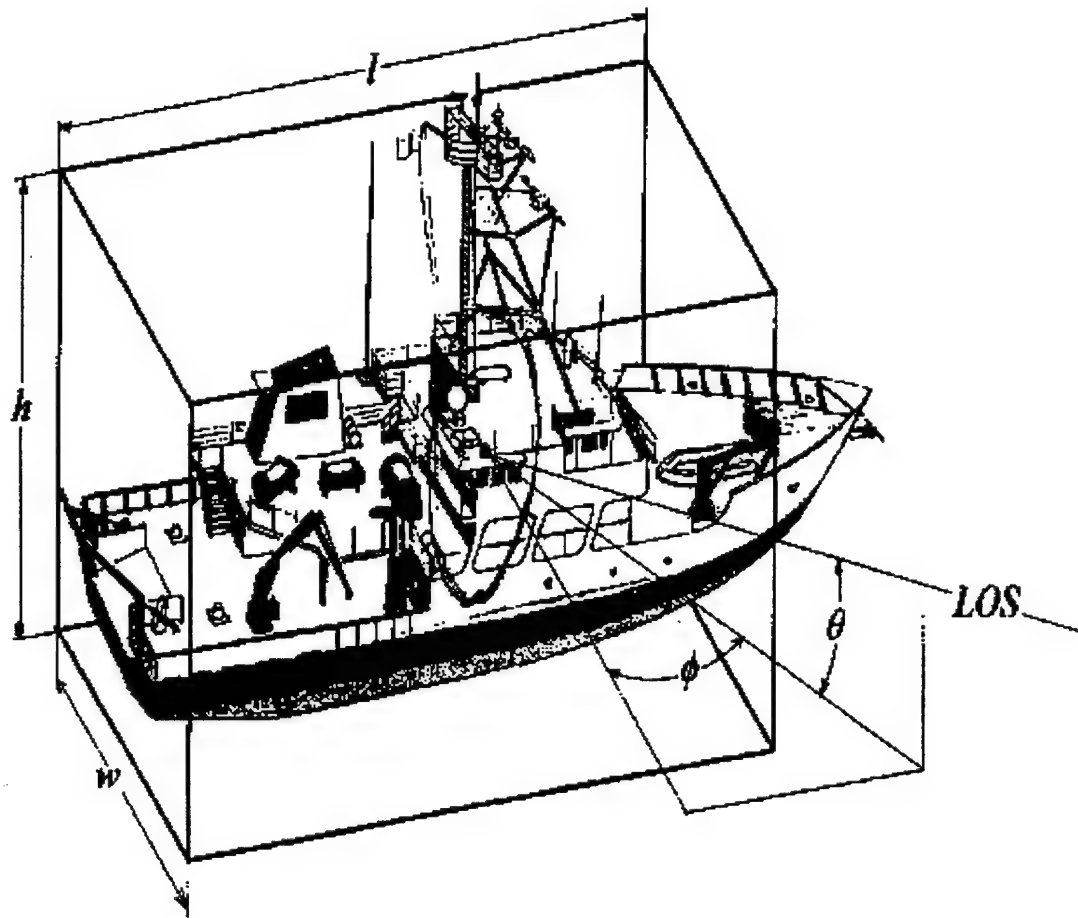


Figure 15 - Orientation of the R/V POINT SUR model.

#### D. MRT COMPUTATION AND CALCULATION VS RANGE WITH VARIOUS CRITERIA

Minimum Resolvable Temperature Difference (MRT) is the most used and most useful FLIR specification parameter. It gives the Temperature Difference  $\Delta T$  between hot and cold bars of a standard 4 bar (7:1 aspect ratio) chart required to make the bars just resolvable, as a function of the spatial frequency of the bars [Ref.21]. The object space spatial frequency  $f_x$  is the inverse of the target angular subtense and is usually measured in cycles per milliradian:

$$f_x = \frac{1}{1000} \left( \frac{R}{2d} \right) \quad (4.8)$$

where:

$f_x$  = spatial frequency in cycles per milliradian

$R$  = distance from the infrared system entrance aperture to the target

$2d$  = the spatial extent of one cycle = two times the bar width

The schematic representation of the above is displayed in Figure 16.

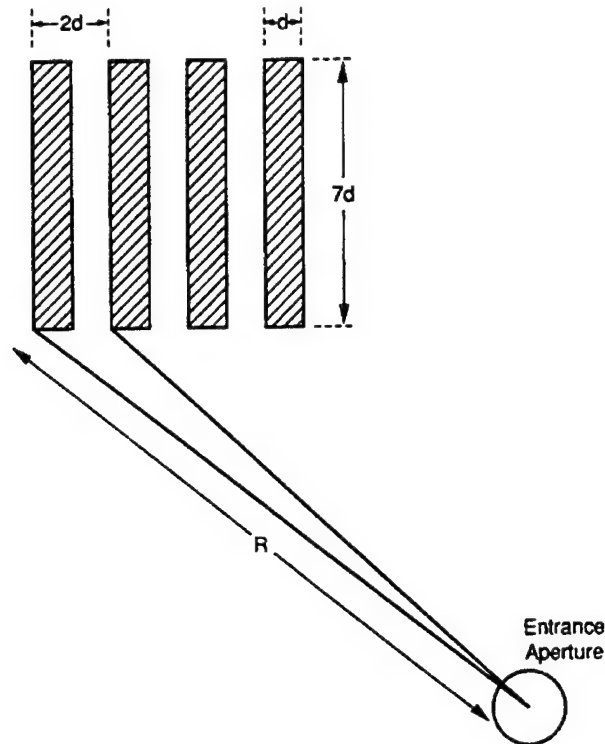
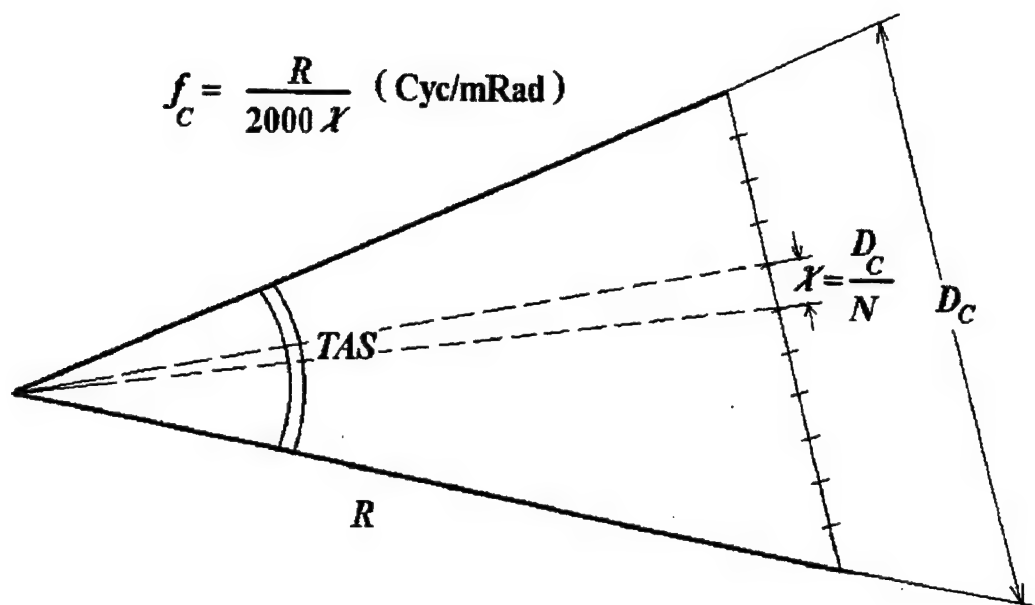


Figure 16 - Definition of spatial frequency. MRT targets have a 7:1 aspect ratio [Ref.2].

In order to plot the target spatial frequency as a function of range, which will be needed in the plotting of the MRT vs range, the fundamental spatial frequency characterizing the ship (basically twice its critical dimension) is expressed as a function of range according to Figure 17. This procedure is in accordance with that described in Shumaker [Ref.21]. In the case that the task is pure detection then  $N=1$ . Otherwise a value from the bar chart equivalent has to be taken.

For the calculation of the MRT a FLIR system with the characteristics displayed in Table 7 was assumed. The values displayed in Table 7 represent typical values for a generic Common Module FLIR.



- $N$  = Number of Bars in the Bar Chart
- $R$  = Slant Range
- $TAS$  = Target Angular Subtense
- $D_c$  = Critical Dimension
- $\lambda$  = Physical Dimension to be Resolved
- $f_c$  = Spatial Frequency of Bar

Figure 17 - Target spatial frequency vs range.

Some of these values were obtained from Shumaker [Ref.21], such as the Field of View values, the serial scan ratio, the over-scan ratio, the dwell time and the number of multiplexer samples per detector dwell time. Others were taken from the original data from the experiment, such as the target's dimensions. Some were chosen by assuming that these values would be close to a real sensor, since these values are not made publicly available by the companies that build FLIR systems. These values are the signal to noise ratio, the in and cross scan detector subtense, the aperture diameter, the focal length, the display spot size and the amplitude of residual image motion. Finally some of the

tabulated values are standard or were chosen in accordance to the specific detection criteria. These values are the number of bars in the bar chart, the specific detectivity, the average wavelength, the eye integration time and the length-to-width ratio of the bars in the bar chart.

From these parameters the MRT and NET were computed using Equations 4.3 and 4.4, and expressed as functions of target range, using Equation 4.8 and the procedure of Figure 17, for the values of N appropriate to detection (N=2) recognition (N=8) and identification (N=13) using the Johnson Criteria. The dimensions of R/V POINT SUR were used for the calculation of the target characteristics.

With the assistance of a series of IDL programs the ship's hot spot temperature along with the sea surface temperature was obtained from the data of the experiment.

With the known hot spot ship temperature (300.26 K, the average of thermistors 11 and 16) and sea temperature (289.95 K, sea surface temperature), the zero range Temperature Difference ( $\Delta T_o = T_{tgt} - T_{bckgd}$ ) was converted using Planck's Law (with the rad.m program) into a Target-Background Radiance Difference with horizontal polarizer ( $\Delta L_h$ ) and with no polarizer ( $\Delta L_o$ ). These radiance differences were propagated to arbitrary range using SEARAD to provide the polarized sea surface radiance and the path attenuation and path radiance for both the horizontally polarized and unpolarized cases. Reconverted to temperature difference these are tabulated in an EXCEL spread sheet (an example of one of spreadsheets used is in Appendix J). A schematic representation of the procedure is displayed in Figure 18.

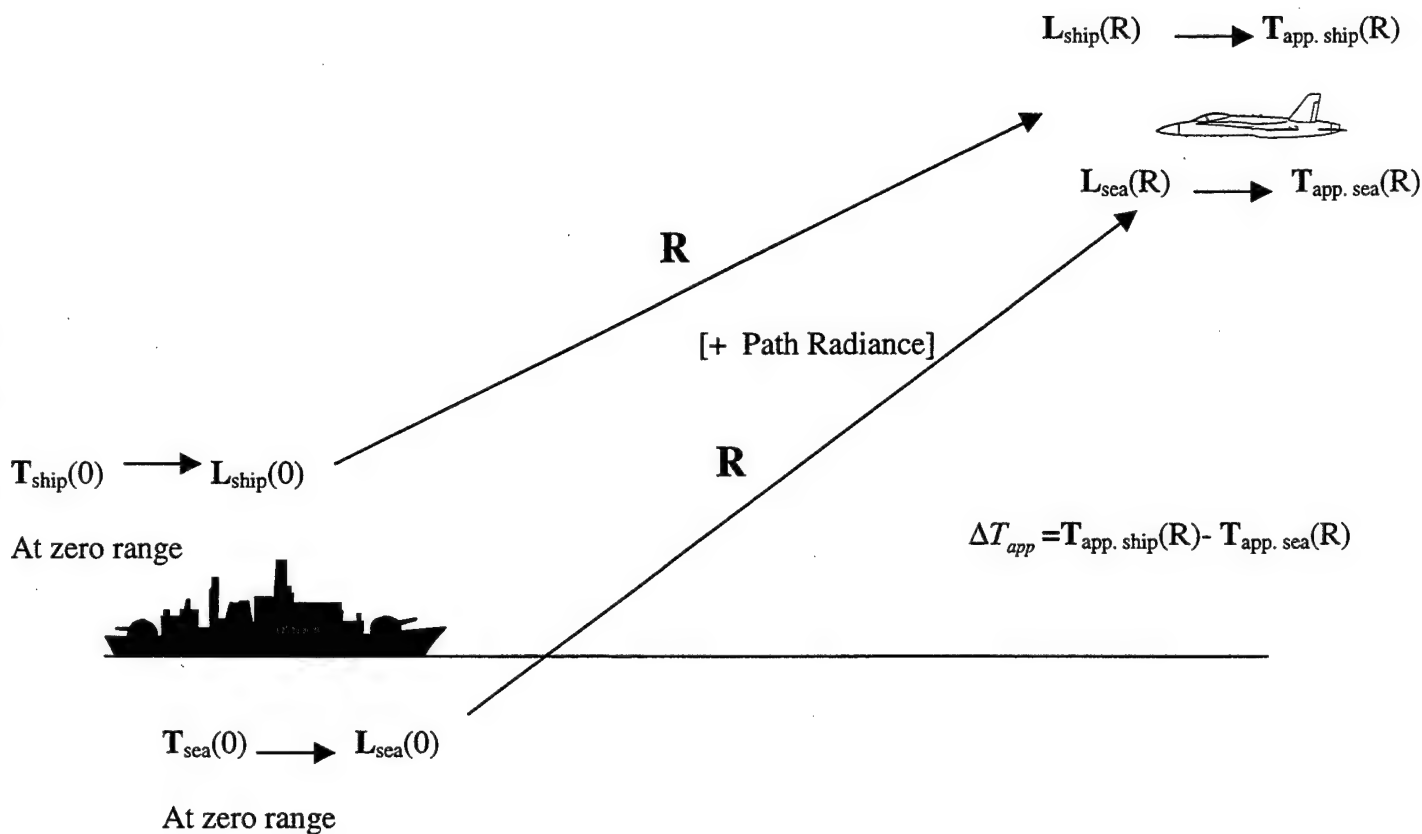


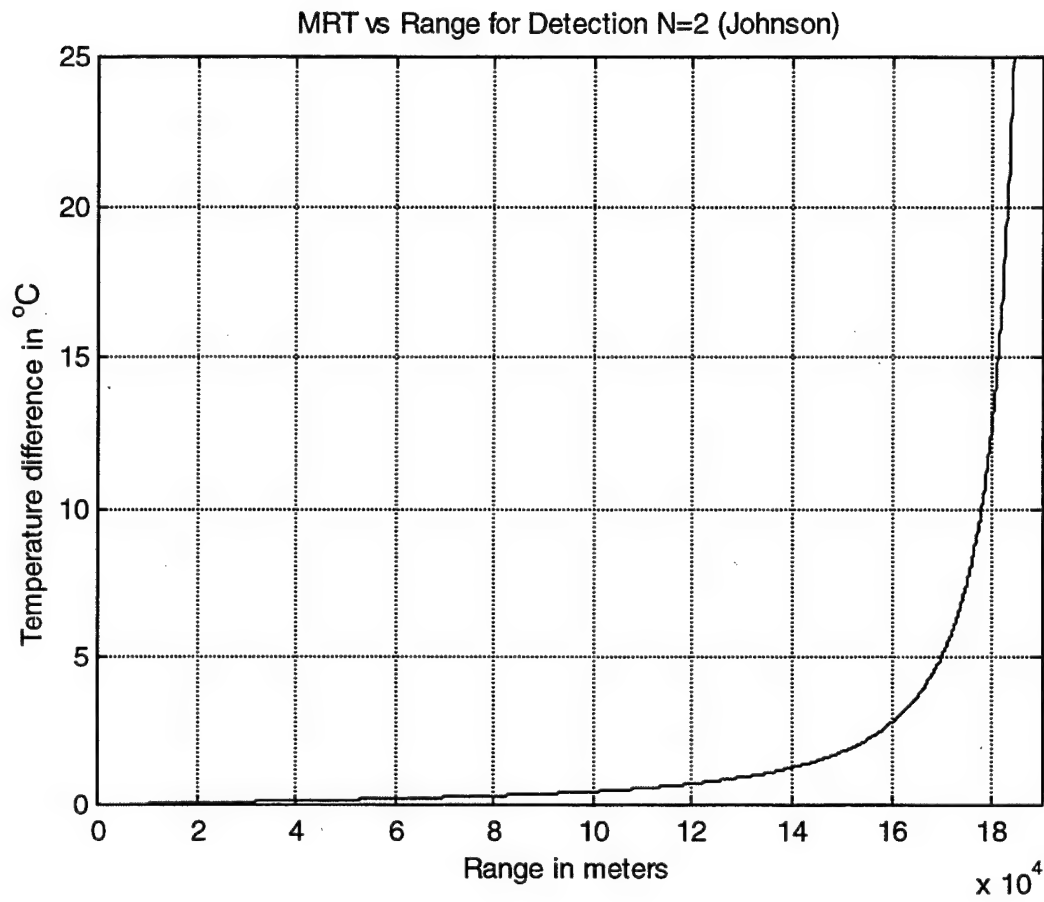
Figure 18 - Schematic representation of the procedure followed to derive the Apparent Temperature Difference  $\Delta T_{app}$

With these characteristics of the system and the target and by taking into consideration the target aspect, a series of MRT curves were plotted with the assistance of the mrt.m program listed in Appendix H. The following plots were calculated for a height of the observer (sensor) of 1000m. N is the number of bars in the bar chart that in this case is also the number of resolution elements (resels, defined as "the smallest region in the object space whose dimension is equal to the resolution in that dimension" [Ref.12]) required on the target dimensions.



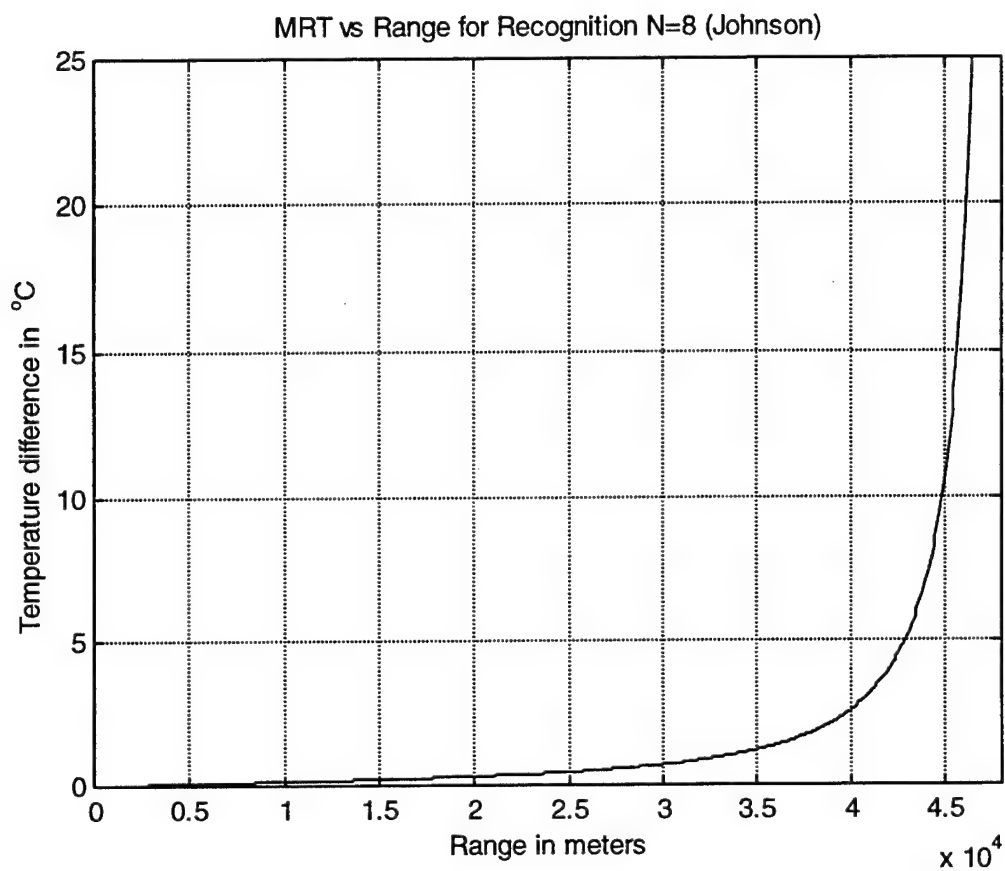
Table 7 - FLIR system and target characteristics.

Symbol	Value	Definition
FOV <sub>x</sub>	6.86 degrees	Field of View in the x direction
FOV <sub>y</sub>	5.16 degrees	Field of View in the y direction
SNRT	2.5	Signal to noise ratio
dx	0.1	In-scan detector subtense in mrad
dy	0.1	Cross-scan detector subtense in mrad
L	7	Length-to-width ratio of the bar 7:1
t <sub>e</sub>	0.1	Eye integration time in seconds
N <sub>ss</sub>	1	Serial scan ratio
N <sub>os</sub>	1	Over-scan ratio
Fr	30	Frame rate in Hz
D	0.1	Aperture diameter in meters
$\lambda$	$10 \cdot 10^{-6}$	Approximation of the radiation wavelength
l	41.5	Length of the ship in meters
w	9.75	Width of the ship in meters
h	8.8	Height of the ship in meters
t <sub>d</sub>	$6 \cdot 10^{-5}$	Dwell time in seconds
f <sup>*</sup>	$30 \cdot 10^3$	Frequency at which the response is down 3db from its low frequency response
Df <sub>p</sub>	$8.5 \cdot 10^6$	Half power frequency response of the preamplifier in HZ
Ns	2	Number of multiplexer samples per detector dwell time
HD	0.2	Height of the display in meters
d <sub>ss</sub>	$3.43 \cdot 10^{-4}$	Display spot size in meters
Dv	0.5	Display viewing distance in meters
AR	0.015	Amplitude of residual image motion in mrad
to	0.7	Transmission of the optics
Nd	180	Number of detectors
N <sub>sc</sub>	0.75	Scan efficiency
D <sub>s</sub>	$4 \cdot 10^{10}$	Specific detectivity in [cm Hz <sup>1/2</sup> W <sup>-1</sup> ]
f	0.2	Focal length in meters
N	Depends on the criteria	Number of bars in the bar chart



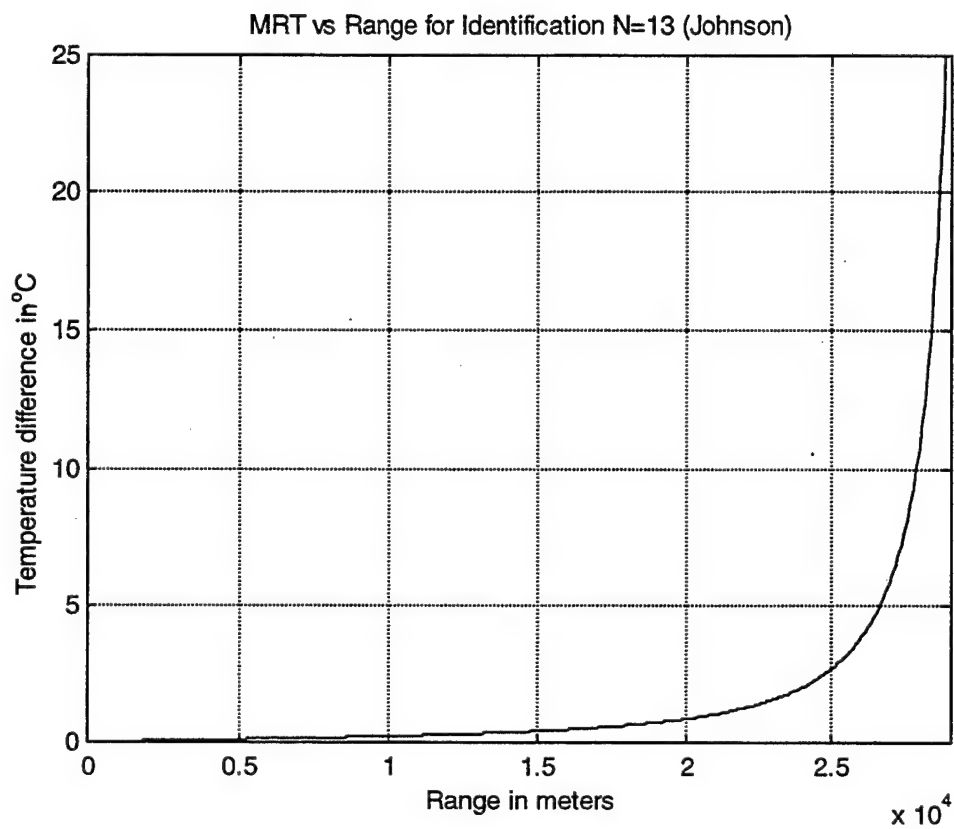
N= required number of resels on critical dimension for detection

Figure 19 - MRT vs Range for Detection N=2 (Johnson).



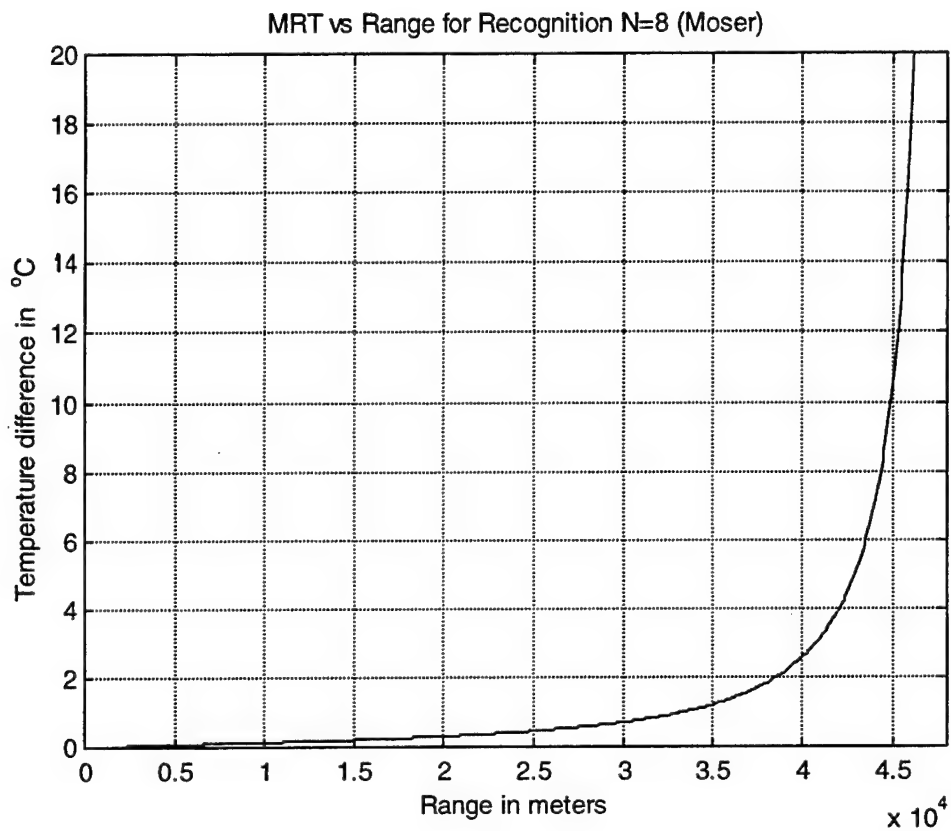
N= required number of resels on critical dimension for recognition

Figure 20 - MRT vs Range for Recognition N=8 (Johnson).



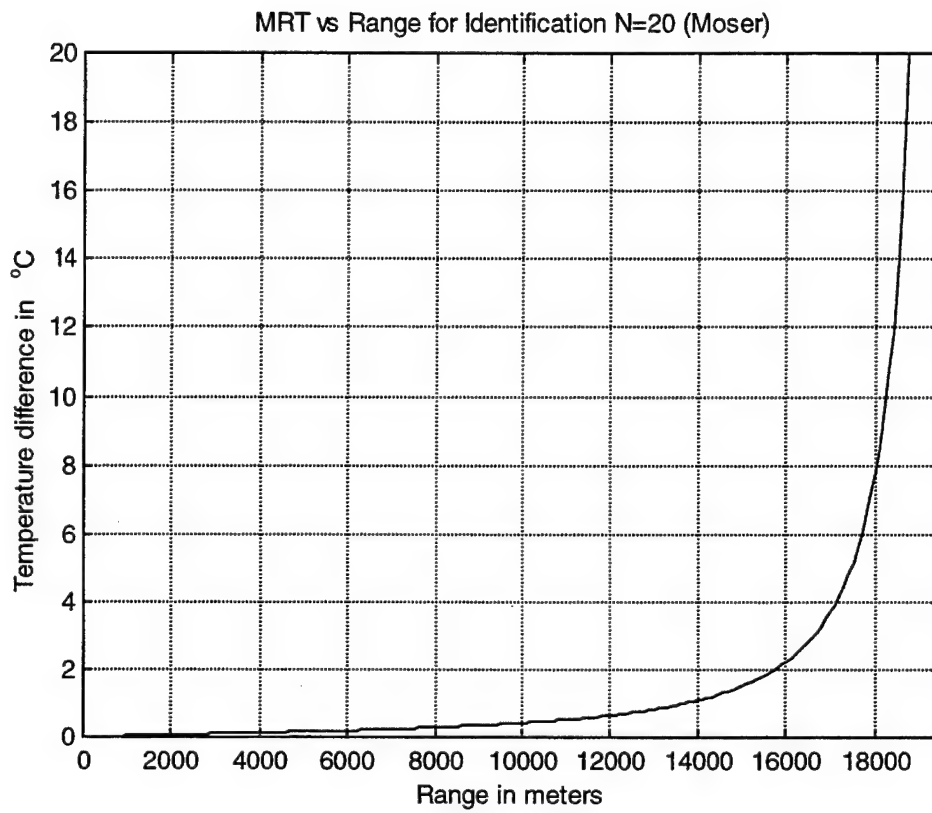
N= required number of resels on critical dimension for identification

Figure 21 - MRT vs Range for Identification N=13 (Johnson).



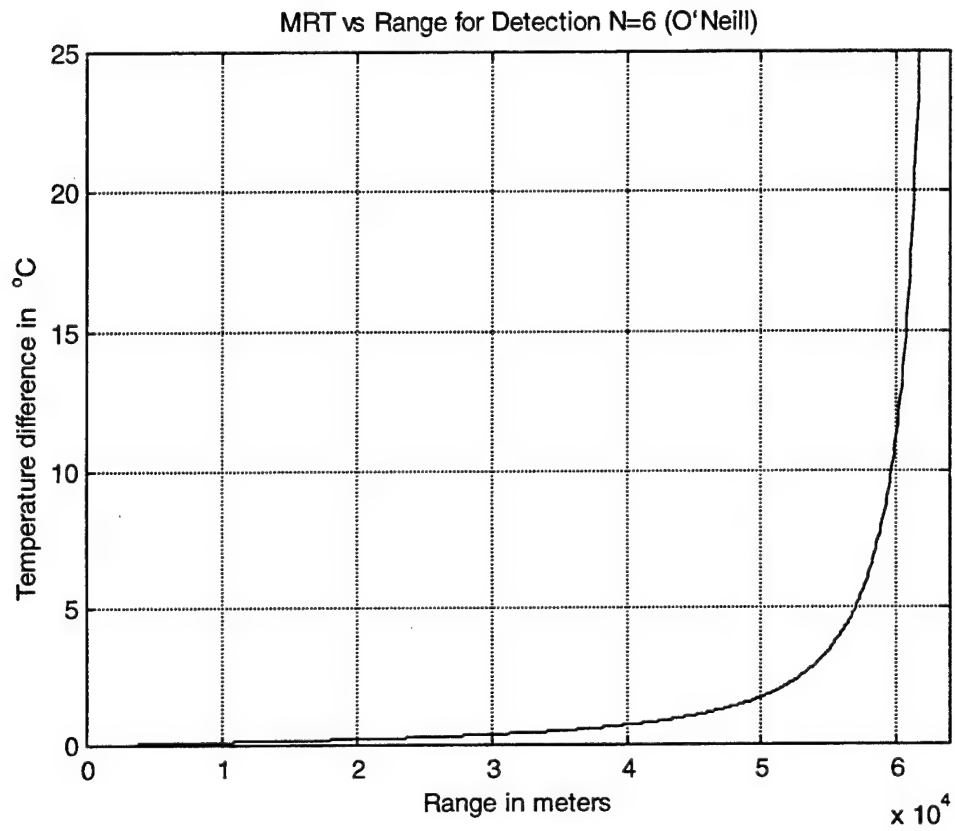
N= required number of resels on critical dimension for recognition

Figure 22 - MRT vs Range for Recognition N=8 (Moser).



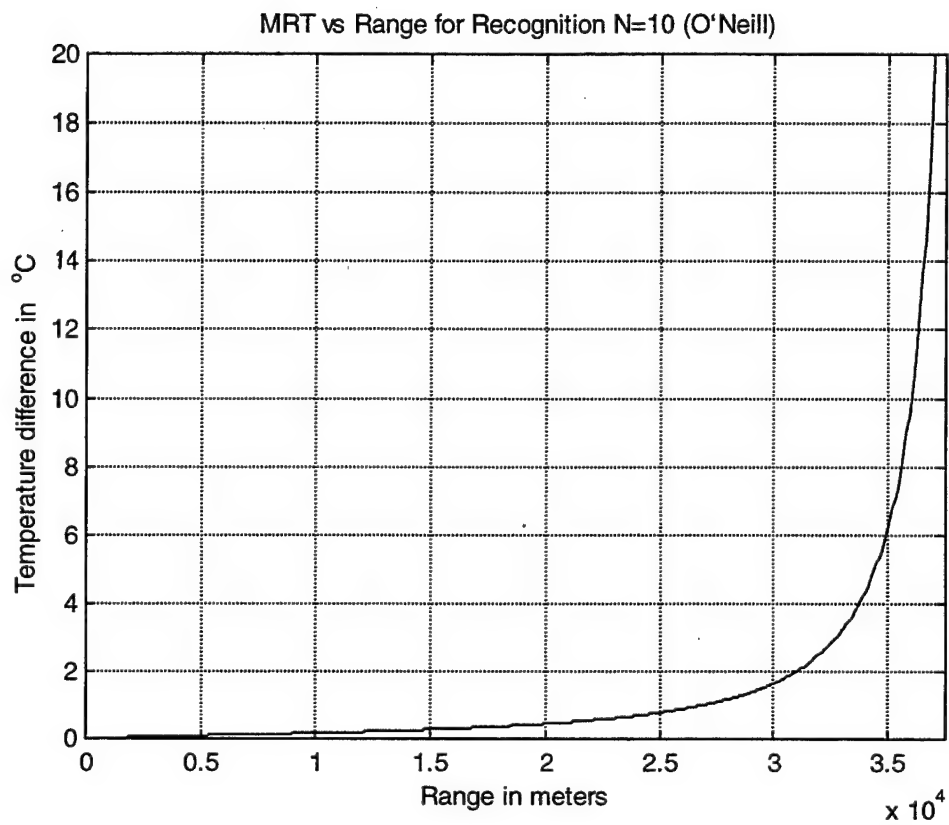
N= required number of resels on critical dimension for identification

Figure 23 - MRT vs Range for Identification N=20 (Moser).



N= required number of resels on critical dimension for detection

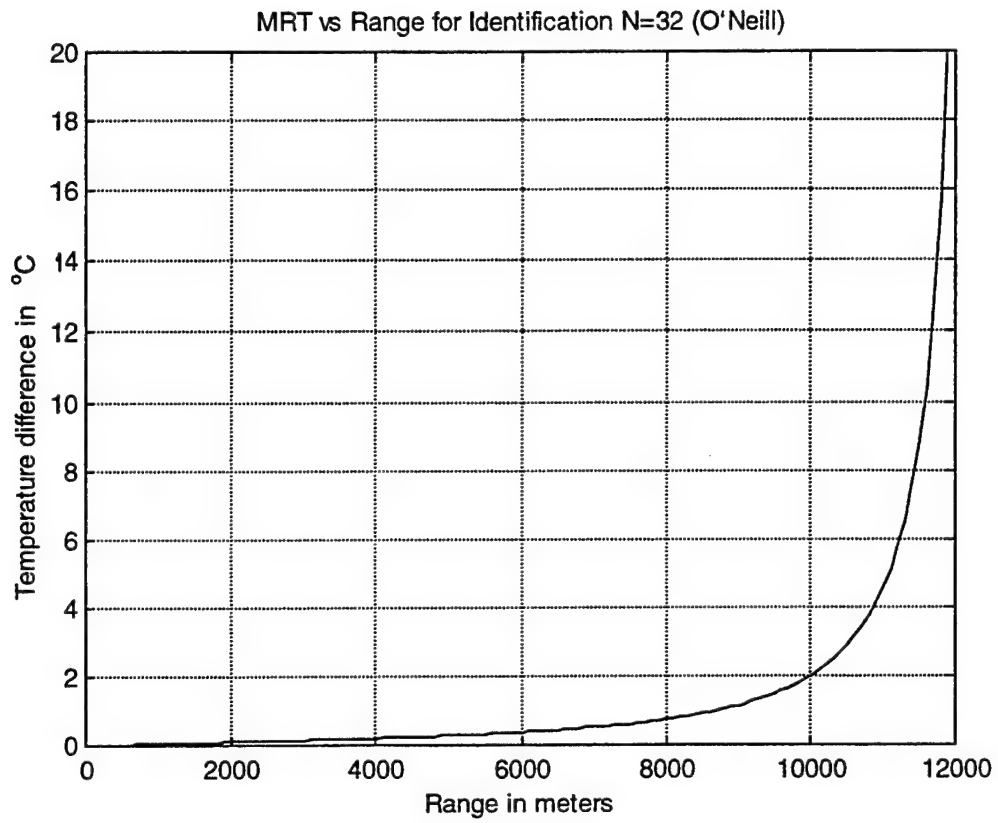
Figure 24 - MRT vs Range for Detection N=6 (O'Neill).



N= required number of resels on critical dimension for recognition

Figure 25 - MRT vs Range for Recognition N=10 (O'Neill).





N= required number of resels on critical dimension for identification

Figure 26 - MRT vs Range for Identification N=32 (O'Neill).

## V. RESULTS

After the procedures described in the previous chapters, the sea surface radiance for the conditions of the image was calculated using SEARAD in radiance mode for various positions of the FLIR with respect to the target, for both scenarios. The radiance values and the MRT values were tabulated and plotted using the EXCEL spreadsheet program. The plots for the 100 m and the 1000 m sensor elevations are displayed in Figure 27 and Figure 28 respectively.

These figures show the Apparent Target to Background Temperature Difference,  $\Delta T_{app}$ , with no polarizer compared with that for horizontal polarizer, plotted against slant range for the sensor at each of the selected fixed elevations, 100 m and 1000 m. This represents the available temperature difference at the receiver as a function of range,  $R$ , from the source. The Minimum Resolvable Temperature Difference, MRT, is shown on the same scale for the same conditions. The intersection of the available  $\Delta T$  with the MRT defines the maximum range at which the task can be performed. In Figure 27 the MRT for identification is shown for sensor at 100m height. The range at which this MRT crosses the Apparent Temperature Difference curve defines the maximum range for identification. Figure 28 shows the equivalent information for sensor at 1000m height.

For the 100m case and for  $N=12$  (six line pairs, which is the identification case for the Johnson criteria), the apparent temperature difference for the horizontally polarized case crosses the MRT line at a range of 13 km. For the same conditions but the unpolarized case the two lines cross at a range of about 28 km.

For the 1000m case and for  $N=12$  respectively, the apparent temperature difference for the horizontally polarized case crosses the MRT line at a range of 18.5 km.

For the same conditions but the unpolarized case the two lines meet at a range of about 29 km.

The inference that may be drawn from these two figures is that the use of the horizontal polarizing filter decreases the maximum range for identification, although the short-range radiance or temperature contrast is improved by the filter. This loss of identification range follows from the fact that the plotted curves of  $\Delta T_{app}$  cross at a relatively short range, and beyond this “cross-over range” identification range is reduced by the presence of the filter. This conclusion should be stated with caution pending a more detailed and complete study. It should be remembered that no consideration is given to reflected sky radiation or sun glint in the ship signature, with or without polarization. The possibility of error in the magnitude of the ship signature should be kept in mind, which could cause error in the apparent temperature difference, and hence in the cross over point.

Two anomalies appear in the curves of Figures 27 and 28, namely;

- a) From the plots of Figures 27 and 28 it is also observed that at some distance beyond the crossover range the temperature difference passes through zero and goes negative for the horizontally polarized case

- b) In Figure 28 both the unpolarized and the polarized signatures exhibit an apparent upward displacement or "bump" in the range around 6 to 10 km.

At first glance there is no physical explanation to this behavior, which appears to be inherent in the model used.

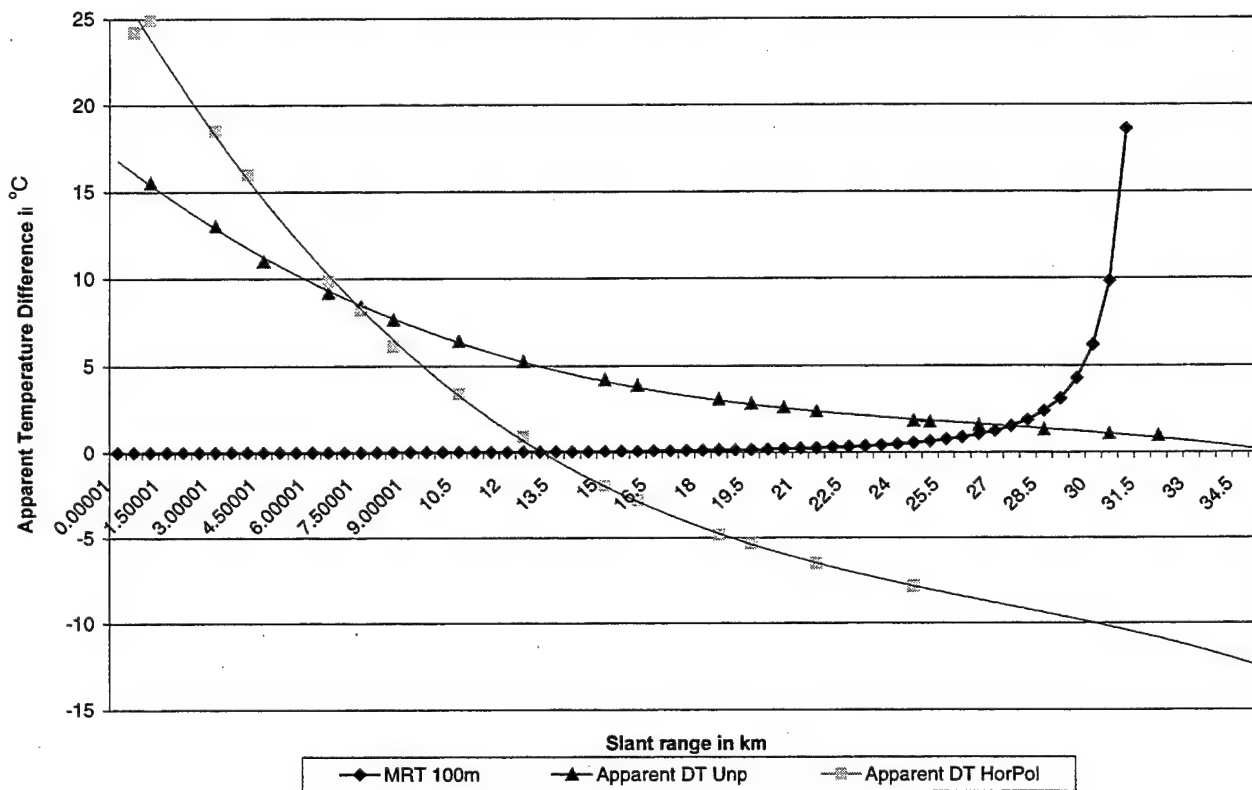
Since at greater ranges the received radiance is known to be dominated by the path radiance which is common to both source and background signatures, the apparent temperatures of the target and background should approach each other asymptotically, so that the apparent temperature difference should approach zero. The unpolarized apparent temperature difference shows this expected behavior in both scenarios, but in both cases the horizontally polarized case shows this anomaly. This suggests that the model used is inadequate in some way to describe the real behavior. Operationally, the anomaly could be made to disappear by adding an offset of about  $11^{\circ}\text{C}$  to the Horizontally Polarized  $\Delta T$  curve in Figure 27, and a similar offset to Figure 28. This correction is displayed in Figure 30, where the temperature is forced to zero at 36 km. While the physical mechanism of such an offset has not yet been identified, several hypotheses have been considered. Additionally, an unexpectedly low value of unpolarized temperature difference occurs at very short ranges in the 1000m scenario only.

The negative temperature difference might perhaps be explained by considering the different spectral distributions of the target and the background, compared with the spectral distribution of transmittance. This point is further discussed in Chapter VI, Discussion and Conclusions. The polarizers for the wavelengths of interest have

relatively uniform properties over the band used, so it does not seem that they should affect adversely the spectral distribution of the target and the background.

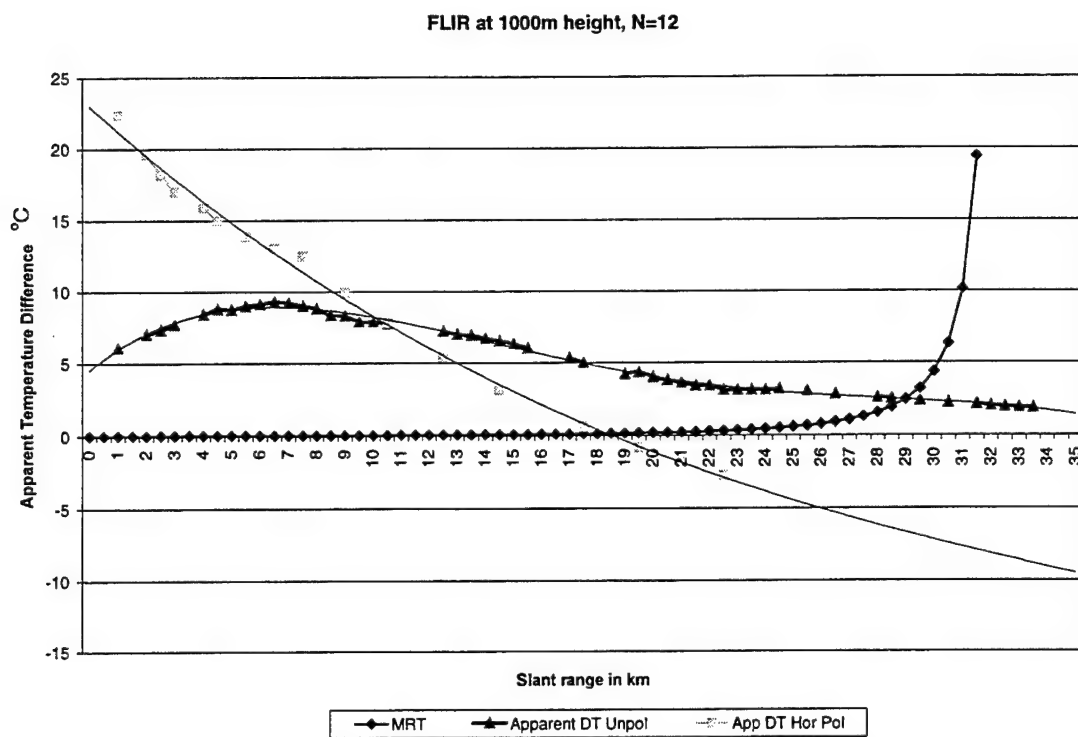
The increase (bump) in the apparent temperature difference curve, noted profoundly in the unpolarized case for sensor at 1000m at ranges up to 8 km is of interest. This behavior was also noted in Chih-Li Yu [Ref. 27]. It may have a connection with the modeling of the waves and the geometry of the simulation (including Sun direction), but for valid conclusions a more thorough study is necessary. This is also considered under discussion in the next chapter.

FLIR at 100m height, N=12



N= required number of resels on critical dimension for identification

Figure 27 - MRT, unpolarized and horizontally polarized apparent temperature difference for sensor at 100 meters.



N= required number of resels on critical dimension for identification

Figure 28 - MRT, unpolarized and horizontally polarized apparent temperature difference for sensor at 1000 meters.

# Sensor at 1000m height Unpolarized

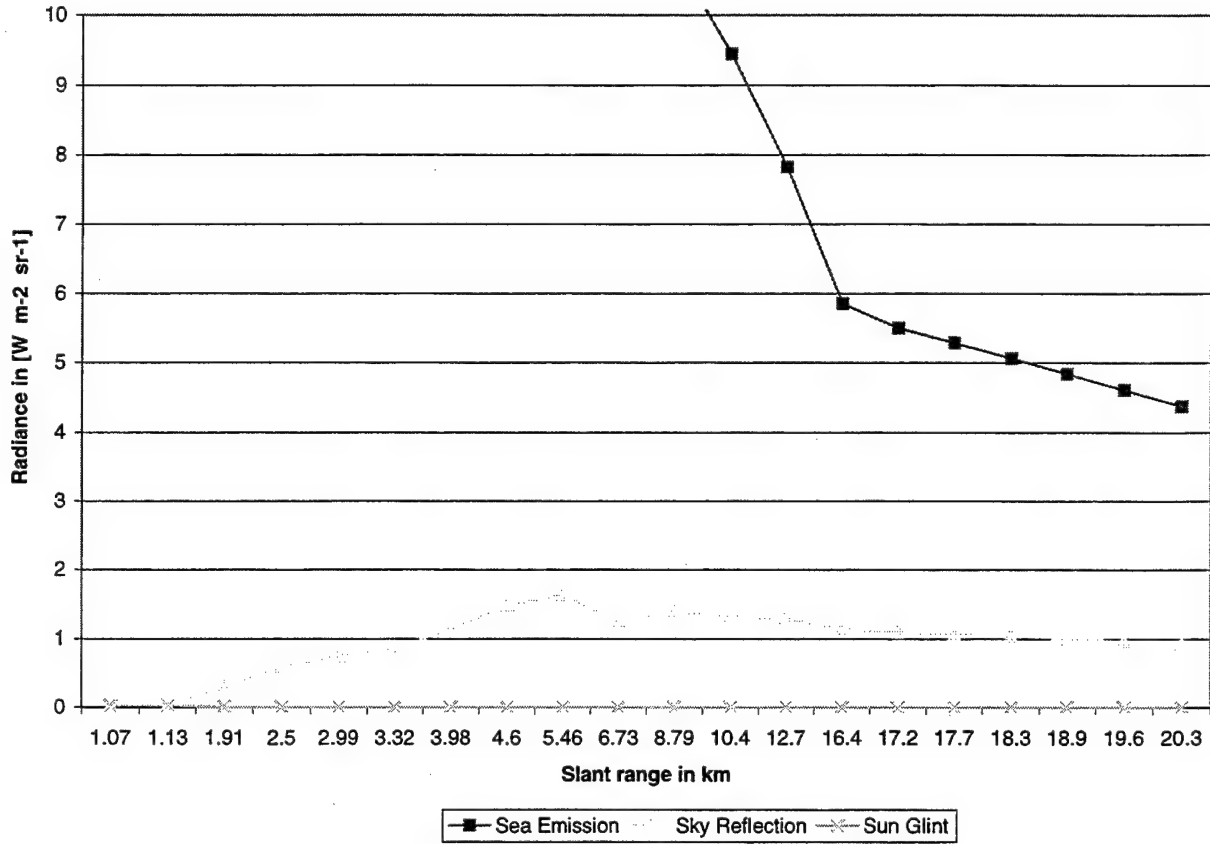


Figure 29 - Plot of full range (slant ranges) horizontally polarized values from SEARAD for Sea Emission, Sky Reflection and Sun Glint for sensor at 1000 meters height.



# FLIR at 100m height, N=12

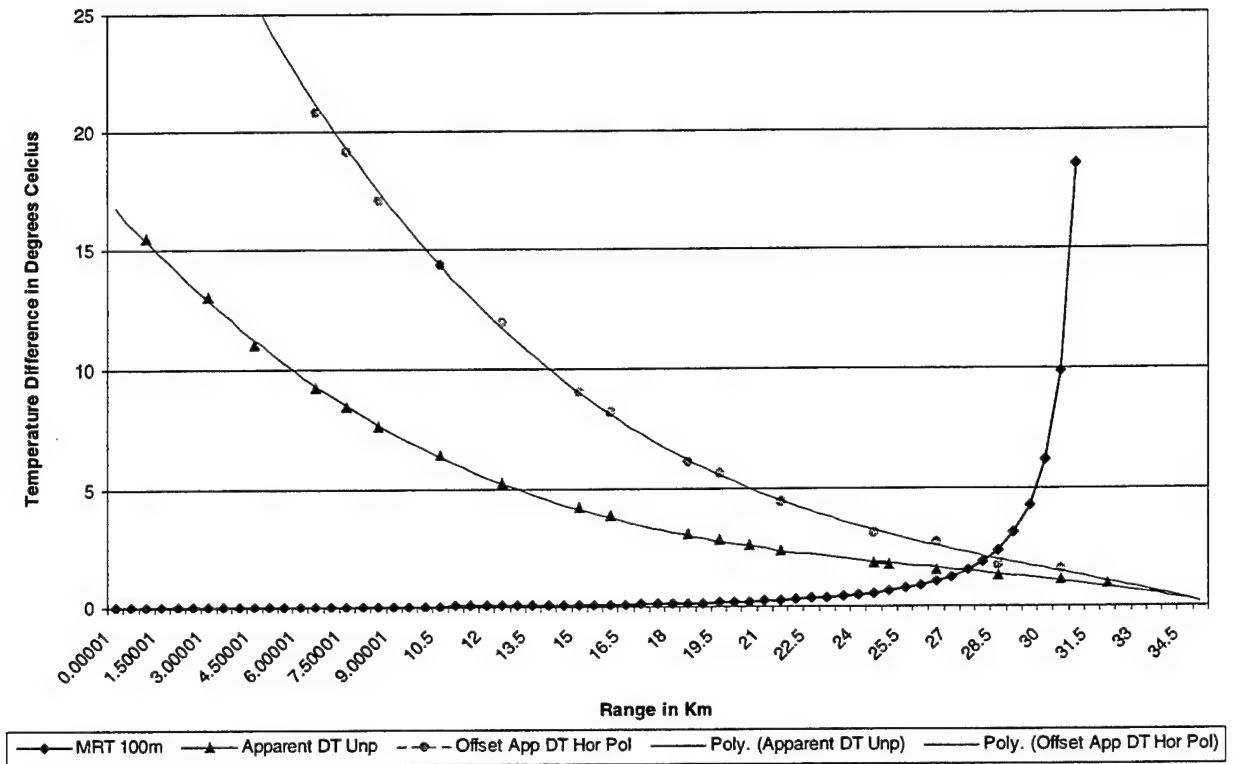


Figure 30 – Plot of MRT, unpolarized and horizontally polarized apparent temperature difference for sensor at 100 meters, with an offset of 11 degrees Celsius to the horizontally polarized apparent temperature difference.

## VI. CONCLUSIONS AND DISCUSSION

From the plots in Figures 27 and 28 the polarized case gives a significantly bigger Apparent Temperature Difference at close ranges whereas the unpolarized case seems to give higher Temperature Differences at greater ranges. So there appears to be a considerable increase in the Apparent Temperature Difference by using a horizontally polarized filter for ranges up to about 10 km. From the outputs of this work there are some very interesting observations which require interpretation.

The first is the fact that the Apparent Temperature Difference for the polarized case passes through zero and goes negative after a certain range. At this time there is no physical explanation for this phenomenon. The temperature differences would be expected to approach zero as the separate radiances become dominated by the path radiance at long range. A possible cause of this anomaly might be differences in the spectral characteristics of the target and background, since the SEARAD transmittances used for determination of apparent target temperature are averages across the in-band wavelengths of interest (8-12  $\mu m$  in this case). Thus the gray body distribution that was used for target and background at different temperatures might have caused suppression (due to averaging) of strong emission or absorption sub-bands within the 8-12  $\mu m$  band. With a spectral analysis of the target and background perhaps the different spectral characteristics might indicate sub-bands of prominent target or background emission bands, as are known to be existent in the 3-5  $\mu m$  band already. If the different spectral characteristics of target and background were found to be true, it could lead to significant target detection advantages, by exploiting the spectral characteristics of specific targets.

In the scenario studied this could lead to preferential propagation of either source or background radiance over the other.

In a first approach to this issue, a plot of the transmittance by sub-band of the 8-12  $\mu\text{m}$  band was made using SeaRad. An obvious variation in the transmittances can be seen from Figure 31. This fact has an important effect on the final apparent temperature difference, since the poor transmittance in one part of the sub-band affects negatively the total transmittance of the whole band. The hypothesis is presented that the integral over the bandwidth of spectral radiance multiplied by spectral transmittance may differ from the product of the integrated in-band radiance times the average transmittance. This could possibly also help provide an interpretation of the related issue, that the two Apparent Temperature Difference curves for the horizontally polarized and the unpolarized cases cross each other. A further effort to evaluate this hypothesis was made by computing separately the product of radiance and transmittance by sub-band. This was done separately for the source temperatures of the sea and the target, with the results shown in Appendix K. The conclusion drawn from this analysis is that the blackbody spectral distributions for the temperatures of target and background differ somewhat in magnitude but negligibly in shape. The correctly sub-band-integrated transmittance at range 25-km showed no difference to four significant figures between the two source temperatures. However this analysis did not take account of reflected sky radiance in the ship signature, while this is a significant part of the background signature. This omission, required by the level of target modeling, implies an under-estimate of the apparent temperature difference. Target size and shape effects are not included in this model. Representation

of the ship target by its hot spot temperature is also somewhat unrealistic, since the sensor Detector Angular Subtense of one (1) mrad gives a footprint of 25 meters at 25 km, which greatly exceeds the hot spot width. The conversion of source temperature to and from radiance should be checked further for consistency.

The "bump" in the Apparent Temperature Difference curve in Figures 27 and 28 at ranges up to 8 km approximately is a second anomaly. This behavior was also noted in Chih-Li Yu [Ref.27]. In these ranges the zenith angle is relatively small, approaching the vertical. In Figure 29 the separated plots of the full range (slant ranges) horizontally polarized values from SEARAD for Sea Emission, Sky Reflection and Sun Glint for sensor at 1000 meters height reveal that the Sky Reflection parameter introduces a small bump at these ranges. It is also known from Wolfe and Zissis [Ref.26] that there is a variation in the spectral radiance of the sky at different angles of elevation. These facts along with the wave geometry could be the main contributing reason for this phenomenon. These are the first thoughts about this and more study is needed to derive more complete conclusions.

Conclusions as to the relative values of identification range for polarized and unpolarized cases should be treated as tentative pending further analysis and improvement of the model.

8-12 microns for FLIR at 100m height and 24.5 Km range

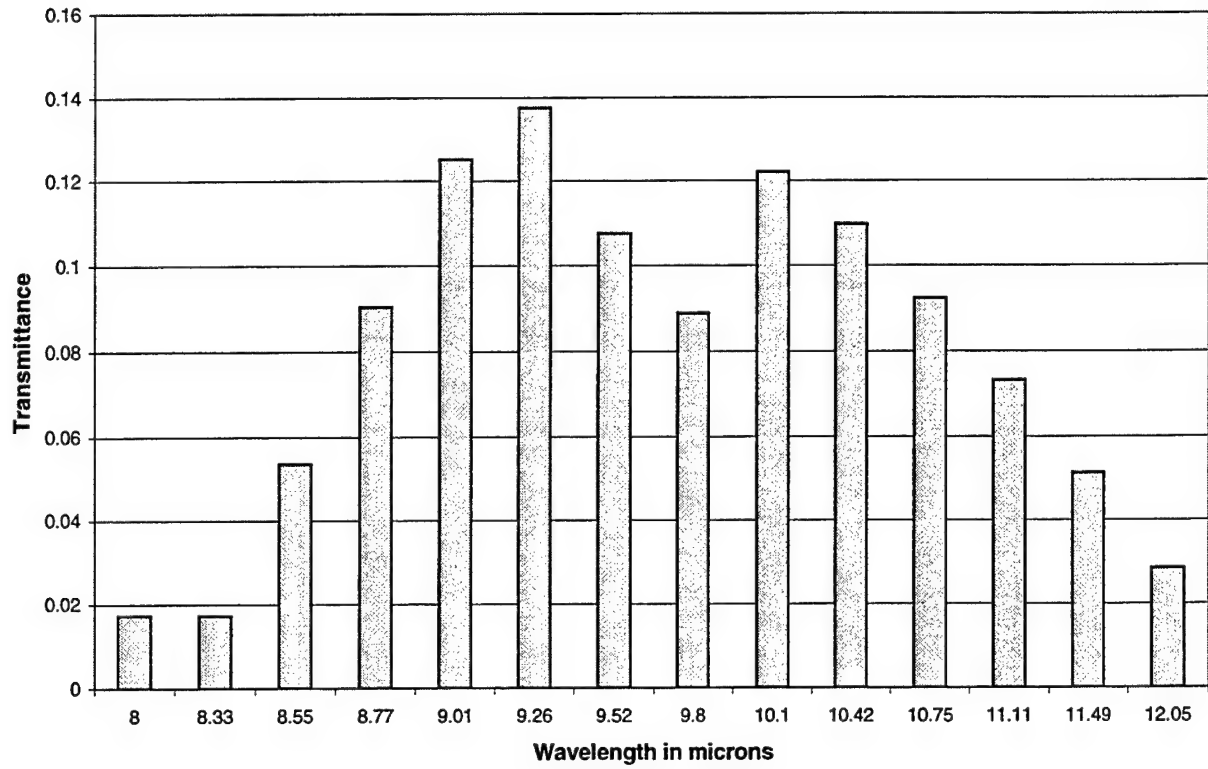


Figure 31 - Transmittances in relation to the sub-band wavelength.

## VII. RECOMMENDATIONS FOR FUTURE WORK

One observation of interest in this work is the negative apparent temperature difference of the horizontally polarized case after a certain range. Due to the lack of any physical explanation of the phenomenon at this time some new ideas about the target and background characteristics were considered. One such explanation deriving from the 3-5  $\mu m$  band relates with the different spectral properties of target and background.

The target and background behave in a different way spectrally. In this experiment SeaRad calculated average values for the wavelengths of interest (8-12.05  $\mu m$ ). In this way a wavelength region of low transmittance of the target could effect adversely the infrared characteristics of the target. Analyzing that in the spectral domain and examining the properties of target and background spectrally could provide characteristic patterns that would eventually improve discrimination of the target from the background.

It is realized that the standard formulation of the MRT is based on a 300° K background. Since the background temperature varies and is only sometimes that the specific 300° K matches for the real conditions, a further study of the MRT formulation is needed in order to examine the accuracy of the calculations in other cases than the 300° K background.

The algorithm used for conversion of source temperature to radiance, and its inversion to return to apparent temperature should be evaluated and validated, particularly as applied to partially polarized radiation.



## **APPENDIX A**

### **EXPERIMENT LOCATION**

#### **Description :**

Plots of the GPS information of the ship trajectory during the experiment in April 9 and April 10, 1996. Image set recording points are marked as diamonds in this figure.

Map showing the planned ship positioning and desired ship heading in each station location.

#### **Conditions :**

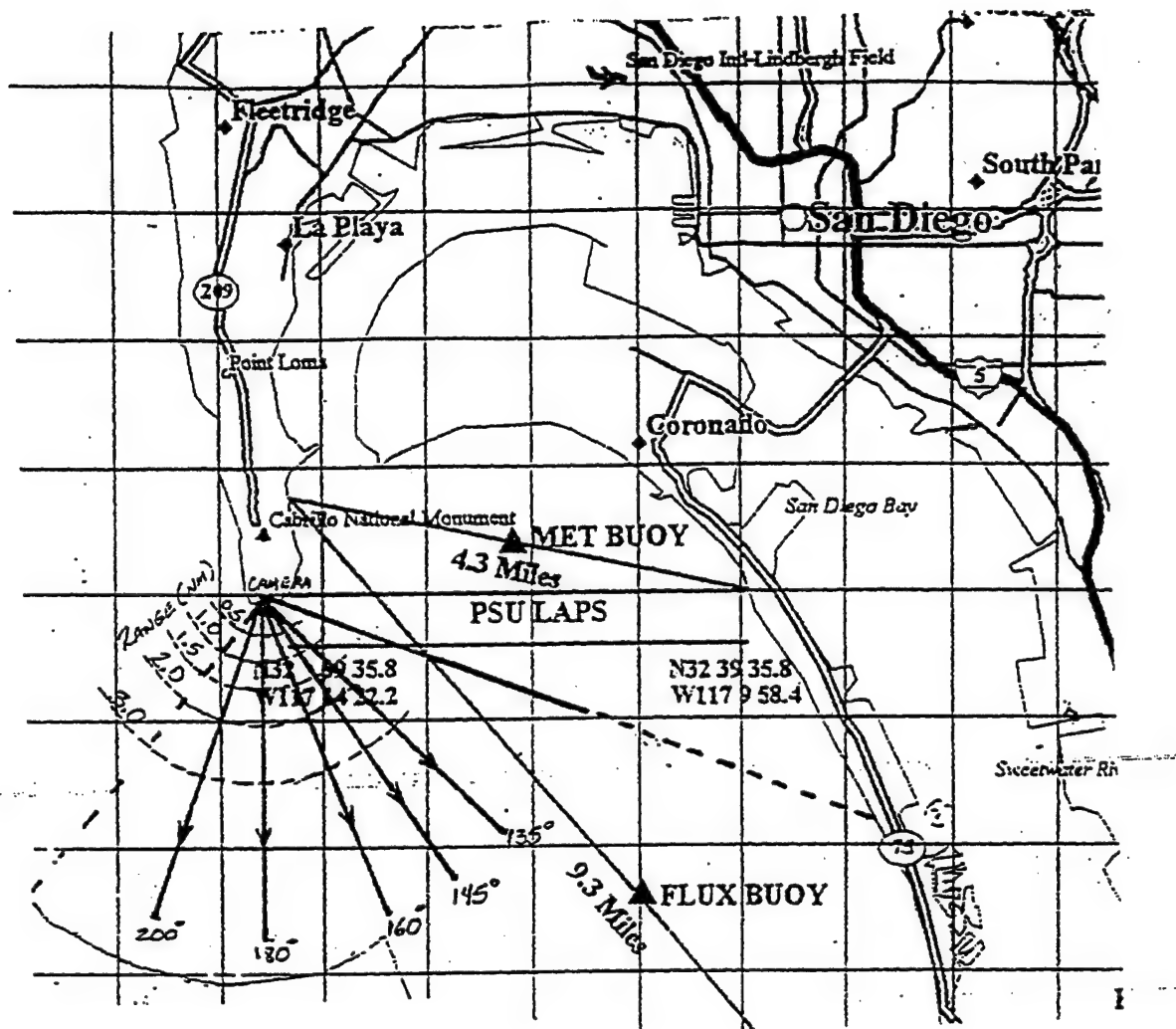
The AGA-780 Thermovision was located at the Building 15 of the NCCOSC-NRaD in Point Loma. Its geographic coordinates were N 32 39 35.8, W 117 14 22.2. It was mounted on a table projecting from the window, and directed using a remote pan-tilt head. The ship maneuvered in reference to the camera position according to five planned magnetic bearings (camera to ship) ranging from 135 to 200 degrees. For each bearing there are 5 station locations at ranges from 0.5 to 3.0 nm. In each station location the ship is supposed to turn to the indicated magnetic headings and stay still during the time needed for the image recording process. This process was modified by ship-handling necessities.



**Notes :**

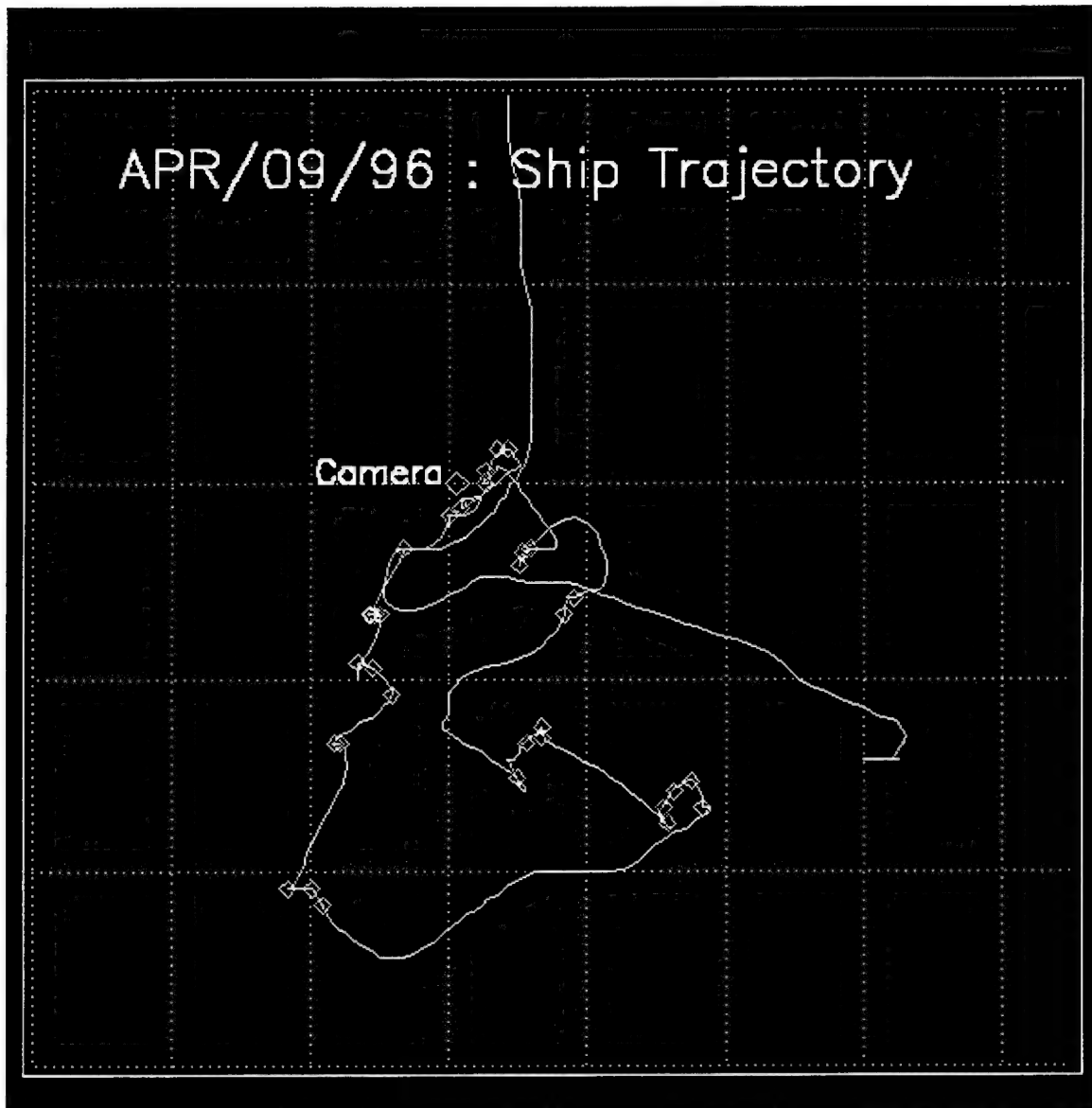
Both ship GPS position and camera location are known, so bearing is computed. Thus, ship heading information is used with the bearing information to give the aspect angle of the target.

Range to the shore station and ship heading were reported from the ship at irregular intervals and recorded at the sensor. Magnetic bearings to the ship were recorded on land in the sensor log.

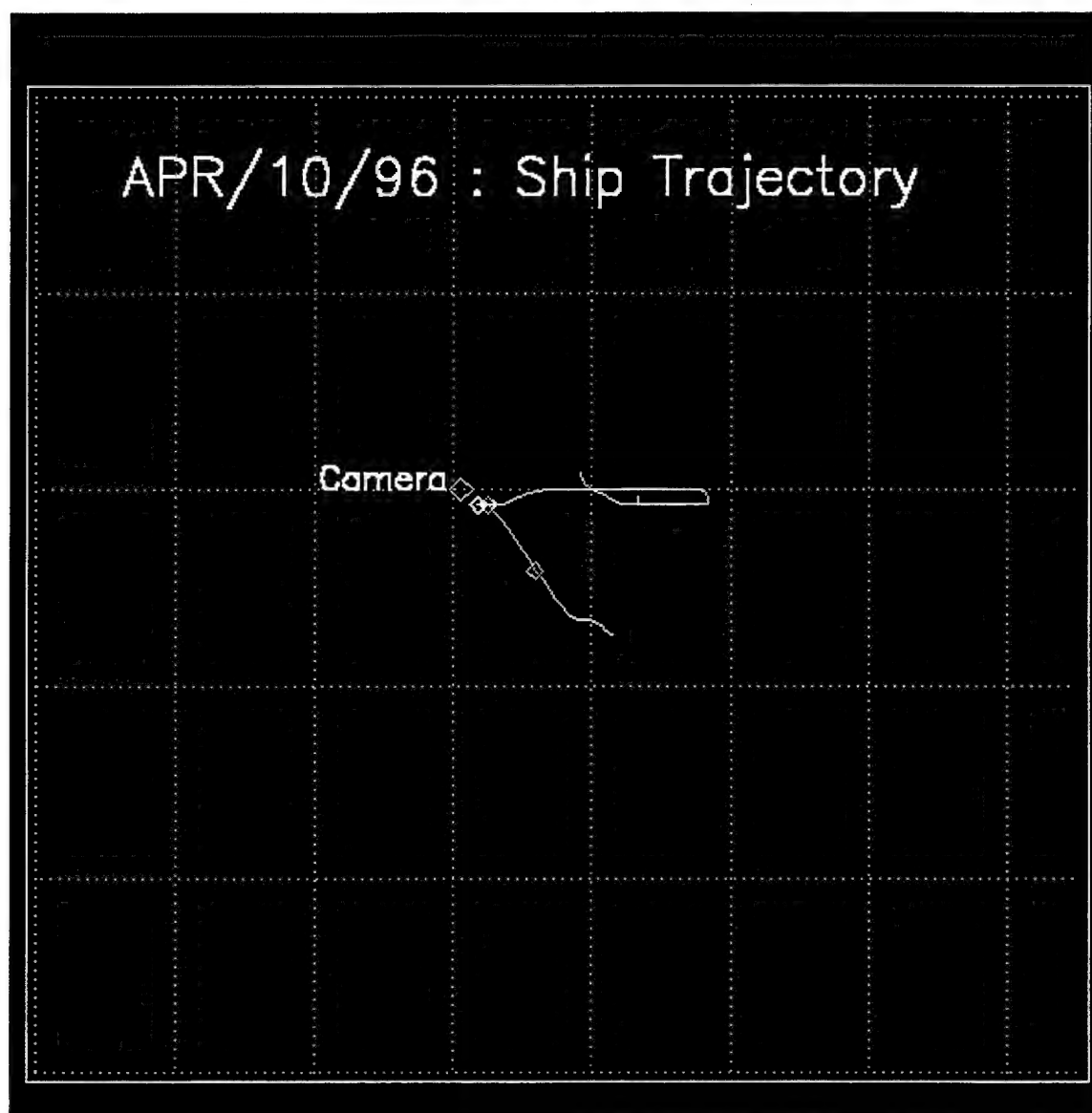


Experiment area (San Diego, California). The courses on the map are the courses that

R/V POINT SUR was to follow during the experiment.



Ship's trajectory on 9 April 1996.



Ship's trajectory on 10 April 1996.



## APPENDIX B

### POLARIZER FILTERS

#### Description :

The two following figures show the performance curves for the KRS-5 substrate, 9.5mm polarizers used in the camera setting positions 4 and 5 respectively.

#### Conditions :

The data were provided by the manufacturer of the polarizers, Graseby-Specac. The measurements were taken with a spectrometer using the actual filter shipped. Where two filters were required for the crossed-grid measurement (trace 3), another polarizer nearly identical to the one shipped is used.

#### Notes :

Trace 1:  $E_v$  i.e. optical power transmitted by the polarizer with its grid lines vertical.

Trace 2:  $E_h$  i.e. optical power transmitted by the polarizer with its grid lines horizontal.

Trace 3:  $E_l$  i.e. optical power transmitted by a pair of polarizers with grids crossed

Vertical axis : Wavenumber/wavelength

Horizontal axis: Transmittance

The principal transmittances  $K_1$  and  $K_2$  of a polarizer are defined as the transmittances of the polarizer for radiation whose electric field vector is (respectively) perpendicular to and parallel to the grid lines. The full equations for  $K_1$  and  $K_2$  are:

$$K_1 = \frac{E_h + E_v}{2E_0} \left\{ 1 + \left[ 1 - \frac{4E_1E_0}{(E_h + E_v)^2} \right]^{1/2} \right\}$$

$$K_2 = \frac{E_h + E_v}{2E_0} \left\{ 1 - \left[ 1 - \frac{4E_1E_0}{(E_h + E_v)^2} \right]^{1/2} \right\}$$

In these equations,  $E_0$  is the total power transmitted through the measurement system with no polarizers in the beam. For the attached traces, the spectrometer output was normalized such that  $E_0 = 1.00$  (i.e. 100%) for all wavelengths. As can be seen from trace 3,  $E_1$  is small over the operating wavelength range of the polarizer. Consequently, the above equation may be simplified (for wavelengths within the operating range) to the following approximate expressions:

$$K_1 = \frac{E_h + E_v}{E_0}$$

$$K_2 = \frac{E_1}{E_h + E_v}$$

So for the specific case the bandwidth of interest is from 8 to 12.5  $\mu m$  . From the curves

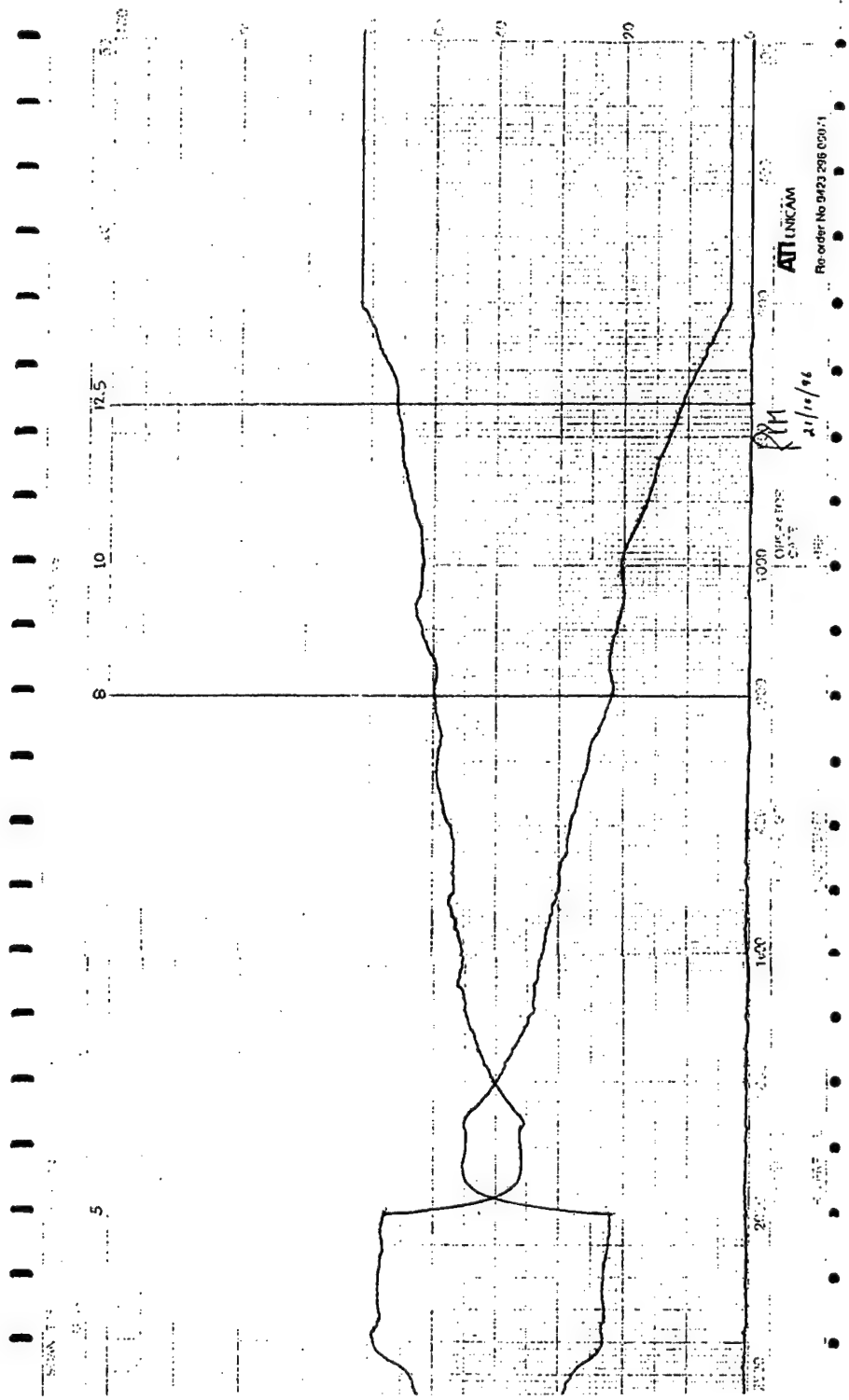
$E_h=0.17$  and  $E_v=0.53$ .  $E_0=1$ , thus

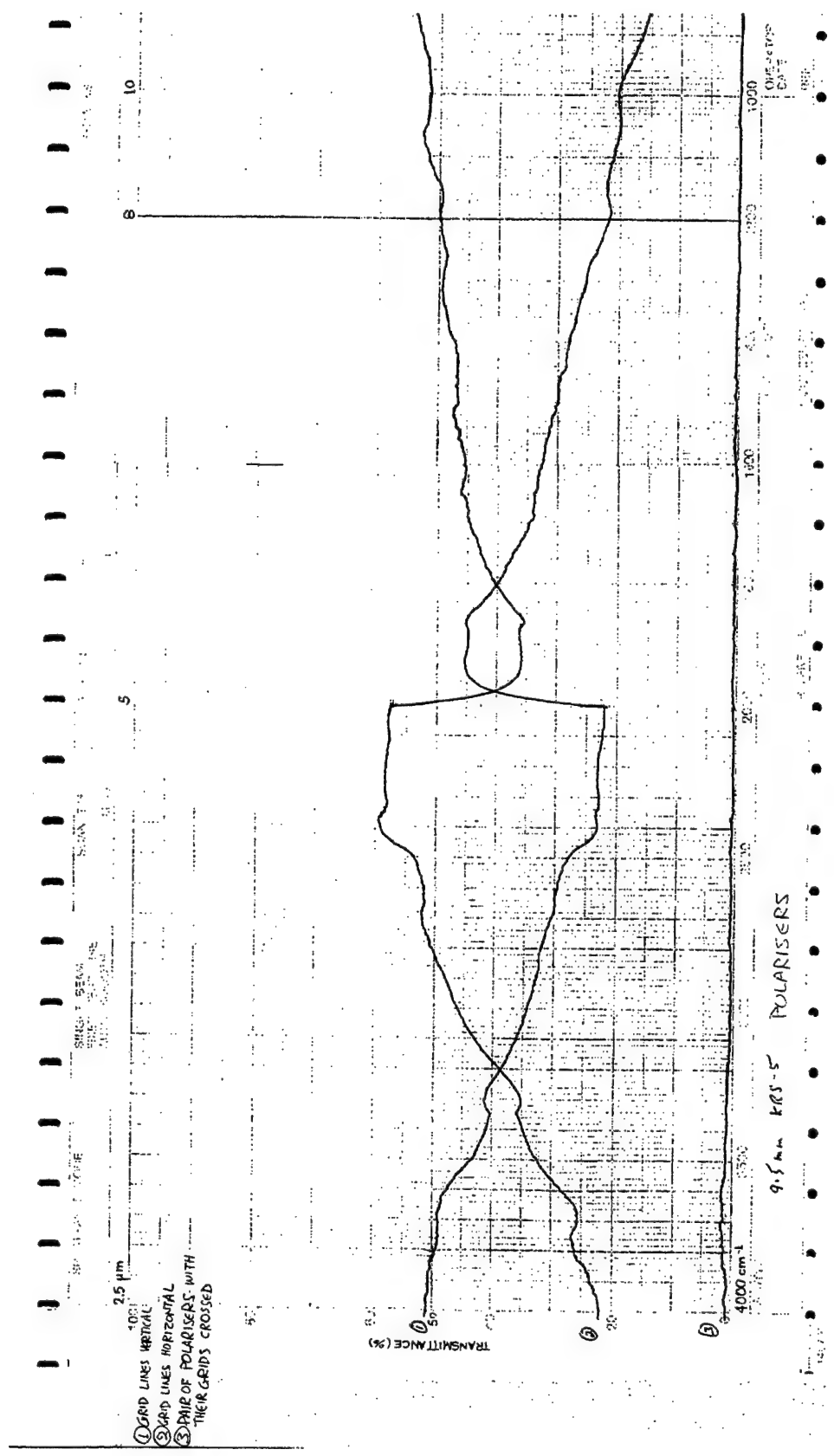
$$K_1 = \frac{E_h + E_v}{E_0} = \frac{0.17 + 0.53}{1} = 0.70$$

The polarizing filter transmittance for non polarized waves in the 8 to 12.5  $\mu m$  , is 0.7.

For this region the average value from the Trace 2 ( $E_h$  i.e. optical power transmitted by the polarizer with its grid lines horizontal) is 0.5. So these two values will multiply the background and the ship plus path radiance respectively to provide the energy reaching the sensor after passing through the polarizing filter.







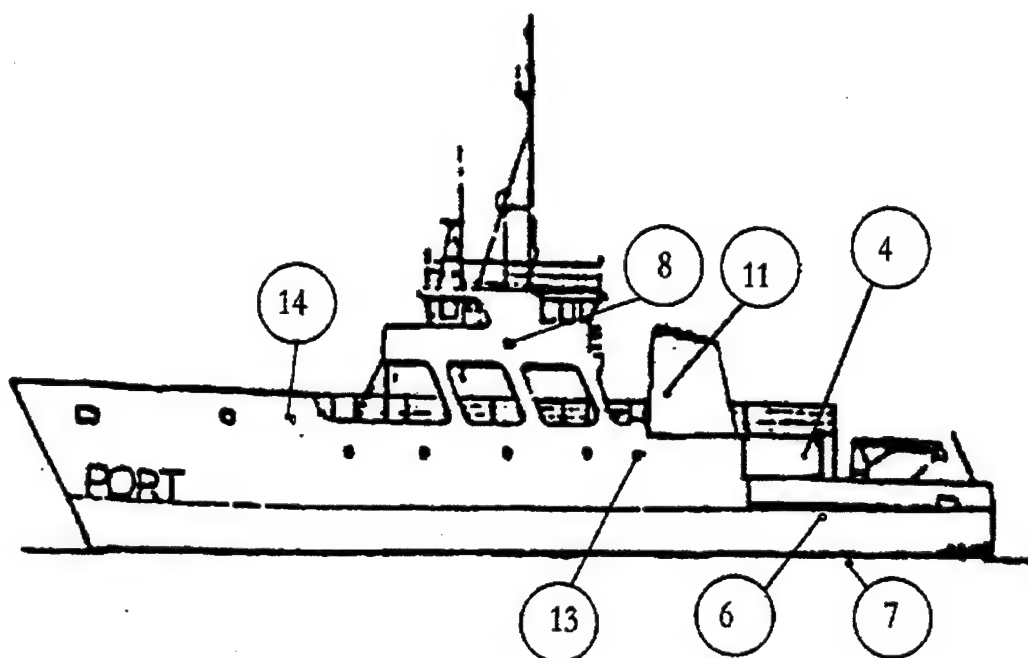
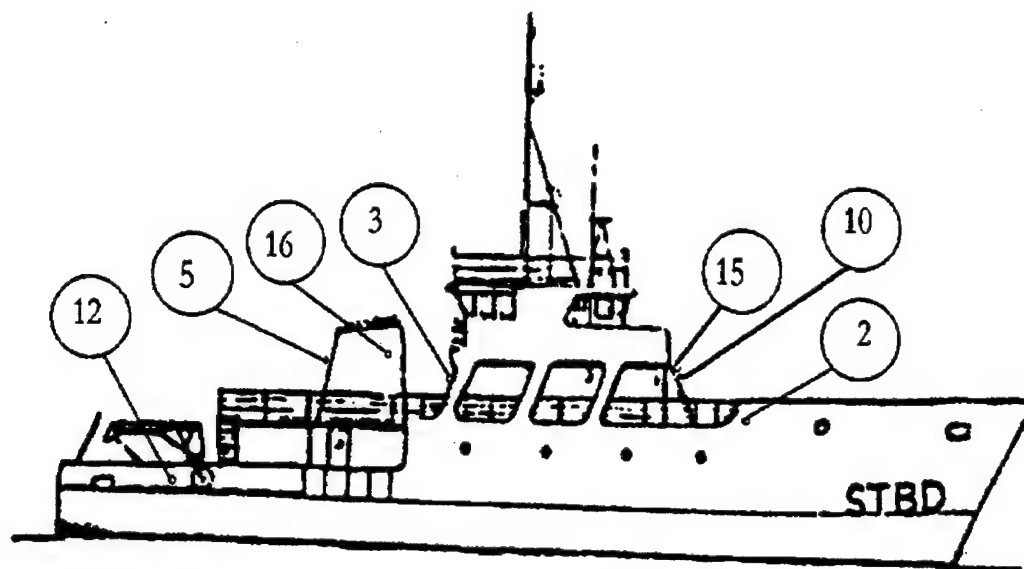


**APPENDIX C**  
**R/V POINT SUR**



**Research Vessel Point Sur**





Location of the thermistors onboard R/V Point Sur.



## APPENDIX D

### SEARAD

This is an example of the tape5-input files used in SeaRad. The atmospheric model was obtained from the meteorological data from the experiment.

F	7	3	2	1	2	2	2	2	2	2	1	1	0	289.95	-5
	3	1	0	7	0	0	0.000	7.000		4.481		0.000	0.000		0.000
	34	0	0		METEOR DATA										
	0.003	1018.000	14.300	75.000	ABH										
	0.009	1017.700	15.000	63.000	ABH										
	0.017	1016.700	14.800	63.000	ABH										
	0.034	1014.700	14.300	65.000	ABH										
	0.046	1013.200	14.000	66.000	ABH										
	0.056	1012.000	13.900	67.000	ABH										
	0.069	1010.500	13.800	68.000	ABH										
	0.075	1009.800	13.700	68.000	ABH										
	0.087	1008.300	13.600	69.000	ABH										
	0.100	1006.800	13.500	69.000	ABH										
	0.112	1005.300	13.400	69.000	ABH										
	0.130	1003.100	13.200	70.000	ABH										
	0.155	1000.200	13.000	71.000	ABH										
	0.163	999.200	12.800	72.000	ABH										
	0.183	996.800	12.700	72.000	ABH										
	0.216	992.900	12.400	73.000	ABH										
	0.243	989.800	12.100	74.000	ABH										
	0.267	986.900	12.000	75.000	ABH										
	0.304	982.500	11.800	76.000	ABH										
	0.332	979.200	11.700	76.000	ABH										
	0.381	973.500	11.500	77.000	ABH										
	0.418	969.200	11.200	78.000	ABH										
	0.497	960.000	11.200	77.000	ABH										
	0.525	956.700	11.300	77.000	ABH										
	0.588	949.500	11.100	77.000	ABH										
	0.613	946.700	11.300	74.000	ABH										
	0.655	941.900	12.100	56.000	ABH										
	0.696	937.300	14.300	24.000	ABH										
	0.738	932.700	15.800	12.000	ABH										
	0.800	925.900	15.500	12.000	ABH										
	0.847	920.800	15.100	12.000	ABH										
	0.892	915.800	15.300	9.000	ABH										
	0.956	908.900	15.500	8.000	ABH										
	1.004	903.800	15.700	7.000	ABH										
	0.100	0.000	90.310	00.000	0.000	0.00	0	85.077	T						
1	2	99	0												
32.665	117.242	0.000	0.000	20.238	198.923	0.000	0.000								
833	1250	10	5	0											
0															



This is an example of a SeaRad out file of the previous tape5 file.

\*\*\*\*\* SEARAD, A MODIFICATION OF LOWTRAN7 \*\*\*\*\*

DATE: 03/02/1999

TIME: 20:43:37.21

THERMAL PLUS SOLAR RADIANCE MODE

MULTIPLE SCATTERING USED

MARINE AEROSOL MODEL USED

WIND SPEED	=	7.00 M/SEC
WIND SPEED	=	4.48 M/SEC, 24 HR AVERAGE
RELATIVE HUMIDITY	=	74.94 PERCENT
AIRMASS CHARACTER	=	7.0
VISIBILITY	=	.00 KM

SLANT PATH TO SPACE

H1	=	.100 KM
HMIN	=	.000 KM
ANGLE	=	90.310 DEG

FREQUENCY RANGE

IV1	=	830 CM-1 ( 12.05 MICROMETERS)
IV2	=	1250 CM-1 ( 8.00 MICROMETERS)
IDV	=	10 CM-1
IFWHM	=	5 CM-1
IFILTER	=	0

SUMMARY OF THE GEOMETRY CALCULATION

H1	=	.100 KM
H2	=	.000 KM
ANGLE	=	90.310 DEG
RANGE	=	29.376 KM
BETA	=	.264 DEG
PHI	=	89.901 DEG
HMIN	=	.000 KM
BENDING	=	.053 DEG
LEN	=	0

SEA AT 289.95 K REPLACES BLACK BODY BOUNDARY

UPWIND	=	85.077 DEG EAST OF LINE OF SIGHT
--------	---	----------------------------------

SUMMARY OF OBSERVATION GEOMETRY

BETA	=	.26417 DEG
PATH AZIMUTH	=	198.923 DEG EAST OF NORTH
WIND AZIMUTH	=	284.000 DEG EAST OF NORTH
RECEIVER LATITUDE	=	32.665 NORTH OF EQUATOR
RECEIVER LONGITUDE	=	117.242 WEST OF GREENWICH
FOOTPRINT LATITUDE	=	32.415 NORTH OF EQUATOR
FOOTPRINT LONGITUDE	=	117.343 WEST OF GREENWICH
SUBSOLAR LATITUDE	=	7.057 DEG NORTH OF EQUATOR

SUBSOLAR LONGITUDE = 122.989 DEG WEST OF GREENWICH

VALUES SEEN FROM FOOTPRINT

RECEIVER ZENITH ANGLE = 89.901 DEG  
 RECEIVER AZIMUTH = 265.132 DEG WEST OF UP WIND  
 SOLAR ZENITH ANGLE = 25.897 DEG  
 SOLAR AZIMUTH = 91.084 DEG WEST OF UP WIND  
 SOLAR SPECULAR TILT = 32.192 DEG ( 4.89 SIGMA, PROB= 5.282E-05)

ZERO RANGE UNPOLARIZED VALUES

SEA EMISSION = 20.01836 W M-2 SR-1 (AV. EMISS. .6071)  
 SKY REFLECTION = 4.61739 W M-2 SR-1  
 SUN GLINT = .00002 W M-2 SR-1  
 TOTAL RADIANCE = 24.63576 W M-2 SR-1  
 BLACK BODY TEMP. = 1.1 C

FULL RANGE UNPOLARIZED VALUES

SEA EMISSION = 1.02095 W M-2 SR-1  
 SKY REFLECTION = .21319 W M-2 SR-1  
 SUN GLINT = .00000 W M-2 SR-1  
 PATH TO FOOTPRINT = 29.24329 W M-2 SR-1 (AV. TRANS. .0514)  
 TOTAL RADIANCE = 30.47743 W M-2 SR-1  
 BLACK BODY TEMP. = 12.5 C

	HORIZONTAL (W M-2 SR-1)	VERTICAL (W M-2 SR-1)	(H-V) / (H+V) (%)
--	----------------------------	--------------------------	----------------------

ZERO RANGE POLARIZED VALUES

SEA EMISSION	8.88451	11.13385	-11.2
SKY REFLECTION	2.63338	1.98401	14.1
SUN GLINT	.00002	.00000	92.0
TOTAL RADIANCE	11.51791	13.11785	-6.5
BLACK BODY TEMP. (C)	-33.5	-28.2	

FULL RANGE POLARIZED VALUES

SEA EMISSION	.45213	.56882	-11.4
SKY REFLECTION	.12153	.09166	14.0
SUN GLINT	.00000	.00000	.0
PATH TO FOOTPRINT	14.62165	14.62165	.0
TOTAL RADIANCE	15.19530	15.28213	-.3
BLACK BODY TEMP. (C)	-21.9	-21.6	



## APPENDIX E

### METEOROLOGICAL DATA

#### 1. METOC FILES

##### Storage format for METOC01 (DASC) data

The data is stored in a set of files with the names "eopace.\*" and "30sec.\*". The extension for the file name is the Julian data the file was started on. A new pair of files is started every day at 00:00 GMT. The time data in the files are in GMT. The eopace files have the data averaged over 10 minutes. The 30sec files have the GPS data averaged over 30 seconds and the last set of data from the Campbell. In the 30sec file, the Campbell data are not averaged. The data format for both files is the same. Each file has a header that tells when the file was started. Each file has a footer that tells when the file was finished. Some files may also have additional start and stop times interspersed with data, depending on whether data logging was turned off or the program was stopped before the end of the day. The data are arranged in fields separated by spaces across a line of text. A carriage return character and a line feed character are at the end of each line. Each new reading is on a new line. The fields are in the order below. The numbers before the fields are not in the data. They serve to make identifying fields easier.

- 01        Number of readings in this average, nn
- 02        Year, yyyy
- 03        Julian date, ddd
- 04        Hours and minutes, hhmm

05	Seconds, ss
06	Relative wind speed, m/s, mmm
07	Relative wind direction, degrees, ddd
08	Ship speed, knots, at present always 0
09	Ship direction, degrees, at present always 090
10	True wind speed, m/s, mmm
11	True wind direction, degrees, ddd
12	T air, degrees C, tt.t
13	RH, per cent, pp
14	Pressure, millibars, pppp.p
15	Sea surface temperature, degrees C, tt.t
16	GPS time, hhmmss
17	GPS latitude, ddmm.m
18	GPS North/South indicator, either 'N' or 'S'
19	GPS longitude, dddmm.m
20	GPS East/West indicator, either 'E' or 'W'
21	GPS speed over ground, knots, kk.k
22	GPS course over ground, degrees, ddd.
23	GPS antenna height, meters, mm.m

An example of the storage format is presented in the following pages.

### **Storage format for METOC02 data**

The METOC02 system had two additional temperature sensors and two additional RH sensors. The data are arranged slightly differently than the METOC01 system. The data is stored in a set of files with the names "eospace.\*" and "30sec.\*". The extension for the file name is the Julian date the file was started on. A new pair of files is started every day at 00:00 GMT. The time data in the files are in GMT. The eospace files have the data averaged over 10 minutes.

The 30sec file have the GPS data averaged over 30 seconds and the last set of data from the Campbell. In the 30sec file, the Campbell data are not averaged. The data format for both files is the same. Each file has a header that tells when the file was started. Each file has a footer that tells when the file was finished. Some files may also have additional start and stop times interspersed with data, depending on whether data logging was turned off or the program was stopped before the end of the day. The data are arranged in fields separated by spaces across a line of text. A carriage return character and a line feed character are at the end of each line. Each new reading is on a new line. The fields are in the order below. The numbers before the fields are not in the data. They serve to make identifying fields easier.

- 01        Number of readings in this average, nn
- 02        Year, yyyy
- 03        Julian date, ddd
- 04        Hours and minutes, hhmm
- 05        Seconds, ss

06	Relative wind speed, m/s, mmm
07	Relative wind direction, degrees, ddd
08	Ship speed, knots, at present always 0
09	Ship direction, degrees, at present always 090
10	True wind speed, m/s, mmm
11	True wind direction, degrees, ddd
12	T air, degrees C, tt.t
13	RH, per cent, pp
14	Pressure, millibars, pppp.p
15	Sea surface temperature, degrees C, tt.t
16	T air A, degrees C, tt.t
17	RH A, per cent, pp
18	T air B, degrees C, tt.t
19	RH B, per cent, pp
20	Delimiter between Campbell data and GPS data, "****"
21	GPS time, hhmmss
22	GPS latitude, ddmm.m
23	GPS North/South indicator, either 'N' or 'S'
24	GPS longitude, dddmm.m
25	GPS East/West indicator, either 'E' or 'W'
26	GPS speed over ground, knots, kk.k
27	GPS course over ground, degrees, ddd.

28      GPS antenna height, meters, mm.m

An example of the storage format is presented in the following page.



## METOC 1 FORMAT

Data logging started at Tue Apr 09 00:00:00 1996

30	1996	99	2355	44	2	156	0	090	6	294	15.4	81	1016.2
21.2	000024	3311.2	N	11728.2	W	6.3	124.3	56.8					
30	1996	99	2355	44	2	156	0	090	6	294	15.4	81	1016.2
21.2	000054	3311.2	N	11728.2	W	6.3	123.9	52.5					
30	1996	99	2355	44	2	156	0	090	6	294	15.4	81	1016.2
21.2	000124	3311.1	N	11728.1	W	6.3	123.5	42.0					
30	1996	99	2355	44	2	156	0	090	6	294	15.4	81	1016.2
21.2	000154	3311.1	N	11728.0	W	6.3	123.0	26.9					
30	1996	99	2355	44	2	156	0	090	6	294	15.4	81	1016.2
21.2	000224	3311.1	N	11728.0	W	6.4	121.6	9.9					
30	1996	99	2355	44	2	156	0	090	6	294	15.4	81	1016.2
21.2	000254	3311.1	N	11727.9	W	6.3	120.5	-4.2					
30	1996	99	2355	44	2	156	0	090	6	294	15.4	81	1016.2
21.2	000324	3311.0	N	11727.9	W	5.9	129.6	-10.7					
30	1996	99	2355	44	2	156	0	090	6	294	15.4	81	1016.2
21.2	000354	3311.0	N	11727.9	W	4.1	185.6	-6.7					
30	1996	99	2355	44	2	156	0	090	6	294	15.4	81	1016.2
21.2	000424	3311.0	N	11727.9	W	4.1	233.5	9.0					

## METOC 2 FORMAT

Data logging started at Tue Apr 09 00:00:00 1996

30	1996	99	2352	32	2	138	0	090	5	288	16.5	75	1016.9
16.8	0.0	0.0	0.0	0.0***	000035	3311.2	N	11728.2	W	6.3	124.3	46.3	
30	1996	99	2352	32	2	138	0	090	5	288	16.5	75	1016.9
16.8	0.0	0.0	0.0	0.0***	000105	3311.1	N	11728.1	W	6.3	124.2	40.7	
30	1996	99	2352	32	2	138	0	090	5	288	16.5	75	1016.9
16.8	0.0	0.0	0.0	0.0***	000135	3311.1	N	11728.1	W	6.2	123.6	29.4	
29	1996	99	2352	32	2	138	0	090	5	288	16.5	75	1016.9
16.8	0.0	0.0	0.0	0.0***	000205	3311.1	N	11728.0	W	6.4	122.3	14.0	
30	1996	100	0002	8	2	149	0	090	5	292	16.2	76	1016.9
16.6	0.0	0.0	0.0	0.0***	000235	3311.1	N	11728.0	W	6.3	121.4	-2.1	
30	1996	100	0002	8	2	149	0	090	5	292	16.2	76	1016.9
16.6	0.0	0.0	0.0	0.0***	000305	3311.0	N	11727.9	W	6.2	120.7	-13.8	
30	1996	100	0002	8	2	149	0	090	5	292	16.2	76	1016.9
16.6	0.0	0.0	0.0	0.0***	000335	3311.0	N	11727.9	W	4.6	159.8	-17.5	
30	1996	100	0002	8	2	149	0	090	5	292	16.2	76	1016.9
16.6	0.0	0.0	0.0	0.0***	000405	3311.0	N	11727.9	W	3.7	216.5	-10.2	
30	1996	100	0002	8	2	149	0	090	5	292	16.2	76	1016.9
16.6	0.0	0.0	0.0	0.0***	000435	3311.0	N	11727.9	W	3.8	259.1	8.3	

## 2. RADIOSONDE DATA

The following data are the radiosonde data collected during the experiment. The data were provided by the Meteorological department of the Naval Postgraduate School.

Sounding program REV 7.62 using Omega

Ship : POINT SUR  
Location : 32.95 N 117.44 W 3 m

Rejected Sigma stations: a,b,c

Phase fitting length is 250 s from 0 min to 120 min

Sounding : 44  
RS-number: 542520109

No PTU editing  
No wind editing

Started at: 9 APR 96 13:49 GMT

Time	AscRate	Hgt/MSL	Pressure	Temp	RH	Dewp	Dir	Speed	WndStat
min s	m/s	m	hPa	degC	%	degC	deg	m/s	
0 0	0.0	3	1017.9	14.0	74	9.5	279	3.3	-----
0 2	4.0	11	1016.9	15.3	62	8.1	///	////	--CDE-GH-
0 4	4.7	22	1015.7	15.2	61	7.8	///	////	--CDE-GH-
0 6	6.2	40	1013.5	14.8	64	8.1	///	////	--CDE-GH-
0 8	4.9	42	1013.2	14.4	64	7.7	///	////	--CDE-GH-
0 10	5.1	54	1011.7	14.1	65	7.7	328	1.4	--CDE-GH-
0 12	5.2	65	1010.5	13.8	66	7.6	///	////	--CDE-GH-
0 14	5.0	73	1009.5	13.7	67	7.7	///	////	--CDE-GH-
0 16	5.1	85	1008.0	13.6	69	8.1	///	////	--CDE-GH-
0 18	4.8	89	1007.6	13.5	69	8.0	///	////	--CDE-GH-
0 20	4.8	100	1006.3	13.4	70	8.1	343	0.9	--CDE-GH-
0 22	5.0	114	1004.6	13.3	70	8.0	///	////	--CDE-GH-
0 24	4.8	118	1004.1	13.2	70	7.9	///	////	--CDE-GH-
0 26	5.1	136	1001.9	13.1	71	8.0	///	////	--CDEFGH-
0 28	4.7	136	1001.9	13.0	71	7.9	///	////	--CDEFGH-
0 30	4.7	143	1001.2	13.0	71	7.9	347	1.2	--CDEFGH-
0 32	4.9	159	999.2	12.8	72	7.9	///	////	--CDEFGH-
0 34	4.7	163	998.7	12.8	73	8.1	///	////	--CDEFGH-
0 36	4.7	181	996.5	12.6	73	7.9	///	////	--CDEFGH-
0 38	4.8	187	995.8	12.6	74	8.1	///	////	--CDEFGH-
0 40	4.8	198	994.6	12.5	74	8.0	7	0.8	--CDEFGH-
0 42	4.8	210	993.1	12.3	74	7.9	///	////	--CDEFGH-
0 44	4.8	216	992.4	12.3	74	7.9	///	////	--CDEFGH-
0 46	4.8	230	990.7	12.1	75	7.9	///	////	--CDEFGH-
0 48	4.8	234	990.2	12.0	76	8.0	///	////	--CDEFGH-
0 50	4.8	245	989.0	12.0	76	8.0	38	0.5	--CDEFGH-

0 52	4.8	259	987.3	11.8	77	8.0	///	////	--CDEFGH-
0 54	5.0	269	986.1	11.7	77	7.9	///	////	--CDEFGH-
0 56	5.0	287	984.0	11.6	78	7.9	///	////	--CDEFGH-
0 58	5.2	291	983.5	11.5	78	7.8	///	////	--CDEFGH-
1 0	5.2	300	982.5	11.4	78	7.8	32	0.5	--CDEFGH-
1 2	5.1	312	981.1	11.3	79	7.8	///	////	--CDEFGH-
1 4	5.2	318	980.4	11.2	79	7.7	///	////	--CDEFGH-
1 6	4.8	324	979.7	11.1	79	7.6	///	////	--CDEFGH-
1 8	4.8	330	978.9	11.1	80	7.8	///	////	--CDEFGH-
1 10	4.7	340	977.7	11.0	80	7.7	0	0.0	--CDEFGH-
1 12	4.7	350	976.6	10.9	81	7.8	///	////	--CDEFGH-
1 14	4.8	359	975.6	10.8	81	7.7	///	////	--CDEFGH-
1 16	4.6	369	974.4	10.8	81	7.7	///	////	--CDEFGH-
1 18	4.8	379	973.2	10.7	82	7.8	///	////	--CDEFGH-
1 20	4.7	385	972.5	10.6	82	7.7	0	0.0	--CDEFGH-
1 22	4.6	397	971.1	10.3	83	7.6	///	////	--CDEFGH-
1 24	4.4	401	970.6	10.4	83	7.7	///	////	--CDEFGH-
1 26	4.1	411	969.4	10.3	84	7.8	///	////	--CDEFGH-
1 28	4.3	419	968.5	10.2	84	7.7	///	////	--CDEFGH-
1 30	4.3	429	967.3	10.1	85	7.7	0	0.0	--CDEFGH-
1 32	4.3	440	966.1	10.0	85	7.6	///	////	--CDEFGH-
1 34	4.3	446	965.4	10.0	86	7.8	///	////	--CDEFGH-
1 36	4.4	456	964.2	9.8	87	7.8	///	////	--CDEFGH-
1 38	4.3	460	963.8	9.8	87	7.8	///	////	--CDEFGH-
1 40	4.2	466	963.1	9.7	88	7.9	0	0.0	--CDEFGH-
1 42	4.3	478	961.7	9.6	88	7.8	///	////	--CDEFGH-
1 44	4.2	486	960.7	9.6	89	7.9	///	////	--CDEFGH-
1 46	4.1	492	960.0	9.5	89	7.8	///	////	--CDEFGH-
1 48	4.3	508	958.1	9.4	90	7.9	///	////	--CDEFGH-
1 50	4.3	514	957.4	9.3	90	7.8	178	0.6	--CDEFGH-
1 52	4.5	533	955.3	9.1	91	7.8	///	////	--CDEFGH-
1 54	4.7	541	954.4	9.1	91	7.8	///	////	--CDEFGH-
1 56	4.5	545	953.9	9.0	91	7.7	///	////	--CDEFGH-
1 58	4.7	559	952.3	8.9	92	7.7	///	////	--CDEFGH-
2 0	4.5	563	951.8	8.8	92	7.6	182	0.8	--CDEFGH-
2 2	4.4	573	950.7	8.7	93	7.7	///	////	--CDEFGH-
2 4	4.5	581	949.8	8.6	93	7.6	///	////	--CDEFGH-
2 6	4.3	585	949.3	8.6	93	7.6	///	////	--CDEFGH-
2 8	4.6	597	947.9	8.5	94	7.6	///	////	--CDEFGH-
2 10	4.6	605	947.0	8.4	94	7.5	181	1.1	--CDEFGH-
2 12	4.9	625	944.7	8.3	95	7.6	///	////	--CDEFGH-
2 14	5.0	637	943.3	8.2	95	7.5	///	////	--CDEFGH-
2 16	5.0	641	942.8	8.1	96	7.5	///	////	--CDEFGH-
2 18	5.1	661	940.5	8.0	96	7.4	///	////	--CDEFGH-
2 20	5.2	671	939.4	8.0	96	7.4	171	1.7	--CDEFGH-
2 22	4.9	681	938.2	7.9	96	7.3	///	////	--CDEFGH-
2 24	5.0	690	937.3	7.8	96	7.2	///	////	--CDEFGH-
2 26	5.2	700	936.2	7.7	96	7.1	///	////	--CDEFGH-
2 28	5.2	714	934.6	7.6	96	7.0	///	////	--CDEFGH-
2 30	5.2	720	933.9	7.5	96	6.9	175	2.0	--CDEFGH-
2 32	5.3	732	932.5	7.4	96	6.8	///	////	--CDEFGH-
2 34	5.2	738	931.8	7.4	96	6.8	///	////	--CDEFGH-
2 36	5.3	744	931.2	7.4	91	6.1	///	////	--CDEFGH-
2 38	5.4	760	929.3	7.7	88	5.9	///	////	--CDEFGH-

2 40	5.4	768	928.4	7.9	82	5.1	176	2.5	--CDEFGH-
2 42	5.3	784	926.6	10.1	42	-2.2	///	////	--CDEFGH-
2 44	5.1	790	925.9	11.6	28	-6.2	///	////	--CDEFGH-
2 46	5.3	800	924.8	12.6	20	-9.7	///	////	--CDEFGH-
2 48	5.0	810	923.7	14.1	17	-10.5	///	////	--CDEFGH-
2 50	4.9	817	923.0	14.4	16	-11.0	178	3.0	--CDEFGH-
2 52	4.7	823	922.3	14.9	15	-11.5	///	////	--CDEFGH-
2 54	4.6	827	921.9	15.0	14	-12.2	///	////	--CDEFGH-
2 56	4.4	833	921.2	15.1	14	-12.1	///	////	--CDEFGH-
2 58	4.2	841	920.3	15.1	13	-13.1	///	////	--CDEFGH-
3 0	4.1	843	920.1	15.2	13	-13.0	181	3.3	--CDEFGH-
3 2	3.9	850	919.4	15.2	13	-13.0	///	////	--CDEFGH-
3 4	4.0	858	918.5	15.2	12	-14.0	///	////	--CDEFGH-
3 6	3.9	860	918.3	15.2	12	-14.0	///	////	--CDEFGH-
3 8	3.5	864	917.8	15.1	12	-14.1	///	////	--CDEFGH-
3 10	3.5	872	916.9	15.1	12	-14.1	183	3.7	--CDEFGH-
3 12	3.2	880	916.0	15.1	12	-14.1	///	////	--CDEFGH-
3 14	3.2	885	915.6	15.1	12	-14.1	///	////	--CDEFGH-
3 16	3.0	889	915.2	15.1	12	-14.1	///	////	--CDEFGH-
3 18	2.9	897	914.3	15.1	12	-14.1	///	////	--CDEFGH-
3 20	2.9	903	913.6	15.2	12	-14.0	186	4.1	--CDEFGH-
3 22	2.9	909	912.9	15.3	12	-13.9	///	////	--CDEFGH-
3 24	2.9	913	912.5	15.3	12	-13.9	///	////	--CDEFGH-
3 26	2.7	915	912.3	15.3	12	-13.9	///	////	--CDEFGH-
3 28	2.9	928	910.9	15.4	12	-13.8	///	////	--CDEFGH-
3 30	3.0	932	910.5	15.4	11	-14.9	187	4.6	--CDEFGH-
3 32	3.0	940	909.6	15.5	11	-14.8	///	////	--CDEFGH-
3 34	2.8	942	909.4	15.6	10	-15.9	///	////	--CDEFGH-
3 36	3.0	951	908.5	15.7	10	-15.8	///	////	--CDEFGH-
3 38	3.1	957	907.8	15.8	9	-17.0	///	////	--CDEFGH-
3 40	3.0	961	907.4	15.9	8	-18.3	189	4.9	--CDEFGH-
3 42	3.0	969	906.5	15.9	8	-18.3	///	////	--CDEFGH-
3 44	3.0	975	905.8	16.1	7	-19.7	///	////	--CDEFGH-
3 46	3.1	982	905.2	16.2	7	-19.6	///	////	--CDEFGH-
3 48	3.1	990	904.3	16.3	7	-19.6	///	////	--CDEFGH-
3 50	3.0	992	904.1	16.5	7	-19.4	193	5.0	--CDEFGH-
3 52	3.0	998	903.4	16.5	7	-19.4	///	////	--CDEFGH-
3 54	3.1	1006	902.5	16.7	7	-19.3	///	////	--CDEFGH-
3 56	3.3	1013	901.8	16.7	7	-19.3	///	////	--CDEFGH-
3 58	3.0	1019	901.2	16.8	7	-19.2	///	////	--CDEFGH-
4 0	3.2	1027	900.3	16.8	7	-19.2	196	5.4	--CDEFGH-
4 2	3.0	1031	899.9	16.9	7	-19.1	///	////	--CDEFGH-
4 4	3.3	1040	899.0	16.9	7	-19.1	///	////	--CDEFGH-
4 6	3.0	1042	898.8	16.9	7	-19.1	///	////	--CDEFGH-
4 8	3.2	1052	897.7	16.9	7	-19.1	///	////	--CDEFGH-
4 10	3.2	1056	897.2	16.9	7	-19.1	197	5.5	--CDEFGH-
4 12	3.0	1058	897.0	17.0	7	-19.0	///	////	--CDEFGH-
4 14	3.3	1073	895.5	16.9	7	-19.1	///	////	--CDEFGH-
4 16	3.0	1073	895.5	16.8	7	-19.2	///	////	--CDEFGH-
4 18	3.0	1081	894.6	16.8	7	-19.2	///	////	--CDEFGH-
4 20	3.1	1085	894.2	16.8	7	-19.2	198	5.8	--CDEFGH-
4 22	3.1	1091	893.5	16.8	7	-19.2	///	////	--CDEFGH-
4 24	3.2	1102	892.4	16.8	7	-19.2	///	////	--CDEFGH-
4 26	3.1	1106	892.0	16.8	7	-19.2	///	////	--CDEFGH-



## APPENDIX F

### CONVERSION OF TEMPERATURE TO IN BAND RADIANCE

```
% Program name: rad.m
% Conversion of the temperature difference
% into in-band background radiance

clear;
Tmin=238.; % Initial temperature
dT=0.01;   % Step
n=200;     % Number of values

disp('Temperature    Radiance');

h=6.626e-34; % Planck's constant
c=2.998e8;   % Speed of light
k=1.382e-23; % Boltzmann constant
a=8e-6;
b=12.05e-6;
dx=0.001e-6;

for T=Tmin:dT:Tmin+n*dT

    sf=0.0;

    for x=a:dx:b-dx % Calculation loop

        xm=x+dx/2;

        f1=(2*h*c^2)/(xm^5);
        f2=1/(exp((h*c)/(xm*k*T))-1);
        fx=f1*f2;
        sf=sf+fx*dx;

    end;

    disp([T,sf]);

end;
```



## APPENDIX G

### CALCULATION OF APPARENT TEMPERATURE DIFFERENCE $\Delta T_{app}$

For the computation of the effective temperature difference, the target and background temperatures were initially converted to in-band radiances by application of the Planck function:

$$N_s = \frac{\epsilon \sigma T^4 \Delta q}{\pi}$$

where:

$\epsilon$  = emissivity

$\sigma$  = Stefan-Boltzmann constant =  $5.6697 \times 10^{-12}$  [W/m<sup>2</sup>K<sup>4</sup>]

$T$  = source temperature [K]

$\Delta q$  = fraction of the thermally emitted radiance lying in the band from  $\lambda_1$  to  $\lambda_2$  at

source temperature  $T$

So it is:  $q_1 = \lambda_1 T$ ,  $q_2 = \lambda_2 T$  and  $\Delta q = q_2 - q_1$

With the use of SEARAD the attenuated radiance and path radiance were calculated for the desired range. The attenuation from the polarizing filter was also calculated and the final amount of energy reaching the sensor was thus obtained. Then by using the Planck function, the radiance was converted back to temperature difference, the apparent temperature difference for the specific range and geometry.





## APPENDIX H

### CALCULATION OF MRT AND MTF

```
% Program mrt.m
% Calculation of MRT and MTF
% Lt S.Lagaras H.N.

FOVx=119.72959 ; % In mRad (=6.86 degrees)
FOVy=90.05899188; % In mRad (=5.16 degrees)
SNRT=2.5; % Signal to Noise Ratio
% NET=0.125; % Noise Equivalent Temperature (if you want
to use this deactivate other NET)
dx=0.1; % in scan detector subtense in mrad
dy=0.1; % cross scan detector subtense in mrad
L=7; % Length to width ratio of the bar 7:1
Te=0.1; % Eye integration time in seconds
Nss=1; % Serial scan ratio
Nos=1; % Overscan ratio
Fr=30; % Frame rate in Hz (1/sec)
D=0.1; % Aperture diameter in meters
wl=10*10(-6); % Approximation of the radiation
wavelength
l=41.5; % Length of the ship in meters
w=9.75; % Width of the ship in meters
h=8.8; % Height of the ship in meters

%%%%% Calculation of back end resolution (Shumaker 7-81)
%rb=0.095; % Back end resolution in mRad
td=6*10(-5); % Dwell time in seconds
fstar=30*103; % Freq at which the detector response is down
3db

% from its low freq response

% Detector electronics resolution (rf)
Vs=dx/td; % Angular scan velocity in mrad/sec
rf=Vs/(fstar*pi);

% Preamplifier resolution (rp)
DFp=8.5*106; % Half power frequency response of the
preamplifier in HZ
rp=0.32*pi*Vs/(2*DFp);
```

```

% Multiplexer resolution (rm)
Ns=2; % # of multiplexer samples per detector dwell time
rm=dx/Ns;

% Display resolution (rd)
HD=0.2; % Display height in meters
dss=3.43*10^(-4); % Display spot size in meters
rd=1.9*dss*FOVy/HD;

% Eye resolution (re)
% Assume display brightness of 5 fl so that re=1.2/M
(Shumaker pg 7-92)
Dv=0.5; % Display viewing distance in meters
M=(2*10^3*atan(HD/(2*Dv)))/FOVy; % System magnification
re=1.2/M;

% Image motion resolution (rs)
AR=0.015; % Amplitude of residual image motion in mRad
rs=3.55*AR; % (Shumaker pg 7-94)

rb=sqrt(rf^2+rp^2+rm^2+rd^2+re^2+rs^2) % Back end
resolution in mrad

%%%%% Variables used for NET calculation

to=0.70; % Transmission of the optics
Nd=180; % Number of detectors
Nsc=0.75; % Scan efficiency
Ds=4*10^10; % Specific detectivity in [cm Hz1/2 Watt-1]
DNDDT=6.27*10^(-5); % Derivative of Plank's equation
f=0.2; % Focal length of the lens in meters

N=13; % Number of bars in the Bar chart
a=0;

R=0.0001:100:29000.0001; % Range in
meters

b=atan(1000./R);
A=(l*w*sin(b))+(h*w*cos(b)*sin(a))+(h*l*cos(b)*cos(a));
At=abs(A);
%%%%% At=214.4513; This is the value used in other
thesis

```

```
Dc=At.^(0.5) ; % Critical dimension
X=Dc/N ;
```

```
fc=D/(1000*w1); % Cut off frequency in
cycles/milliradians
fs=R./(2000*X); % Fundamental spatial freq characterizing
the target in cycl/mrad
m=fs./fc;
Ho=(2/pi)*(acos(m)-(m.*(1-m.^2).^0.5));
%Hd=sin(pi*dx*fs)/(pi*dx*fs);
MTF=Ho;
```

```
NET=(20*f*(FOVx*FOVy*Fr*Nos*Nss)^0.5)/(to*(pi*Nd*Nsc)^0.5*D
^2*dx*dy*Ds*DNDT);
```

```
Rx=(1+(2*fs.*rb).^2).^(-0.5); % Shumaker pg 8-60
```

```
MRT=2*SNRT*NET.*(Rx.^0.5).*(((fs.^2).*dx*dy/L).^0.5).*((Te*
Fr*Nos*Nss)^(-0.5))./MTF;
```

```
figure(1)
plot(R,MRT);
axis([0,29000,0,25])
grid;
ylabel('Temperature difference in Celcius');
xlabel('Range in meters');
title('MRT vs Range for Identification N=13 (Johnson)');
```

```
figure(2)
plot(m,MTF,'r');
grid;
axis([0,1.2,0,1])
ylabel('MTF');
xlabel('fs/fc');
title('MTF vs fs/fc');
```

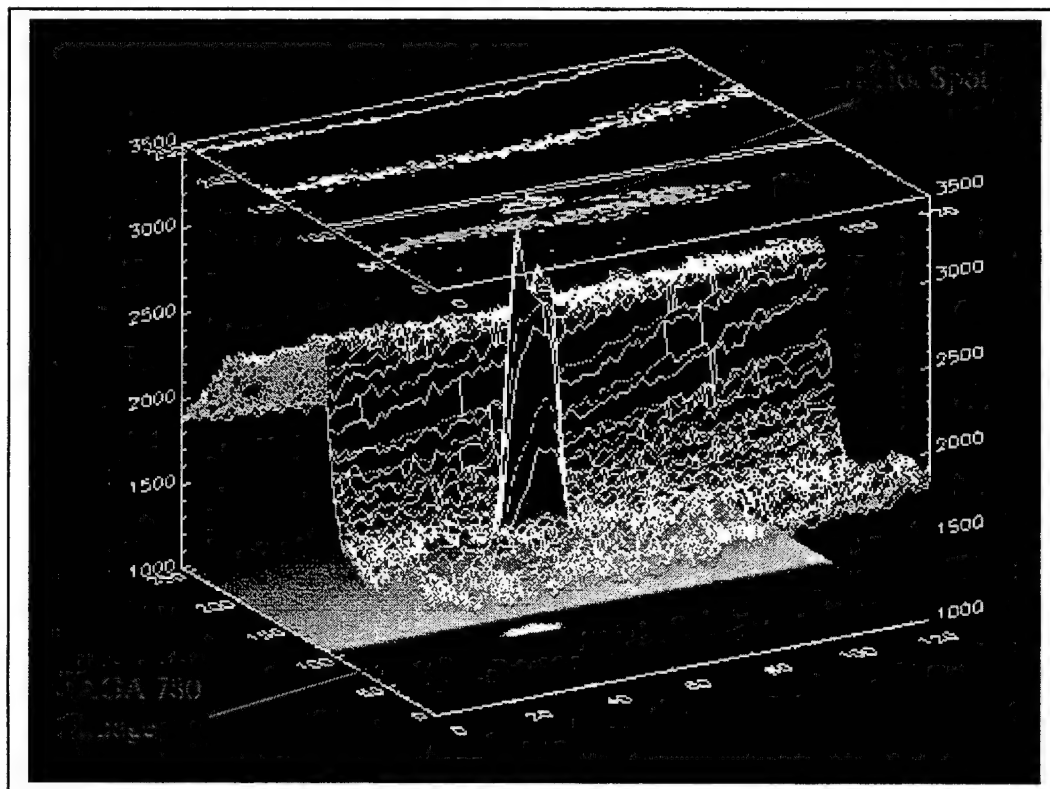
```
figure(3)
plot(fs,MTF,'r');
grid;
ylabel('MTF');
xlabel('fs');
title('MTF vs fs');
```



## APPENDIX I

### IDL OUTPUTS

A number of IDL programs originally created by M.C. Pontes and later modified to fit the needs of this work were used to obtain the temperature information of R/V POINT SUR from the reordered images. The programs used are available from professor A.W. Cooper. In the following image is presented the IDL output data in a form of an image that was used for this work. The final ship temperature was finally obtained through the average temperature of the two thermistors in the hot spot area.



IDL output image.



## APPENDIX J

### EXCEL SPREADSHEET OUTPUTS

The following table is part of the EXCEL spreadsheet that was used for calculation to  
the apparent temperature difference for the unpolarized case for the 100m scenario.

File	Range (KM)	Zenith Angle	Emissivity	Hot Spot Temp.(K)	Ship Radiance (0 Km)	Transmittance	Path Radiance	Ship+Path Radiance	Ship+Path Temperature	Background Radiance	Background Temperature	Apparent DT
1	0.107	159.562	0.9875	300.23	37.023798	0.962	1.03394	36.64713177	296.03	32.47968	288.97	7.06
15	0.155	130	0.9748	300.23	37.023798	0.952	1.33149	36.55963427	295.88	32.16871	288.42	7.46
18	0.199	120	0.9506	300.23	37.023798	0.943	1.58085	36.48688722	295.76	31.63351	287.47	8.29
21	0.306	109	0.8785	300.23	37.023798	0.924	2.12944	36.33572743	295.52	29.98601	284.48	11.04
24	0.717	98	0.7294	300.23	37.023798	0.864	3.88881	35.89218142	294.79	27.13858	279.05	15.74
25	1.146	95	0.6856	300.23	37.023798	0.813	5.43071	35.53846294	294.2	27.00474	278.78	15.42
26	2.88	92	0.6236	300.23	37.023798	0.655	10.28435	34.54974753	292.54	27.34466	279.45	13.09
275	3.857	91.5	0.6147	300.23	37.023798	0.586	12.44314	34.1427883	291.85	27.59885	279.95	11.9
271	5.307	91.1	0.6093	300.23	37.023798	0.5	15.13976	33.65906401	291.02	27.96645	280.66	10.36
299	6.551	90.9	0.6075	300.23	37.023798	0.439	17.07819	33.31682802	290.43	28.26909	281.24	9.19
298	7.43	90.8	0.6069	300.23	37.023798	0.401	18.2796	33.1076313	290.07	28.44433	281.58	8.49
297	8.595	90.7	0.6064	300.23	37.023798	0.356	19.69177	32.8648375	289.65	28.68894	282.04	7.61
296	10.229	90.6	0.6062	300.23	37.023798	0.302	21.37795	32.57394667	289.14	28.9886	282.61	6.53
295	12.723	90.5	0.6062	300.23	37.023798	0.237	23.43201	32.21775738	288.51	29.36314	283.32	5.19
2~13	15.027	90.44	0.6063	300.23	37.023798	0.191	24.9017	31.95843599	288.05	29.63658	283.83	4.22
2~11	16.035	90.42	0.6063	300.23	37.023798	0.173	25.44248	31.86240666	287.88	29.73818	284.02	3.86
294	17.225	90.4	0.6064	300.23	37.023798	0.155	26.01343	31.75582115	287.69	29.84631	284.22	3.47
2~8	18.668	90.38	0.6065	300.23	37.023798	0.136	26.6204	31.64823184	287.5	29.96226	284.44	3.06





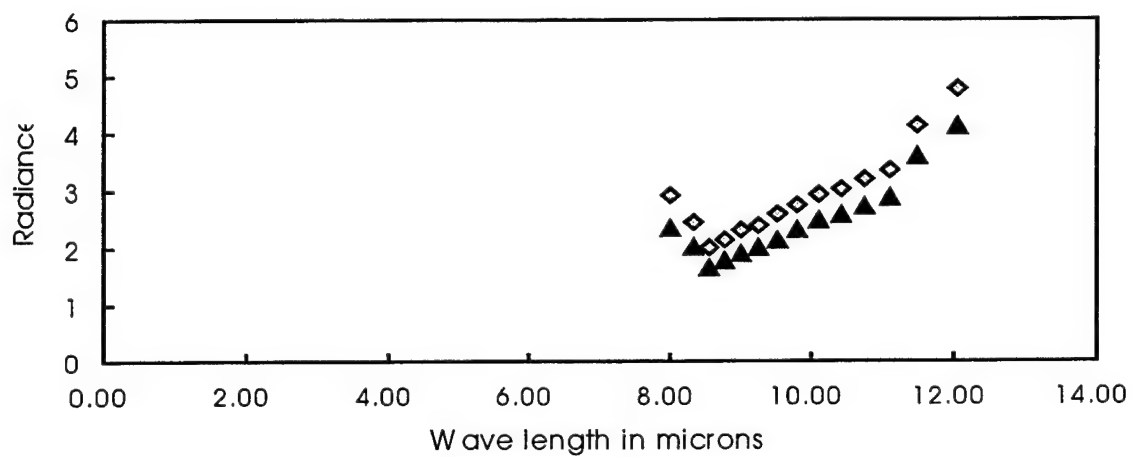
## **APPENDIX K**

### **SPECTRAL RADIANCE OF A BLACK BODY AT DIFFERENT TEMPERATURES**

In the following table a plot of the spectral radiances for a black body at 303.3 K and at 290 K is presented. The purpose of this plot is to evaluate the spectral characteristics of the target and background as they were used for the purposes of the thesis. As a result the spectral characteristics of the target and background do not seem to have any effect on the fact that the Apparent Temperature Difference for the polarized case goes negative after a certain range.

This plot shows the distribution of the radiance with wavelength for sub-bands across 8-12  $\mu m$  band, for gray body sources at 290 K (sea temperature) and 303.3 K (the ship hot spot temperature). The wavelength extend of the sub-bands is not constant. From these emitted sub-band radiances the available radiances at 25 km were computed using the sub-band transmission values shown in Figure 31. The effective band transmittance is then available as the ratio of the total radiance at 25 km to total emitted radiance. This quantity computed as .0756 showed no difference between the ship and background temperatures. However, it differs significantly from the LOWTRAN band averaged transmittance of 0.14. It should be noted that this comparison is strictly between the sea surface black-body emission and the ship hot spot temperature black body emission. Reflected sky radiance is not included in the plot numbers.

# Spectral Radiance at $T = 303.3$



◆ Spectral Radiance at 303.3 K    ▲ Spectral Radiance at 290 K

## LIST OF REFERENCES

1. Brochure from Army Night Vision and Electronic Systems Division (NVESD), Fort Belvoir, VA.
2. Michael C. Dudzik, *Electro-Optical Systems Design, Analysis, and Testing (The Infrared and Electro-Optical Systems Handbook, Volume 4)*, Infrared Information Analysis Center and SPIE, MI, 1993.
3. A.W. Cooper and E.C. Crittenden, *Electro-Optic Sensors and Systems*, Naval Postgraduate School, Monterey, CA, 1997.
4. Eugene Hecht, *Optics* (Second edition), Addison-Wesley Publishing Company, May, 1990.
5. Edward Collett, *Polarized Light, Fundamentals and Applications*, Marcel Dekker Inc., New York, NY, 1993.
6. A.W. Cooper, W.J. Lentz, P.L. Walker, P.M. Chan, "Infrared Polarization Measurements of Ship Signatures and Background Contrast," SPIE Proceedings, *SPIE International Symposium on Optical Engineering in Aerospace Sensing*, Orlando, FL, 1992.
7. D.L. Jordan, G. Lewis, "Infrared Polarization Signatures," AGARD Meeting on *Atmospheric Propagation Effects through Natural and Man-made Obscurants for Visible to MM-Wave Radiation*, SPIE Proceedings, May 1993.
8. M. Sidran, "Broadband Reflectance and Emissivity of Specular and Rough Water Surfaces," *Applied Optics*, Vol. 20, No.18, September 1981.
9. J.R. Maxwell, J.L. Beard, C. Due, "Polarization in the Thermal Infrared," Presented at the workshop on Detection, Discrimination and Classification of Targets in Clutter, November 1990.
10. P.M. Saunders, "Radiance of Sea and Sky in the Infrared Window 800-1200  $\text{cm}^{-1}$ ," *Journal of the Optical Society of America*, Vol 58, No. 5, May 1968.
11. T.J. Rogne, F.G. Smith, J.E. Rice, "Passive Target Detection Using Polarized Components of Infrared Signatures," *SPIE Proceedings on Polarimetry: Radar, Infrared, Visible, Ultraviolet and X-ray*, Vol. 1317, 1990.
12. G.C. Holst, *Electro-Optical Imaging System Performance*, SPIE and JCD Publishing, 1995.

13. D.J. Gregoris, S. Yu, A.W. Cooper, E.A. Milne, "Dual-band Infrared Polarization Measurements of Sun Glint from the Sea Surface," *SPIE Proceedings*, Vol. 1687, 1992.
14. S.B. Campana, Editor, *Passive Electro-Optical Systems (The Infrared and Electro-Optical Systems Handbook, Volume 5)*, Infrared Information Analysis Center and SPIE, MI, 1993.
15. AGA Thermovision Operating Manual, AGA Thermovision Systems AB, Publication No. 556 492, ed. II, 1980.
16. M.C. Pontes, "Polarization Effects on Infrared Target Contrast," Master's Thesis, Naval Postgraduate School, Monterey, CA, September 1998.
17. "Using IDL," IDL Version 5.0, Research Systems Inc., Boulder, CO, March 1997 Edition.
18. C.R. Zeisse, "SeaRad, A Sea Radiance Prediction Code," Technical Report 1702, Naval Command Control and Ocean Surveillance Center RDT&E Division, San Diego, CA, August 1995.
19. J.A. Ratches et al., "Night Vision Laboratory Static Performance Model for Thermal Viewing Systems," ECOM-7043, 1975.
20. J.M. Lloyd and R.L. Sendall, "Improved Specifications for Infrared Imaging Systems," *Proceedings of IRIS Imaging Symposium*, p.109-129, Infrared Information Analysis Center, ERIM, Ann Arbor, MI, 1970.
21. D.L. Shumaker, J.T. Wood, C.R. Thacker, *Infrared Imaging Systems Analysis*, The Environmental Research Institute of Michigan, 1993.
22. A.W. Cooper, E.C. Crittenden, E.A. Milne, P.L. Walker, E. Moss, D. Gregoris, "Mid and Far Infrared Measurements of Sun Glint from the Sea Surface," *SPIE Proceedings Vol. 1749 Optics of the Air-Sea Interface*.
23. J. D'Agostino and R. Moulton, "Minimum Findable Temperature Difference (MFTD)," *Infrared Imaging Systems: Design, Analysis, Modeling and Testing V*, G.C. Holst, *SPIE Proceedings* Vol. 2224, pp.74-94, 1994.
24. J. Johnson, "Analysis of Image Forming Systems," *Proceedings of Image Intensifier Symposium*, October 1958.
25. P. Moser, "Mathematical Model of FLIR Performance," NADC Technical Memorandum NADC-2023:PMM of 19 October 1972.

26. W.L. Wolfe, G.J. Zissis, *The Infrared Handbook*, The Infrared Information Analysis (IRIA) Center, Environmental Research Institute of Michigan, 4<sup>th</sup> Printing 1993.
27. Chih-Li Yu, "Estimate of Maximum Detection Range for FLIR from EOMET 95 Measurement Data," Master's Thesis, Naval Postgraduate School, Monterey, CA, December 1997.
28. C.R. Zeisse, "The Infrared Polarization of Sea Radiance," Technical Report 1743, Naval Command Control and Ocean Surveillance Center RDT&E Division, San Diego, CA, July 1997.



## INITIAL DISTRIBUTION LIST

	No. Copies
1. Defense Technical Information Center.....2 8725 John J. Kingman Rd., STE 0944 Ft. Belvoir, VA 22060-6218	
2. Dudley Knox Library.....2 Naval Postgraduate School 411 Dyer Rd. Monterey, CA 93943-5101	
3. Engineering and Technology Curricular Office.....1 Code 34 Naval Postgraduate School Monterey, CA 93943-5107	
4. Professor William B. Maier II, Code PH/Mw.....1 Chairman, Department of Physics Naval Postgraduate School Monterey, CA 93943-5117	
5. Professor Jeffrey B. Knorr, Code EC.....1 Chairman, Department of Electrical and Computer Engineering Naval Postgraduate School Monterey, CA 93943-5121	
6. Professor Alfred W. Cooper, Code PH/Cr.....2 Department of Physics Naval Postgraduate School Monterey, CA 93943-5117	
7. Professor Ron J. Pieper, Code EC/Pr.....1 Department of Electrical and Computer Engineering Naval Postgraduate School. Monterey, CA 93943-5121	
8. Naval Sea Systems Command.....1 PEO Expeditionary Warfare, ATTN: Mr. J.E. Misanin, 2531 Jefferson Davis Highway Arlington, VA 22242-5170 National Center 2 - Room 12E52	



9. Space and Naval Warfare Systems Center - SD.....1  
 Propagation Division  
 ATTN: Dr. J.H. Richter, Code D88  
 53570 Silvergate Ave.  
 San Diego, CA 92152-5230
  
10. Space and Naval Warfare Systems Center - SD.....1  
 RDT&E Division  
 ATTN: Dr. D.R. Jensen, Code D833  
 53570 Silvergate Ave.  
 San Diego, CA 92152-5230
  
11. Space and Naval Warfare Systems Center - SD.....1  
 RDT&E Division  
 ATTN: Dr. C.R. Zeisse, Code D883  
 53570 Silvergate Ave.  
 San Diego, CA 92152-5230
  
12. Naval Air Warfare Center.....1  
 Research and Technology Group, Physics Branch  
 ATTN: Dr. J. Bevan  
 China Lake, CA 93555-6100
  
13. Embassy of Greece .....1  
 Naval Attaché  
 2228 Massachusetts Avenue, N.W.  
 Washington, DC 20008
  
14. Evaggelos S. Lagaras, Admiral (Retired) Hellenic Navy.....1  
 Ethnikis Aminis 78  
 Papagos 156-69  
 Athens  
 GREECE-HELLAS
  
15. Spyridon E. Lagaras, Lieutenant Hellenic Navy.....2  
 Thrakis 4  
 Agia Paraskevi 153-41  
 Athens  
 GREECE-HELLAS